

Physics at the LHC Run-2 and Beyond

Andreas Hoecker

CERN, Geneva, Switzerland

Abstract

After an astounding Run-1 with 8 TeV proton–proton collisions featuring among others the discovery of the Higgs boson, Run-2 of the Large Hadron Collider (LHC) has started in 2015 colliding protons with unprecedented 13 TeV centre-of-mass energy. The higher energy and large expected integrated luminosity significantly increases the discovery potential for new physics, and allows for more detailed Higgs boson studies as well as improved Standard Model measurements. The lecture discusses methods, recent results and future prospects in proton–proton physics at the LHC.¹

1 Introduction

The Large Hadron Collider (LHC) at CERN probes nature at the smallest distances ever explored on Earth to study and improve our current knowledge of space and time, matter and force as it is encoded in the Standard Model (SM) of particle physics. The SM is *the* legacy of 20th century particle physics: it unifies quantum mechanics, special relativity and field theory; it unifies electromagnetic and weak interactions; it describes (about) all laboratory data. Does the SM deliver a complete answer to the complexity of the world generated by the simultaneous existence of very small as well as very large, seemingly fundamental numbers? We have reasons to believe that this is not the case.

The SM is made of spin one-half matter particles consisting of three generations of massive quarks and leptons, and force carriers in the form of partially massive spin one gauge bosons. An additional doublet of complex scalar fields, the Brout-Englert-Higgs (BEH) field ϕ , is dictated by the requirement of local gauge symmetry [1]. Its condensation after spontaneous symmetry breaking at low temperature is responsible for the masses of the SM gauge bosons and (chiral Dirac-) fermions, leaving the electromagnetic force with infinite range, but making the weak force short-ranged (about 10^{-15} cm). The new field is not only a constant background field, but it has its own massive quantum, the scalar Higgs boson. Being a boson, we might want to call it a fifth force. However, unlike the other forces, the new force is not a gauge force. Its non-universal coupling to masses of fermions and gauge bosons reminds us of classical gravitation, but the BEH force is much stronger than gravity and short-ranged.

The potential of the scalar double field ϕ consists in its simplest form at low temperature of three terms: a quadratic term with negative coefficient μ , a quartic term with positive coefficient λ realising the “Mexican hat” shape, and a Yukawa term describing the helicity-changing couplings between the BEH field and the fermions. The discovery of the Higgs boson and measurement of its mass fixes the coefficients to $\lambda = m_H^2/2v^2 \approx 0.13$ and $|\mu| = \sqrt{\lambda} \cdot v = m_H/\sqrt{2} \approx 89$ GeV, where $v = |\mu|/\sqrt{\lambda} = (\sqrt{2} \cdot G_F)^{-1/2} \approx 246$ GeV is the vacuum expectation value of ϕ .

We may wonder how the potential evolves with the decreasing temperature of the expanding universe. Above the critical temperature T_{EW} of approximately 100 GeV, during the earliest 10^{-11} second after the big bang where the universe covered a causal domain of a few cm, the evolution of the potential is such

¹As I am a member of the ATLAS experiment, for practical reasons, this lecture writeup leans somewhat towards ATLAS results. In the majority of the cases, the plots shown can be interchanged against those from CMS (and vice versa) without altering the message.

that its minimum is $\langle 0|\phi|0\rangle_{T>T_{EW}} = 0$. Gauge symmetry is respected, ie, all matter particles are massless and weak interaction is long-ranged. A spontaneous phase transition at T_{EW} (within the SM expected to be continuous, that is of second order) displaces the ground state of the BEH field to $\langle 0|\phi|0\rangle_{T<T_{EW}} = v$, breaking gauge symmetry. This spontaneous symmetry breaking corresponds to choosing a direction in the $SU(2)_L \times U(1)_Y$ group space. The condensed field fills all space-time, but without orientation as it has no spin. (One could imagine it as a Lorentz-invariant ether [2]). The massive gauge bosons and fermions interact with the condensate which effectively reduces their velocity. The acquired mass is proportional to the strength of that interaction. The action of the BEH field thus creates a “vacuum viscosity”.

There are many questions about the structure of the SM in particular related to the matter sector: a large mass hierarchy is observed; CP violation has been observed in the quark sector, consistent with a single CP-violating phase in the quark mixing matrix. In effect, three quark generations allow for exactly one such phase. The neutrino sector still bears many unknowns, among which the origin and values of neutrino masses, the neutrino nature, CP violation and whether or not there are sterile neutrinos that are singlets under the SM interactions (but possibly not under the new force).

Electroweak unification reduces the number of SM parameters from 20 to 19 (including the strong-CP parameter and neglecting the massive neutrino sector, which is irrelevant for LHC physics unless there are new right-handed neutrinos in reach of the LHC). Figure 1 demonstrates beautifully electroweak unification at work at the HERA collider in electron–proton and positron–proton scattering [3]. At low momentum transfer, neutral current processes with photon exchange producing an electron/positron in the final state dominate over charged current processes mediated via W bosons. Above 100 GeV, however, neutral and charged current processes are of similar size: electromagnetic and weak interactions are unified.² Electroweak unification relates the electromagnetic and weak coupling strengths to each other (the latter coupling given at lowest order by the ratio-squared of weak gauge boson masses). This relation has been tested experimentally to high precision [4].

The scales of particle physics reach from zero mass (for the photon and gluons) to as much as (and beyond) the Planck scale set by the strength of gravity. Within these two extremes lies the range of sensitivity of the LHC covering three orders of magnitude between roughly 10 GeV and 10 TeV, probing length scales down to an attometre. That range comprises the study of high-energetic radiation such as jets, charm and bottom flavour physics, top quarks, Z , W bosons and the Higgs boson, and any new physics that may reside therein. The physics at scales above that of the LHC is highly speculative. There

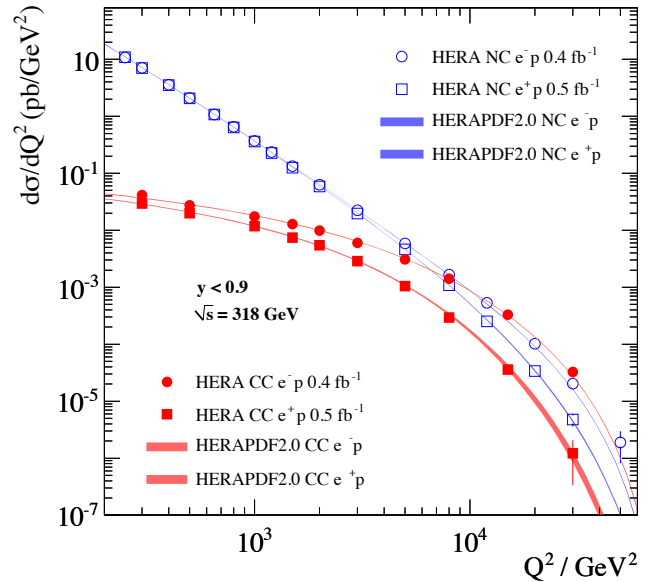


Fig. 1: Differential cross-section versus momentum transfer-squared measured at the HERA collider for neutral (blue) and charged (red) current deep inelastic scattering processes [3]. The data points are integrated over the Bjorken- x variable.

²Looking in more detail into Fig. 1, the neutral current cross sections for e^-p and e^+p are almost identical at small Q^2 but start to diverge as Q^2 grows. This is due to γ - Z interference, which has the opposite effect on the e^-p and e^+p cross sections. The charged current cross sections also differ between e^-p and e^+p scattering, with two effects contributing: the helicity structure of the W^\pm exchange and the fact that charged current e^-p (e^+p) scattering probes the u -valence (d -valence) quarks [3].

could be right-handed neutrinos of mass above 10^{10} GeV, as predicted by the (type 1) seesaw mechanism, the Peccei-Quinn axion scale above 10^{10} GeV to suppress strong CP violation, grand unification of the electroweak and strong forces at roughly 10^{15} GeV, quantum gravity at roughly 10^{18} GeV and the hypercharge Landau pole well above the Planck scale.

2 Particle physics at the dawn of the LHC

The Higgs boson — last of the particles? The SM predicts all properties, except for its mass. But before coming to the Higgs boson let us briefly recall the status of particle physics at the dawn of the LHC.

- LEP and SLC had ended their experimental programmes, with among their main results the proof of three light active neutrino flavours, and direct Higgs boson searches that excluded $m_H < 114$ GeV. Moreover, SM tests to unprecedented precision were performed with no direct or indirect hint for beyond the SM (BSM) physics. Among these, asymptotic freedom of strong interactions was tested to the percent level through measurements of the strong coupling strength $\alpha_s(\mu)$ at scales $\mu = m_\tau$ and $\mu = m_Z$, respectively, and comparison with the accurately predicted evolution from the QCD renormalisation group. In both cases the extraction occurred by comparing experimental results for the inclusive τ or Z hadronic widths (among other Z pole observables) with NNNLO (3NLO) perturbative QCD predictions.
- Precision measurements at the Z pole and of the top-quark and W -boson masses allowed to exclude an SM Higgs boson heavier than about 160 GeV at 95% confidence level. There are also theoretical arguments in favour of a not too heavy Higgs boson, which is required to moderate longitudinal weak-boson scattering at large momentum transfer. The evolution of the quartic coupling in the scalar potential with the energy scale Λ representing the SM cut-off scale where new physics occurs leads to constraints on m_H in terms of upper perturbativity and lower (meta)stability bounds. Indeed, the SM Higgs boson must steer a narrow course between two disastrous situations if the SM is to survive up to the Planck scale $\Lambda = M_{\text{Planck}}$.
- The Tevatron collider at Fermilab, USA still continued Run-2. That collider led to the discovery of the top quark and the measurement of its mass to better than 1%. The W boson mass was measured more precisely than at LEP and by today Tevatron dominates the world average. The mixing frequency of neutral B_s mesons was measured for the first time, and found in agreement with the SM prediction. The Higgs boson was beyond Tevatron’s sensitivity except for masses around 160 GeV, which could be excluded. No hint for BSM physics was seen.
- The B factory experiments BABAR at SLAC, USA and Belle at KEK, Japan were about to end with a precise confirmation of the Kobayashi-Maskawa paradigm of a phase in the three-generation CKM quark matrix being the sole responsible of the observed CP violation in the quark sector. Ambiguous initial hints about a possible difference in the unitarity triangle angle β extracted from tree and loop (“penguin”) processes disappeared with increasing statistics. The B -factory experiments measured many rare processes and observed for the first time CP violation in the charm sector.
- There was (and still is) no hint for charged-lepton flavour violation in spite of ever increasing experimental sensitivity. Any non-zero measurement would indicate new physics as the SM predictions via the massive neutrino sector are immeasurably small. Also, no sign of a CP-violating electric dipole moment (EDM) was seen in atoms or neutrons. The absence of a neutron EDM strongly constrains QCD induced CP violation that would be expected in the SM. Only the anomalous magnetic moment of the muon exhibits a long-standing $>3\sigma$ discrepancy between data and the SM prediction.
- The neutrino sector has seen a revolution after the discovery of neutrino oscillation and the mea-

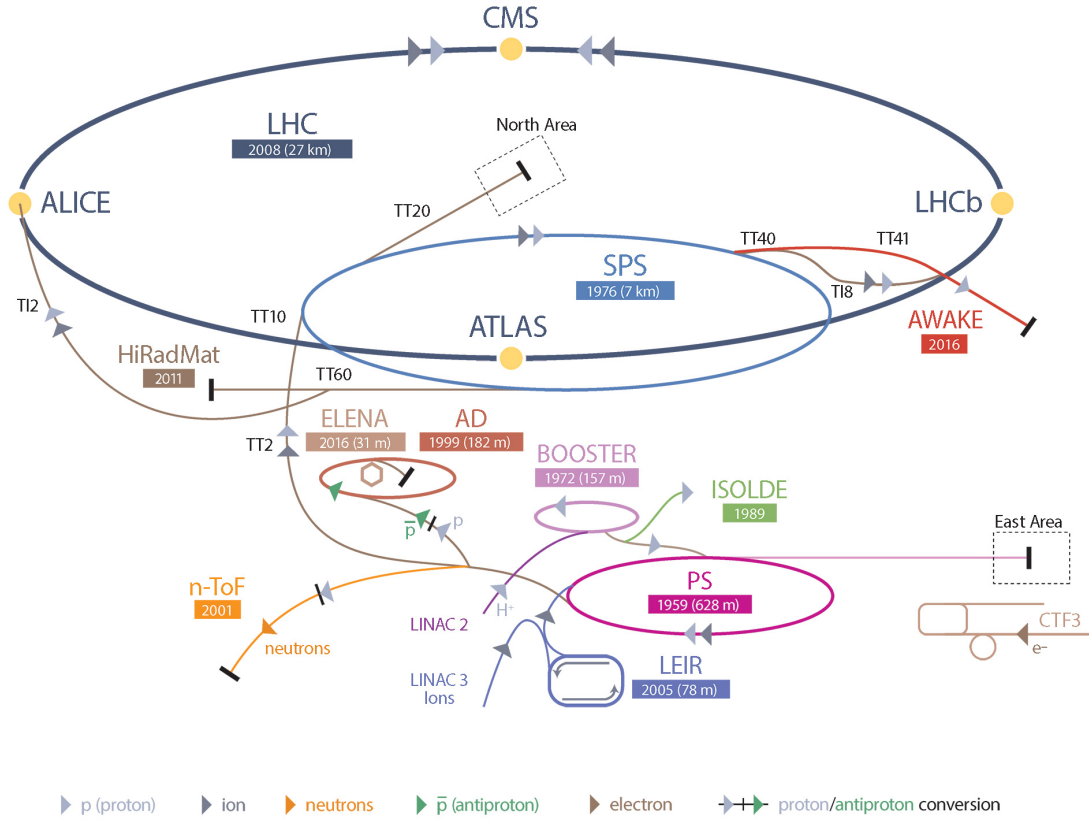


Fig. 2: Schematic view of CERN's accelerator complex.

surement of all three angles of the neutrino mixing matrix. These measurements establish that neutrinos have mass, but their nature (Dirac versus Majorana), mass hierarchy (normal versus inverted), as well as CP violating mixing phase remain unknown and are the subject of intense experimental activity.

- Finally, there has been no signal other than gravitational effects for dark matter, no signs of axions or of proton decay.³

3 Experimental setup

Producing the Higgs boson and searching for new physics at the TeV scale requires a huge machine. Particle accelerators exploit three principles: (i) they look deep into matter requiring high energy to resolve small de Broglie wave lengths (particle accelerators are powerful microscopes), (ii) Einstein's relation between energy and mass allows to produce potentially new heavy particles at high energy, and (iii) accelerators probe the conditions of the early universe through Boltzmann's relation between energy and temperature.

Figure 2 gives a schematic view of CERN's accelerator complex. It consists of a succession of machines

³It is not possible to reach energies in the laboratory that would allow to directly study the physics at the expected grand unification scale. Even Enrico Fermi's "Globatron" (that was to be built in 1994) would with current LHC magnet technology "only" reach insufficient 20 PeV proton-proton centre-of-mass energy. Proton decay is among the greatest mysteries in elementary particle physics. It is required for baryogenesis and predicted by grand unified theories (GUT). Its discovery could therefore provide a probe of GUT-scale physics. The best current limit on the partial proton lifetime from Super-Kamiokande, combining all its data from 1996 until now, is $\tau(p \rightarrow e^+ \pi^0) > 1.7 \cdot 10^{34}$ years.

that accelerate particles to increasingly higher energies and condition the particle beams. Each machine boosts the energy of a beam before injecting it into the next machine in the sequence. Protons are accelerated to 50 MeV in the Linac 2, to 1.4 GeV in the PS Booster, to 26 GeV in the PS (Proton Synchrotron) where also spatial proton bunches with 25 ns (7.5 m) distance and bunch trains are formed, 450 GeV in the SPS (Super Proton Synchrotron) before being injected in opposite directions into the LHC. Booster, PS and SPS have their own experimental halls where fractions of the beams are used for fixed target experiments at lower energies. The LHC [5] is a superconducting proton/ion accelerator and collider installed in a 26.7 km circumference, 70–140 m underground tunnel with 4 m cross-section diameter. Up to 2 800 bunches containing each more than 100 billion protons are accelerated within roughly 20 minutes from 450 GeV up to the design energy of 7 TeV per beam. So far, proton–proton collisions with centre-of-mass energies of 0.9, 2.8, 5, 7, 8, and 13 TeV were delivered by the LHC. In addition, data with 5 and 8 TeV proton–lead and 2.8 and 5 TeV lead–lead collisions were taken.

The most challenging component of the LHC are the 1 232 superconducting dipole magnets realised in a novel “2-in-1” design that guide the protons along their circular trajectory around the ring. The dipoles have a length of 14.3 m each, and are cooled to 1.9° K by means of a closed circuit of 120 tonnes liquid-helium. The LHC also features almost 400 focusing quadrupole magnets and 3 700 multipole corrector magnets. The maximum dipole field strength of 8.3 T, achieved with a current of almost 12 kA, limits the energy to which the protons can be accelerated. The proton’s energy is given by $E_p[\text{TeV}] = \sqrt{4\pi\alpha} \cdot B[\text{T}] \cdot r[\text{km}]$ so that, with the radius $r = 4.3$ km, one finds $E_p \sim 7$ TeV taking into account that only roughly two-third of the ring are equipped with dipoles. Following the scale-energy relation $\mu \approx 200 \text{ GeV am} / E[\text{TeV}]$, does the LHC thus probe length scales of $\mu \sim 10^{-20}$ m at 14 TeV centre-of-mass energy? It is not quite that small as the protons are composite particles whose energy is distributed among its constituents (partons).

The LHC hosts four large, ultra-sophisticated experiments among which the general purpose detectors ATLAS and CMS, as well as ALICE and LHCb dedicated mainly (but not only) to heavy-ion and flavour physics studies, respectively, requiring optimisation for low transverse momentum physics. There are additional smaller-scale experiments dedicated to forward physics. The design of the ATLAS detector emphasises excellent jet and missing transverse momentum resolution, particle identification, flavour tagging, and standalone muon measurement. CMS features excellent electron/photon energy and track (muon) momentum resolution, and flavour tagging. Both detectors are highly hermetic with very few acceptance holes allowing to precisely determine missing transverse momentum. ALICE has highly efficient track reconstruction in busy heavy-ion environment and particle identification. LHCb is a forward spectrometer with a trigger for fully hadronic B and D hadron events, excellent low-momentum track resolution, and particle identification (pion/kaon separation).

The particle detectors measure particles produced as debris from the proton–proton collisions through interaction with active material. Different concentric detector layers measure different properties. The innermost parts of the detectors measure tracks of charged particles in layers of semi-conductors or straw tubes that respond to traversing charges. The momentum and charge of these particles is measured through their immersion in a homogeneous magnetic field. Outside the tracking volume are thick calorimeters that absorb most particles and measure their energy. Additional tracking chambers behind the calorimeters identify and measure muons, which are minimum ionising in most of their momentum range and thus penetrate the calorimeter layers. Neutrinos do not interact with the detector and therefore induce missing energy. Due to the non-zero longitudinal momentum of the collisions in the laboratory frame and the missing acceptance coverage along the beam line, only the transverse missing momentum in a collision is conserved. Hence, the reconstructed missing transverse momentum is used to detect neutrinos or any unknown non or weakly interacting particles. In addition to stable particles, the experiments also reconstruct jets from near-by calorimeter depositions or tracks. Jets are narrow cones of

hadrons and other particles produced by the hadronisation of a quark or gluon due to QCD confinement. Reconstruction of long-lived states in a jet allows to tag jets originating from b or c quarks. The ensemble of measurements in a given proton–proton bunch crossing makes up an event. It contains more than the original hard parton scattering due to underlying event interaction and additional soft proton–proton interactions (dubbed “pileup”).

LHC computing represents “big data”: the LHC experiments started more than a decade ago with large scale computing, which is now present everywhere. The ATLAS managed data volume of roughly 150 petabyte (dominated by simulated data) is of similar order as the Google search index or the content uploaded to Facebook every year. Unlike these companies, however, the LHC has to manage its data volume with a public science budget.

4 Experimental methods

We will review in this chapter a few (basic) experimental concepts at the LHC.

4.1 Luminosity

Besides energy, luminosity is the single most important quantity in collider physics. The instantaneous luminosity of the beam collision, expressed in units of $\text{s}^{-1}\text{cm}^{-2}$, is a function of the LHC beam parameters as follows

$$L = \frac{f_{\text{rev}} \cdot n_{\text{b}} \cdot N_p^2}{4\pi \cdot \sigma_x \cdot \sigma_y} \cdot F(\theta_c, \sigma_x, \sigma_z), \quad (1)$$

where $f_{\text{rev}} = 11\,245.5$ Hz is the bunch revolution frequency determined by the size of the LHC (27 km) and the speed of light, $n_{\text{b}} = 1, \dots, 2\,808$ is the number of proton bunches in the machine (2 808 is the maximum number of possible 25 ns slots; the theoretical maximum of 3 564 bunches cannot be reached due to space needed between bunch trains and for the beam dump kicker magnets (abort gap)), $N_p \approx 1.15 \cdot 10^{11}$ is the number of protons per bunch (the bunch intensity), and $\sigma_{x,y} = 12, \dots, 50 \mu\text{m}$ is the transverse beam width characterising the beam optics. The factor $F(\theta_c, \sigma_x, \sigma_z)$ accounts for luminosity reduction due to the beam crossing angle θ_c , roughly given by $(1 + (\sigma_z/\sigma_x)^2 \cdot (\theta_c/2)^2)^{-1/2}$, the hourglass effect leading to a varying transverse bunch size in the collision point because of the several cm longitudinal bunch extension, and other effects.

Luminosity drives the statistical precision of any measurement and our ability to observe low cross section processes as

$$N_{\text{events}}^{\text{obs}} = \text{cross section} \times \text{efficiency} \times \int L \cdot dt, \quad (2)$$

where the cross section is given by Nature, the efficiency of detection is optimised by the experimentalist, and the integrated luminosity is delivered by the LHC. There are several options to maximise the luminosity of the machine as outlined below.

- **Maximise the total beam current.** The cryogenic system limits the maximum beam current leading to an anticorrelation between N_p and n_{b} . Improvements in beam collimation, cryogenics vacuum, and background protection allow to extend that limit.
- **Maximise brightness and energy, minimise β^* .** The transverse beam size is given by $\sigma(s) = \sqrt{\beta(s)\epsilon_n/\gamma}$, where $\sigma^* = \sigma(s=0) \approx 17 \mu\text{m}$ at the collision point. The value $\beta^* \approx 60$ cm is the longitudinal distance from the focus point where the transverse beam size grows twice as wide. The emittance $\epsilon \cdot \pi$ is the area in phase space occupied by the beam, and $\epsilon_n \approx 3.8 \mu\text{m}$ is the normalised

emittance, where the Lorentz γ factor is taken out. To reduce (“squeeze”) β^* one needs to respect the quadrupole aperture limit. The beam brightness, N_p/ε_n , is limited by beam–beam interactions which have a quadrupole de-focusing effect, and by space-charge tune shift and spread (the tune spread is limited by resonances).

- **Compensate reduction factor.** The crossing angle is required to avoid parasitic long-range beam encounters. The hour glass effect may be reduced by shorter bunches, at the expense of a higher longitudinal pileup density.

The LHC group offers an excellent tool [6] to study the dependence of the expected LHC luminosity under various parameter settings.

The instantaneous luminosity is measured by the experiments [7–9] with dedicated detector systems that are calibrated with the use of so-called van-der-Meer beam-separation scans [10]. Such scans are performed in specific low-intensity LHC fills during which the beams are separated from each other by an increasing distance in both x and y directions. The dedicated luminosity detectors count for each scan point the hits they receive from inelastic minimum-bias events. From the Gaussian profile of the hit counts versus the beam separation one can determine the transverse beam profiles entering Eq. (1) via the convolution relation $\sigma_{x,y} = \Sigma_{x,y}/\sqrt{2}$, where it is assumed that both LHC beams have the same width. The knowledge of L from the measured beam currents and beam widths in the specific LHC fill allows to extract the visible cross section, σ_{vis} , for any dedicated luminosity detector (this may include, for example, cluster counting in the Pixel detector). During normal (ie, high-luminosity) data taking, the counts measured in that detector together with the calibrated visible cross section from the van-der-Meer scan allow to extract the luminosity via $L = N_{\text{counts}}/\sigma_{\text{vis}}$. Note that this method does not require to know the acceptance nor the efficiency of the luminosity detector, which are included in σ_{vis} .

The precision of the luminosity calibration depends on many factors. Systematic uncertainties arise from correlations between the x and y transverse beam positions during the scan, beam–beam corrections, beam orbit drifts and position jitters, stability (reproducibility) of the results, and instrumental effects such as the absolute length scale calibration for the separated beams, beam backgrounds and noise, the reference specific luminosity, the measurement of the beam currents, and the extrapolation of the calibration from the low to high-luminosity regimes as well as the run-by-run stability of the luminosity detectors. The best precision on the integrated luminosity achieved by the experiments undercuts 2%.

During Run-1 of the LHC, spanning the years 2010–2012 of data taking, the peak luminosity achieved was $L_{\text{peak}} = 7.7 \cdot 10^{33} \text{ cm}^{-2}\text{s}^{-1}$ and an integrated luminosity during the year 2012 of 23 fb^{-1} at 8 TeV proton–proton centre-of-mass energy was delivered to the experiments. With 50 ns bunch distance a maximum number of 1380 colliding bunches was reached. At L_{peak} the LHC produced every 45 minutes a $H \rightarrow \gamma\gamma$ event, and typically two 160 pb^{-1} fills were needed to produce one $H \rightarrow 4\ell$ ($\ell = e, \mu$) event.

The high luminosity of the LHC comes to the price of additional inelastic proton–proton pileup interactions within a bunch crossing. An average of $\langle\mu\rangle = 21$ (maximum $\langle\mu\rangle = 40$) interactions per crossing occurred during 2012, with a similar or slightly higher rate in 2016. The LHC design pileup value at 14 TeV is obtained as follows

$$\langle\mu\rangle = \frac{\sigma_{\text{inel}} \cdot L}{f_{\text{rev}} \cdot n_b} \approx \frac{80 \text{ mb} \cdot 10 \text{ nb}^{-1}\text{s}^{-1}}{11\,245 \text{ s}^{-1} \cdot 2\,808} \approx 25, \quad (3)$$

where we used $10^{34} \text{ cm}^{-2}\text{s}^{-1} = 10 \text{ nb}^{-1}\text{s}^{-1}$. When the detector response integrates over several bunch crossings, as for example the calorimeter pulse shape, pileup occurring in the recorded proton collision (in-time pileup) as well as that in neighbouring collisions (out-of-time pileup) affect the event reconstruction. Most analyses are fairly insensitive to pileup at the rates experienced so far. Mitigation methods

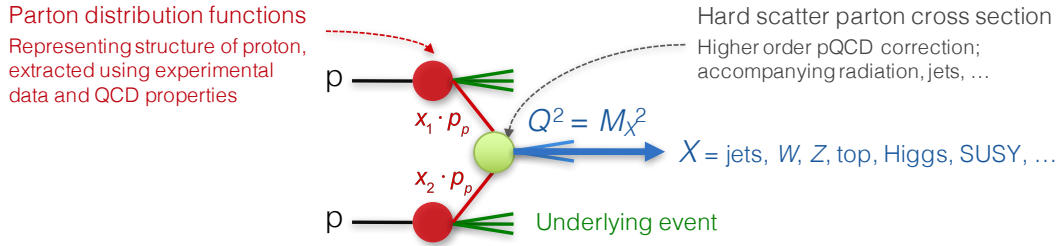


Fig. 3: Simplified view of a proton–proton collision.

have been developed to further improve the robustness of the physics object reconstruction and analyses. Pileup does, however, affect the trigger requiring higher thresholds, which impacts the low transverse momentum physics programme of the experiments. It also increases the stored event size and CPU time needed for track reconstruction.

4.2 Proton–proton collisions

Owing to factorisation (see for example [12]), the cross section of a proton–proton collision can be computed as the convolution of parton density functions⁴ (PDF) with the parton scattering matrix element (cf. Fig. 3). The PDFs are universal distributions containing the long-distance structure of the proton (or hadrons in general) in terms of valence and sea quarks and gluons. They are related to parton model distributions at leading order, but with logarithmic scaling violations (DGLAP⁵). Since precise Lattice QCD predictions are not yet available, the PDFs are extracted versus the parton momentum fraction x and the momentum transfer Q^2 using experimental data and exploiting QCD evolution properties. The centre-of-mass energy-squared of the parton collision, \hat{s} , is given by the product of the momentum fractions of the colliding partons, $x_{1,2}$, times the proton centre-of-mass energy: $\hat{s} = x_1 \cdot x_2 \cdot s$. The production of the 125 GeV Higgs boson thus occurs at an average momentum fraction $\langle x \rangle \sim 0.01$ at $\sqrt{s} = 13$ TeV.

The parton density functions rise dramatically towards low x in particular at high Q^2 and most notably for the gluon density. The consequences are: the cross section of a given pro-

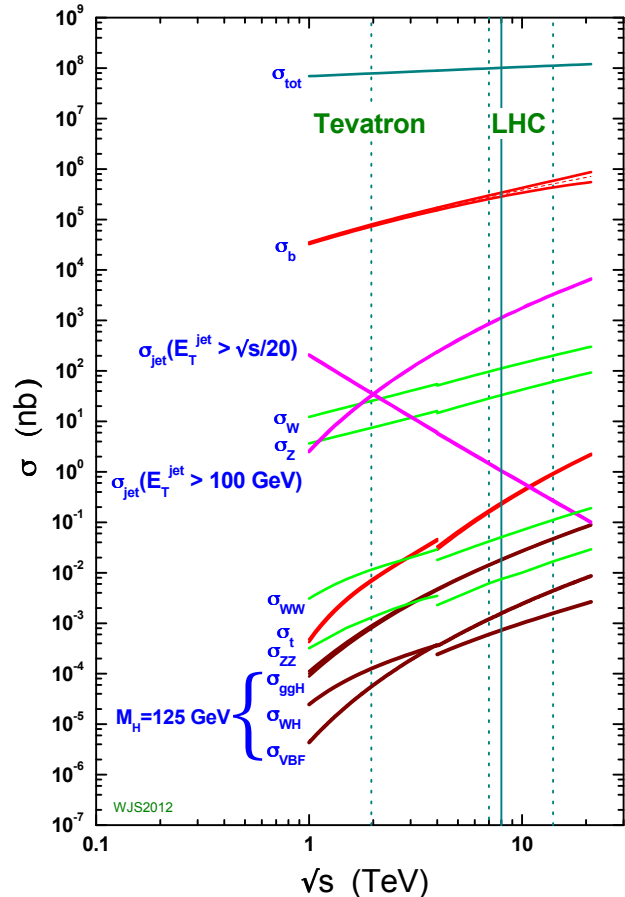


Fig. 4: Cross sections of selected proton–(anti-)proton processes versus centre-of-mass energy [11].

⁴Parton density functions were introduced 1969 by Feynman in the parton model to explain Bjorken scaling in deep inelastic scattering data.

⁵In analogy with a running coupling strength, one can vary the factorisation scale and obtain the renormalisation group equation for PDFs. The DGLAP equations [13] describe the Q^2 dependence of the PDFs.

cess increases with increasing proton–proton collision energy, more luminosity allows to reach higher parton collision energy, and the low- x regime is dominated by gluon–gluon collisions. Hence, although the parton-level cross sections falls with centre-of-mass energy, the cross-sections of proton–proton processes rise due to the convolution with increasing PDFs. This is depicted in Fig. 4: all cross sections rise with centre-of-mass energy, where gluon initiated processes have a steeper slope than quark initiated ones because of the strong enhancement of the gluon PDF towards lower x . One notes that when requiring a centre-of-mass-energy dependent minimum transverse momentum for jets, the jet cross section decreases with centre-of-mass energy as expected for a parton–parton cross section. The inclusive cross section is dominated by inelastic scattering (also denoted minimum bias events), the interesting jet and boson physics processes have many orders of magnitude lower rates.

4.3 The experimental data path in a nutshell

The LHC detectors cannot record events at the filled proton bunch crossings rate of approximately 30 MHz⁶ as each event has an approximate raw size of 2 MB, requiring to store 60 TB per second. This is not only impractical given the computing resources, but also unnecessary in view of the LHC physics goals as most events contain only soft minimum bias interactions. Instead, online custom hardware and software triggers reduce that rate by filtering out events with a million and more times smaller cross sections than minimum bias events.

The data path of an LHC experiment can be described in a nutshell as follows.

1. LHC bunches collide every 25 n (50 ns during Run-1), but not all bunches are filled with protons.
2. LHC detectors record the detector response in pipelined on-detector memories that are time-stamped (synchronised) to the LHC collisions they belong to. The events are kept during the latency of the first level trigger decision (2–3 μ s).
3. Level-1 hardware and high-level software triggers filter the interesting events that are written to disk. The level-1 trigger system reduces the initial bunch crossing rate to up to 100 kHz. The high-level trigger further reduces this rate to about 1 kHz that are kept. A trigger menu is a large collection of physics and monitoring triggers. Among these are low-threshold single lepton triggers, single missing transverse momentum and jet triggers, and lower threshold di-object and topological triggers. The online system also provides detailed data quality monitoring.
4. The recorded data are subject to prompt offline calibration and refined monitoring, followed by the prompt reconstruction (mostly) at CERN.
5. The reconstructed data are distributed to computing centres world-wide from where standardised derived datasets are produced for physics and performance analysis.
6. Large amounts of Monte Carlo events using the same reconstruction software as used for data are also produced and distributed for analysis.
7. Performance groups provide standard physics objects with calibrations and uncertainties, unified in analysis releases. Analysis groups build physics analyses on top of this ground work.

⁶The LHCb phase-1 upgrade is preparing for exactly that!

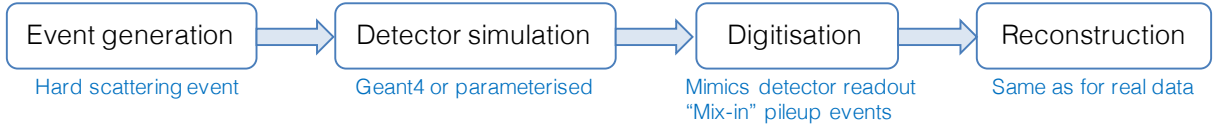


Fig. 5: Monte Carlo event simulation chain.

4.4 Monte Carlo event simulation

A crucial ingredient to any physics and performance analysis is Monte Carlo (MC) event simulation. MC events mimic the physics processes, which allows to isolate specific processes by subtracting simulated background processes, to evaluate the acceptance and efficiency of signal processes, to optimise signal selection, and to evaluate systematic uncertainties by varying MC parameters.

The MC generation path is sketched in Fig. 5. A matrix element generator calculates the hard parton–parton scattering event and stores it in a common data format. The event is passed through the detector simulation which simulates the interactions of the stable particles with the active and passive detector material. The simulation may use Geant4 [14] or a parametrised fast simulation. The output of that process is subject to the digitisation step during which the detector response and readout is mimicked. After this step the simulated data have the same format as real detector data except for the so-called truth information which records the information about the generated particle types, decay chains and four-momenta. The following event reconstruction is identical to that of real data (also format wise).

The physics modelling with event generators proceeds as follows. The hard scattering matrix element calculation including initial and final-state radiation (ISR/FSR) is convolved with the parton density functions. Decays of the hard subprocesses, and multiple parton interactions (and their ISR/FSR) are also generated. Matrix elements are used as much as possible, but one cannot fully avoid phenomenological description of nonperturbative effects such as parton showers, hadronisation, and the underlying event. State-of-the-art event generation includes next-to-leading order (NLO) matrix elements up to two partons, leading order (LO) matrix elements up to 5 partons, parton shower matching. Nonperturbative and electroweak corrections are sometimes applied. Fixed-order calculations are known to higher order (NNLO or even 3NLO). The physics modelling, including PDFs, has the largest systematic uncertainty in many analyses and is therefore a critical step that requires care, extensive validation and sometimes correction with data.

There has been significant progress in both generator developments and fixed-order calculations. Fixed-order predictions have seen an NNLO revolution with about 20 new results during the last two years. Some of the resulting NNLO to NLO K-factors, in particular for diboson production, were not covered by the uncertainties assigned to the NLO calculations as obtained from the canonical factors two and one-half variations of the renormalisation scale [15].

4.5 Cross section measurement and data unfolding

The measurement of the cross section of a given process requires to isolate this process via selection of its final state, followed by the subtraction of contributing background processes. The remaining number of events needs to be corrected for resolution effects, the selection efficiency and, in case of the total cross section, the acceptance:

$$\sigma_{pp \rightarrow X}^{\text{tot}} = \frac{1}{A_X} \sigma_{pp \rightarrow X}^{\text{fid}} = \frac{1}{A_X} \left(\frac{N_{\text{obs}} - N_{\text{bkg}}}{L \cdot C_X} \right). \quad (4)$$

Here, N_{obs} and N_{bkg} are the total observed and the estimated number of background events, L the integrated luminosity, $A_X = N_{\text{gen, fid}}/N_{\text{gen}}$ is the acceptance factor, given by the fraction of generated $pp \rightarrow X$ events falling into the fiducial acceptance defined close to the final state selection, $C_X = N_{\text{reco, sel}}/N_{\text{gen, fid}}$ is a correction factor that corrects for the detector resolution and inefficiency of events generated in the fiducial region, and $\sigma_{pp \rightarrow X}^{\text{fid}}$ is the fiducial cross section.

The acceptance factor is computed entirely from theory using the best available fixed order calculation. The correction factor depends on the particle detector and is partly or fully determined from MC simulation. It is therefore the main interest of the experimentalist to determine the fiducial cross section, which is corrected for experimental effects and has minimal theory dependence. The acceptance correction to obtain the total inclusive cross section is left for theory.

The definition of the fiducial cross section should facilitate the comparison between theoretical predictions and experimental results and thus should have the least possible dependence on the MC event generators available at the time of the measurement. A suitable definition of the observables is based on the physical particles that enter the detector. This includes the stable particles which account for the majority of interactions with the detector material, and from which the measurements are ultimately made. A detailed discussion about the definition of particle level objects is provided in a dedicated ATLAS note [16].⁷

A differential cross section corresponds to a binned fiducial cross section. It requires the application of unfolding due to bin-to-bin correlations. Unfolding is a mathematically unstable inversion problem that requires careful regularisation.

4.6 Background determination

The subtraction of backgrounds as in Eq. (4) usually relies on MC simulation. In case of new physics searches, which often select extreme phase space regions such as a very large effective mass⁸ as illustrated in Fig. 6, the MC predictions may suffer from large and difficult to estimate modelling uncertainties. More robust and reliable background estimates normalise the MC predictions of the main backgrounds in phase space regions (dubbed “control regions”) close to the signal region. Sometimes further data driven corrections for the transfer of the MC normalisation from the control region to a signal region are required.

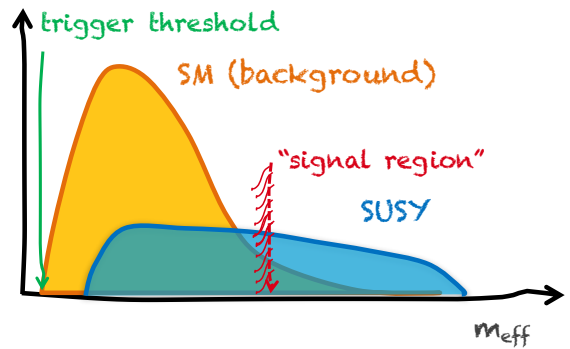


Fig. 6: Sketch illustrating signal and background distributions of a discriminating variable. A requirement is applied to enrich the signal.

For a typical search for supersymmetry looking for jets, possibly b -jets and leptons, and missing transverse momentum, the main background sources stem from top production, W + jets and $Z(\rightarrow \nu\nu)$ + jets

⁷The recommendations in Ref. [16] about how to suitably define an event topology at particle level on MC are: 1. Select the stable particles. 2. Select prompt leptons (e, ν_e, μ, ν_μ) and associate photons (not from hadrons) to electrons and muons to define dressed-level charged leptons. 3. Define particle-level jets by clustering all stable particles excluding the particles found in step (2). 4. Assign the jet flavour based on heavy-flavour hadrons ghost-matched to jets. 5. Sum all prompt neutrinos defined in (2) to form the missing transverse momentum. 6. Resolve lepton-lepton and jet-lepton overlap following a procedure close to that used at the detector level. 7. Define other particle-level observables in complex event topologies based on the particle-level objects defined above.

⁸The effective mass, m_{eff} , is defined by the scalar sum of the transverse momenta of all selected objects and the missing transverse momentum.

events, WW , WZ , ZZ diboson production, and rare processes such as $tt + W$ or $tt + Z$. All these backgrounds may produce true missing transverse momentum due to decays to neutrinos. Additional backgrounds may arise from misreconstruction of multijet events, or the misidentification of non-prompt leptons or jets as prompt leptons. Such backgrounds are usually determined from data using control regions or so-called ABCD sideband methods exploiting two or more none or only weakly correlated variables. The former backgrounds are often called irreducible, and the latter due to misreconstruction are denoted reducible backgrounds. MC simulation is mainly used to predict irreducible backgrounds, in particular if they are sub-dominant.

4.7 Basic physics objects

All ATLAS and CMS physics analyses are built upon basic physics objects. These correspond to single stable particles, ensembles of particles or event properties.

Tracks and vertices are measured in the inner tracking systems. Their precise measurement requires an accurate detector alignment which is obtained from data by minimising hit residuals with respect to fitted tracks. Also important is a precise mapping of the inner tracker geometry and material, which is made with the help of survey data, and from collision data using reconstructed vertices from hadronic interactions, photon conversions to electron–positron pairs, track extensions, and long-lived hadrons.

- **Electrons and photons** are reconstructed as energetic clusters in the electromagnetic calorimeter associated or not with an inner detector track. Due to significant amount of active and passive tracker material (between 0.4 and 2.4 radiation lengths depending on $|\eta|$),⁹ roughly 40% of the photons convert to electron–positron pairs and hence are reconstructed as one or two displaced electron tracks. The electron efficiency, energy scale and resolution are precisely calibrated in data using $Z \rightarrow ee$, $J/\psi \rightarrow ee$ and $W \rightarrow e\nu$ events. Photons are calibrated using MC and radiative $Z \rightarrow ee(\mu\mu) + \gamma$ events, as well as $\pi^0 \rightarrow \gamma\gamma$ decays at low energy.
- **Muons** are reconstructed in the inner tracker and the outer muon systems. Combined tracking improves the momentum resolution for high transverse momentum (p_T) muons, which are dominated in precision by alignment uncertainties. Muons are calibrated using $Z \rightarrow \mu\mu$, $J/\psi \rightarrow \mu\mu$ and $\Upsilon(1S) \rightarrow \mu\mu$ events.
- **Hadronic τ decays** (τ_h) to a narrow jet of charged and neutral pions or kaons are reconstructed in the inner tracker and the electromagnetic and hadronic calorimeters. Multivariate analysers (and particle flow in CMS, see next item) are used to combine the available detector information and improve the efficiency and purity of the selection as well as the energy measurement (using multivariate regression). Taus are calibrated using $Z \rightarrow \tau_h\tau_h$ decays and E/p for the hadronic tracks.
- **Jets** are formed by clustering particles using the infrared and collinear safe¹⁰ anti- k_r algorithm [17] (for which the distance between clustered particles is defined using negative p_T power) via a pairwise successive aggregation of proto-jets. Jet particles are reconstructed in the electromagnetic

⁹The “rapidity” of a particle is defined by $y = \frac{1}{2} \ln[(E + p_z)/(E - p_z)]$, where E denotes the particle’s energy and p_z the particle’s momentum along the beam direction (z). Differences in rapidity are Lorentz invariant under a boost along z . The “pseudorapidity” is defined by $\eta = \frac{1}{2} \ln[(p + p_z)/(p - p_z)] = -\ln(\tan \frac{\theta}{2})$. The azimuthal angle ϕ is measured in the plane transverse to the beam direction and the polar angle θ is measured with respect to the beam direction. Rapidity and pseudorapidity are equal for massless particles.

¹⁰Infrared safety requires that a jet remains unaffected when adding a particle with $|p_T| \rightarrow 0$ to it. Collinear safety requires that a jet remains unaffected when replacing a particle i with four-momentum p_i by two particles j and k with four-momenta $p_j + p_k = p_i$ such that $|\vec{p}_i - \vec{p}_j| = 0$, where $\vec{p} = (y, \phi)$.

and hadronic calorimeters in ATLAS, and with the use of a particle flow algorithm in CMS. The particle flow algorithm aims at identifying and reconstructing all the particles from the collision by combining the information from the tracking and calorimeter devices. The algorithm results in a list of particles, namely charged hadrons, neutral hadrons, electrons, photons and muons, which are used to reconstruct jets and missing transverse momentum (see next item), and to reconstruct and identify hadronic τ decays. In ATLAS, tracks are used via a multivariate algorithm to identify low transverse momentum jets from pileup interactions. Neutral energy contributions from pileup are corrected by subtracting from the calorimeter jet energy a contribution equal to the product of the jet area and the median energy density of the event. The jet energy scale and resolution are calibrated using the constraint from transversely balanced dijet and multijet events, photon plus jet and Z plus jet events, and E/p together with test beam results to extrapolate the absolute calibration to large transverse momenta with insufficient data coverage.

- **Missing transverse momentum** is computed as the negative vector sum of the transverse momenta of all identified objects (leptons, photons, jets, ...), and a contribution denoted soft term from objects originating from the primary event vertex that are not associated to any identified object. ATLAS uses a track-based soft term and CMS uses the particle flow algorithm. The missing transverse momentum magnetitude is denoted E_T^{miss} .
- **Flavoured jets** containing a b or c hadron are identified in the inner tracking detector as a property of a reconstructed jet. The characteristics of (long-lived) weakly decaying heavy flavour hadrons include a displaced secondary vertex, large impact parameter, a large hadron mass, and semi-leptonic decays in 30–40% of the cases. A multivariate algorithm combines the available information to tag jets containing a heavy-flavour hadron (and hence originating from a heavy-flavour quark). The efficiency of b -tagging is calibrated from data using $t\bar{t}$ events, muons from heavy flavour decays in dijet events, and using MC simulation to extrapolate the calibration to high transverse momenta. Charm tagging is calibrated using $W + c$ or $D^* \rightarrow D^0(\rightarrow K\pi)\pi$ events. Mistag rates are obtained from tracks with negative impact parameters or secondary vertices with negative decay lengths.

4.8 Boosted objects

The high centre-of-mass energy of the LHC can produce highly boosted W , Z , H bosons or top quarks so that their hadronic decays are merged into a single jet. This would occur in particular in presence of hypothetical heavy states that decay to massive bosons or top quarks. The identification and reconstruction of such merged objects requires a jet substructure analysis. Boosted signatures can also be used to enhance the signal-to-background ratio in some analyses such as $H \rightarrow \tau\tau$ and $H \rightarrow bb$. Boosted signatures originating from a very hard ISR jet can be used to render visible to the trigger and data analysis collisions with soft final state activity (eg., WIMPs, compressed spectra in supersymmetry or other new physics models).

The average transverse distance between two bodies originating from the decay of a resonance with mass m and transverse momentum p_T can be approximated by $\Delta R = \sqrt{\Delta\phi^2 + \Delta\eta^2} \approx 2m/p_T$. A W boson with $p_T = 200$ GeV (400 GeV) has $\Delta R = 0.8$ (0.4). To ensure that all final state objects are fully contained the experiments usually employ so-called “fat jets”, which are jets with radius parameter $R = 1$ or 1.2, compared to standard anti- k_t jets [17] of $R = 0.4$. There exist many strategies to reconstruct the substructure in a fat jet (eg., jet mass), and to correct for pileup effects (jet grooming), see, eg. [18, 19] and references therein.

4.9 Systematic uncertainties

Systematic uncertainties are the evil (see figure on the right) in every measurement. Well designed experiments minimise systematic uncertainties by achieving maximum phase space coverage, high measurement precision, response homogeneity and linearity, high calorimeter depth, sufficient longevity of the detector components including resistance against irradiation, etc. The understanding, evaluation and reduction of systematic uncertainties is often the main analysis challenge. A high quality analysis stands out by its thoroughness on all relevant sources of systematic uncertainty. It is thereby important to distinguish relevant from irrelevant sources, where in doubt a source should be considered relevant. For many uncertainty sources, in particular theoretical ones, estimating a “one-sigma” error is very difficult or simply impossible. In such cases conservative uncertainties should be chosen where possible.



(Reasonably) conservative uncertainty estimates are a must! It is of no use to the scientific endeavour to make over-aggressive statements that one cannot fully trust.

5 Physics highlights from the LHC Run-1

The LHC Run-1 featured proton–proton collisions at 7 and 8 TeV with datasets corresponding to approximately 5 and 20 fb⁻¹ integrated luminosity for ATLAS and CMS, and a total of 3 fb⁻¹ for LHCb. There are numerous physics highlights published in altogether more than a thousand physics papers. Only a small subset of these are recollected here.

5.1 Standard Model and top-quark physics

We should praise the extraordinary match between a plethora of total, fiducial and differential cross-section measurements of all known proton–proton scattering processes and their theoretical predictions, confirming the predictive power of the SM. An example for the measurement of double-differential jet cross-sections by CMS compared to theory prediction is shown in Fig. 7 [20]. Figure 8 gives a summary of ATLAS Run-1 and Run-2 cross-section measurements witnessing the large variety of channels and cross section magnitude, as well as the agreement with the SM predictions. There are many subtleties in this comparison that are not represented in such a summary plot. For example, diboson cross sections exhibit some discrepancy with the NLO SM predictions, which are resolved by moving to NNLO and by taking into account soft-gluon resummation corrections that are needed in case of phase space cuts sensitive to such effects (as, eg., a low- p_T jet veto). A compilation like Fig. 8 delivers a strong statement about the depth of the understanding of hadron collider physics at the highest centre-of-mass energies. It gives confidence that new physics searches, which depend on a good understanding of SM processes, can be reliably performed. We should stress that Run-1 analysis is not over yet: it represents a high-quality, extremely well understood data sample for precision measurements.

The analysis of Run-1 data allowed first critical electroweak studies of vector-boson scattering (VBS). In electroweak theory the Higgs boson acts as “moderator” to unitarise high-energy longitudinal vector boson scattering. Indeed, if only Z and W bosons are exchanged, the amplitude of (longitudinal) $W_L W_L$ scattering, $A_{Z,\gamma} \sim v^{-2} \cdot (s+t)$, rises with the centre-of-mass energy and violates unitarity. Higgs-boson exchange regularises this amplitude via the negative term $A_H \sim -(m_H^2/v^2) \cdot (s/(s-m_H^2) + t/(t-m_H^2))$, if m_H^2/v^2 is not too large, which is the case for $m_H = 125$ GeV. That mechanism can be tested by, eg., measuring same-charge $W^\pm W^\pm + 2\text{jets}$ production at the LHC (see graphs in Fig. 9). Requiring same-sign $W^\pm W^\pm$ production greatly reduces strong production (see right-hand graph in Fig. 9) due to the lack of

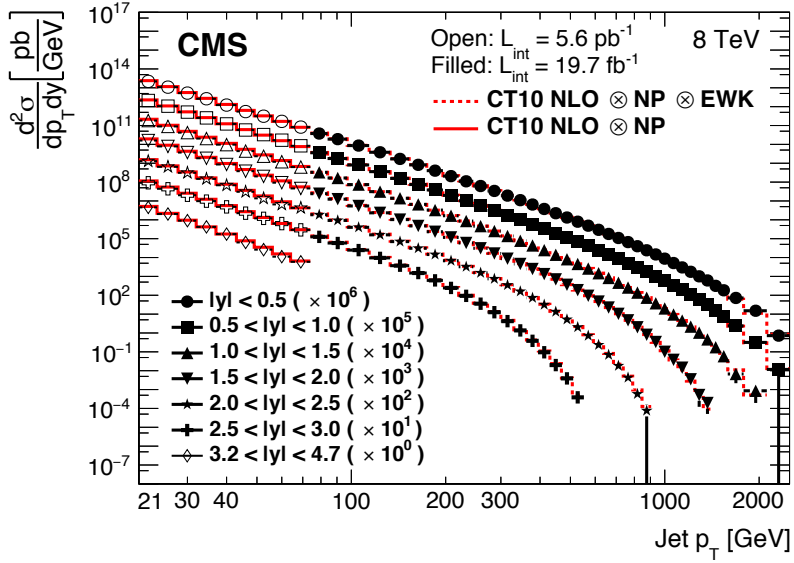


Fig. 7: Double-differential inclusive jet cross sections as function of jet transverse momentum measured by CMS (dots with error bars) in 8 TeV data [20]. The red lines indicate the SM predictions using NLO perturbative QCD and applying nonperturbative (low- p_T) and electroweak corrections.

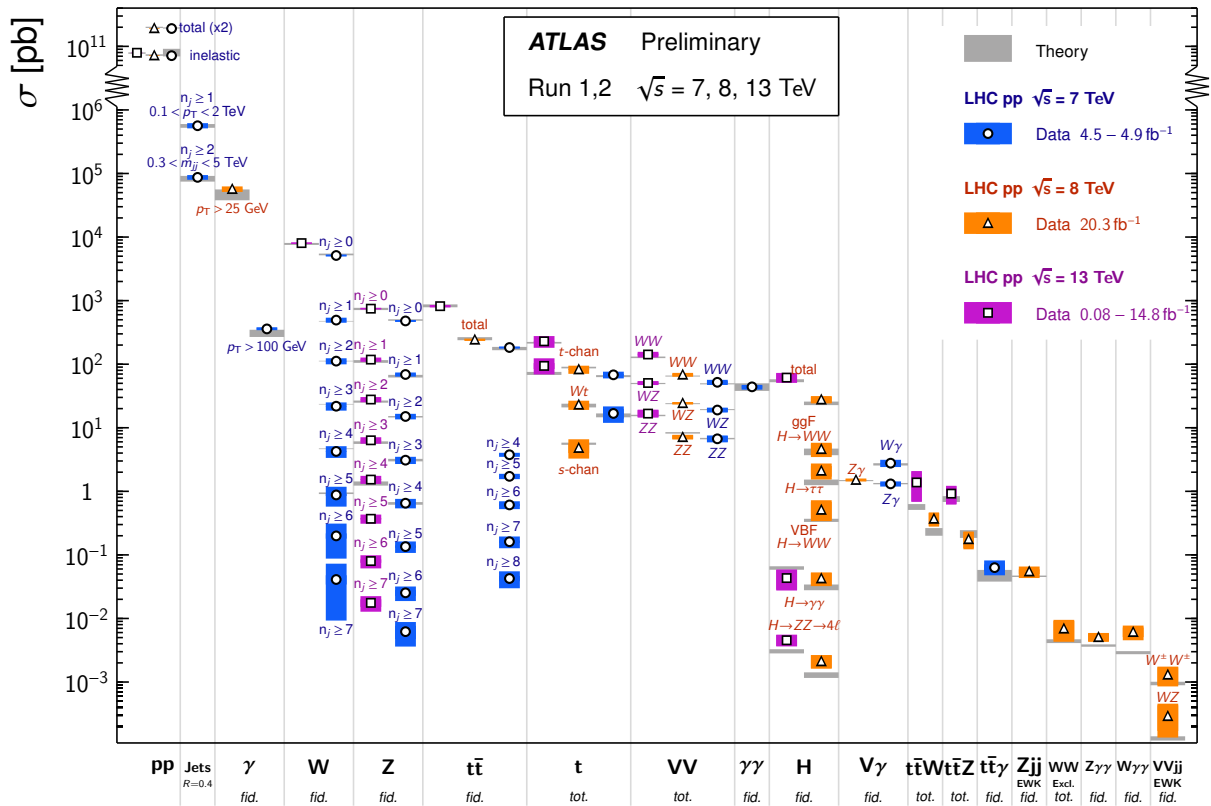


Fig. 8: Summary of ATLAS Run-1 and Run-2 cross-section measurements (status August 2016).

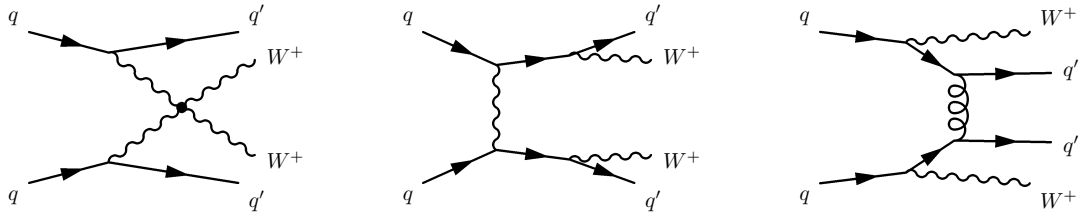


Fig. 9: Feynman graphs for same-charge $W^\pm W^\pm + 2$ jets production. Top: electroweak VBS; middle: electroweak non-VBS; bottom: gluon exchange.

contributions from two initial gluons or one quark and one gluon. It also suppresses the s-channel Higgs amplitude, but moderation through t-channel Higgs exchange remains. The two electroweak processes in Fig. 9 cannot be separated in a gauge-invariant way. Contributions from electroweak VBS to this process can be separated from non-VBS electroweak and strong processes by requiring a large dijet invariant mass and a rapidity gap for hadronic activity. Evidence for electroweak production at the 3.6σ (2.0σ) level was found by ATLAS (CMS) [21, 22].

Strong top-quark pair production has been studied with unprecedented experimental precision at the LHC. Inclusive cross sections are best measured in the dilepton $e\mu$ final state that is very pure and can be isolated with a minimal set of selection requirements. The measurements provide precise tests of NNLO QCD including leading-logarithmic resummation.¹¹ In addition, many top properties (mass, charge, charge asymmetry, polarisation, spin correlations, suppressed flavour-changing neutral currents (FCNC), etc.) were measured or probed.

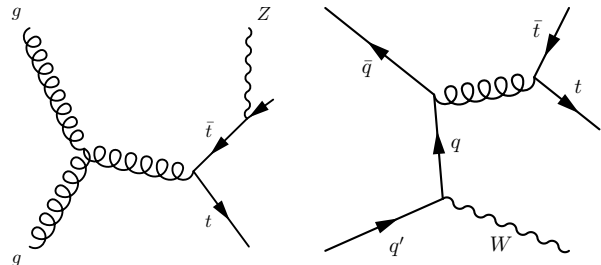


Fig. 10: Feynman graphs for leading order ttZ (left) and ttW production.

The large luminosity and high centre-of-mass energy also allowed to observe the rare $tt + W$ and $tt + Z$ production (see Feynman graphs in Fig. 10) with more than 7.1σ combined significance for both modes [23, 24]. The neutral-current tZ coupling is directly probed in $tt + Z$.

Run-1 also allowed detailed studies of electroweak single top production and property measurements (see Fig. 11 for representative leading-order diagrams). Single top cross sections are enhanced at the LHC compared to the Tevatron: at 8 TeV LHC centre-of-mass energy, factors of 42 (t-channel), 31 (Wt), but only 5 for s-channel production so that the signal to background ratio is worse for the latter channel at the LHC. Production of t-channel single top has been studied in great differential detail already [25, 26]. The separate measurement of tq and $\bar{t}q$ production provides sensitivity to u and d quark PDFs. Inclusive Wt channel production was clearly observed by both ATLAS and CMS [27, 28]. Production via an s-channel process (see bottom diagram in Fig. 11) was recently observed by the Tevatron experiments with 6.3σ combined significance in agreement with the SM prediction [30]. ATLAS reported an observed evidence of 3.2σ (for 3.9σ expected significance), also in agreement with the SM prediction [29].

¹¹The cross section of soft gluon emission is infrared divergent (eikonal factor). The divergence is cancelled by virtual corrections up to logarithmic leftover terms $\sigma(a \rightarrow b) \rightarrow \sigma \ln^2(1 - m_b^2/s)$, which need to be resummed. Several resummation strategies denoted “threshold resummation”, “transverse momentum resummation”, or “high-energy resummation” exist in the literature.

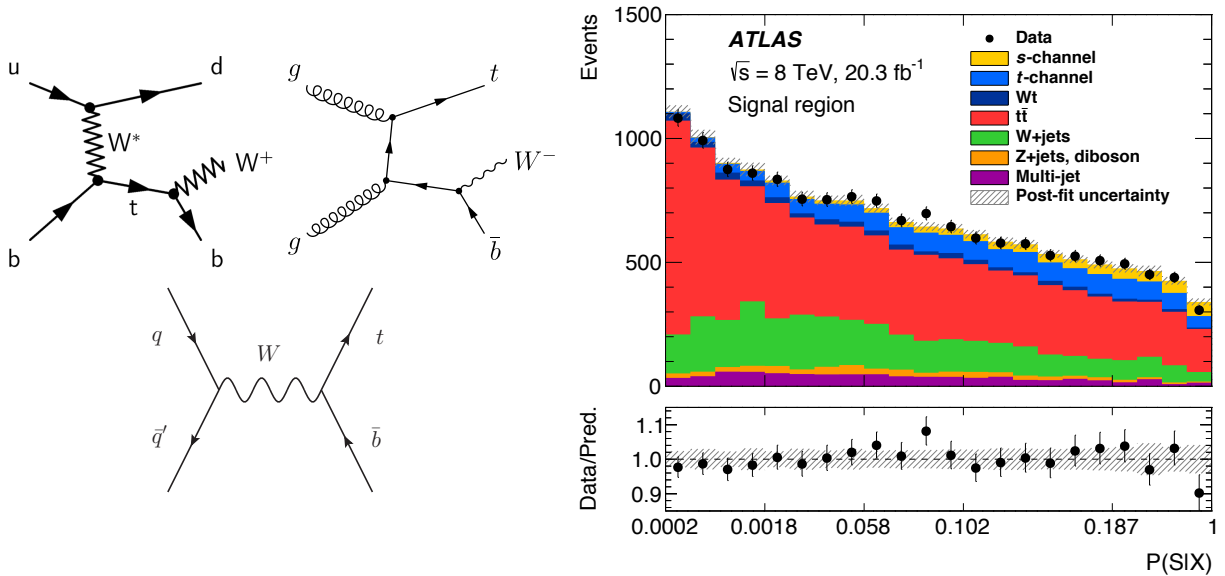


Fig. 11: Left: leading-order Feynman graphs for t-channel (top left), Wt -channel (top right), and s-channel (bottom) single top production at the LHC. Right: distribution of a discriminant variable in an ATLAS search for s-channel single top production [29].

5.2 Higgs boson physics

Among all the Run-1 physics results, the discovery of the Higgs boson is (so far) the magnum opus [31, 32] (articles that each have collected about 6 700 citations to date). The Higgs boson had been vainly searched for at many accelerators. The most stringent non-LHC limits came from the Large Electron–Positron Collider (LEP at CERN, 1989–2000) and the proton–antiproton collider Tevatron (Fermilab, 1990–2011) excluding at 95% confidence level $m_H < 114 \text{ GeV}$ [33] and $149 < m_H < 182 \text{ GeV}$ [34], respectively. Global fits to electroweak precision data (see Section 6) constrained the Higgs boson mass via logarithmic corrections and excluded about $m_H > 160 \text{ GeV}$ at 95% confidence level [35].

At the LHC the Higgs boson is dominantly produced via gluon fusion with a cross section of 19.3 pb at 8 TeV for $m_H = 125 \text{ GeV}$ [36] (see also [37] for a recent review on Higgs boson physics). The cross section steeply falls with the Higgs boson mass. Additional production modes are weak boson fusion (VBF) with 1.6 pb , associated production with a weak boson (also denoted Higgs-strahlung) with 0.70 pb (0.42 pb) for WH (ZH), and associated production with a $t\bar{t}$ or $b\bar{b}$ pair (ttH , bbH) with 0.13 pb and 0.20 pb , respectively (cf. Fig. 12 for the corresponding Feynman diagrams). The uncertainties in the predictions are larger ($7\sim 14\%$) for the gluon initiated processes than for the quark initiated ones ($\sim 3\%$, dominated by PDF uncertainties). The inclusive 8 TeV Higgs cross section amounts to 22 pb . In total, about 470 thousand SM Higgs bosons of 125 GeV were produced in 2012 at 8 TeV in each ATLAS and CMS.

Because of the coupling to the mass of the decay particles ($\propto m_V^2, m_f$) the Higgs boson decays with preference to the heaviest particles allowed. It does not couple directly to photons and gluons but proceeds via loops involving preferentially heavy particles (eg., top, W boson). The branching fractions predicted for an SM Higgs boson of mass 125 GeV are shown on the right panel of Fig. 12. The theoretical uncertainty in these predictions ranges from 3% to about 12%. The leptonic ($\ell = e, \mu$) and photon final states provide the best discovery sensitivity. The decays $H \rightarrow \gamma\gamma$ and $H \rightarrow ZZ^{(*)} \rightarrow 4\ell$ provide the best mass resolution ($1\text{--}2\%$ for $m_H = 125 \text{ GeV}$). The decay $H \rightarrow WW^{(*)} \rightarrow 2\ell 2\nu$ ($\sim 20\%$ mass resolution due to the neutrinos in the final state) has a good trigger, a sustainable background level, and large branching

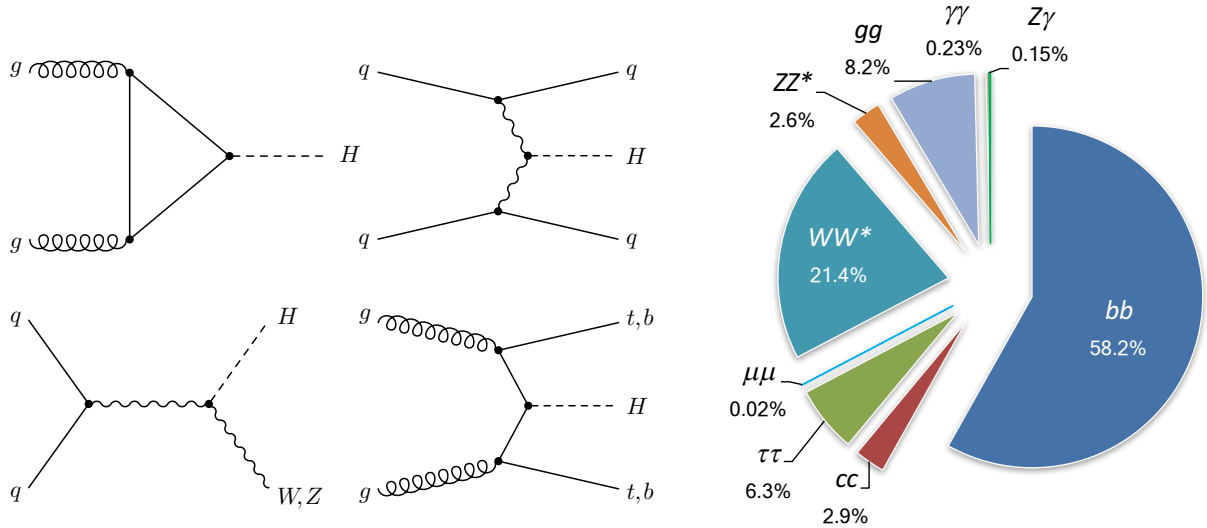


Fig. 12: Left: Feynman graphs for the dominant Higgs production channels: gluon fusion via (dominantly) a top quark triangle (top left), weak boson fusion (top right), associated production with a weak boson (bottom left) and with a heavy quark pair (bottom right). Right: branching fractions predicted for an SM Higgs boson of mass 125 GeV [36]. Considering only leptonic decays to e, μ , the exploitable branching fractions to WW^* and ZZ^* are 1.1% and 0.012%, respectively.

fraction. The fermionic modes $H \rightarrow \tau\tau$ and $H \rightarrow bb$ have mass resolutions of about 10% and 15%, respectively, and are more challenging to detect due to large backgrounds. The decays $H \rightarrow \mu\mu$ and $H \rightarrow Z(\rightarrow \ell\ell)\gamma$ have excellent mass resolution but too low branching fractions to be in reach with the current datasets.

It is fortunate that at $m_H = 125$ GeV many decays of the Higgs boson are experimentally accessible. The phenomenological aspects of that mass might appear less appealing as we will see later. The dominant $H \rightarrow bb$ mode is only exploitable in association with W/Z or tt . Their leptonic decays provide a trigger signal and help to reduce the overwhelming background from strong interaction bb continuum production, $\sigma(bb) \sim \mathcal{O}(100 \mu\text{b})$. A boost of the Higgs boson helps to improve the signal purity at the expense of reduced efficiency.

There is no doubt about the discovery of the Higgs boson. Each of the most sensitive bosonic channels $H \rightarrow \gamma\gamma$, $H \rightarrow 4\ell$ and $H \rightarrow 2\ell 2\nu$ from ATLAS and CMS have achieved an independent observation (cf. Fig. 13) [38–43]. The combination of ATLAS and CMS mass measurements gives $m_H = 125.09 \pm 0.21_{\text{stat}} \pm 0.11_{\text{syst}}$ GeV [44]. There are very different experimental challenges in each Higgs channel. All analyses have constantly increased their sensitivity during Run-1 owing to improved understanding of lepton reconstruction and calibration, as well as improved background modelling and signal against background discrimination.

In addition to sophisticated individual analyses, ATLAS and CMS have joined forces and combined their Higgs mass and coupling measurements [44, 45]. These combinations represent the full picture of what the experiments have learned in a framework that consistently treats all processes in terms of production mechanism and decay. Figure 14 shows as an example the ratios of measured to predicted signal strengths per production process (left panel, assuming the Higgs decays to proceed according to the SM), and vice versa per decay channel (middle panel, assuming SM Higgs production) [45]. The overall signal strength, assuming an overall scale for all individual signal strengths, is measured to be $\mu = 1.09 \pm 0.11$. The right hand panel of Fig. 14 shows the results of a fit of leading order coupling modifiers [46] to

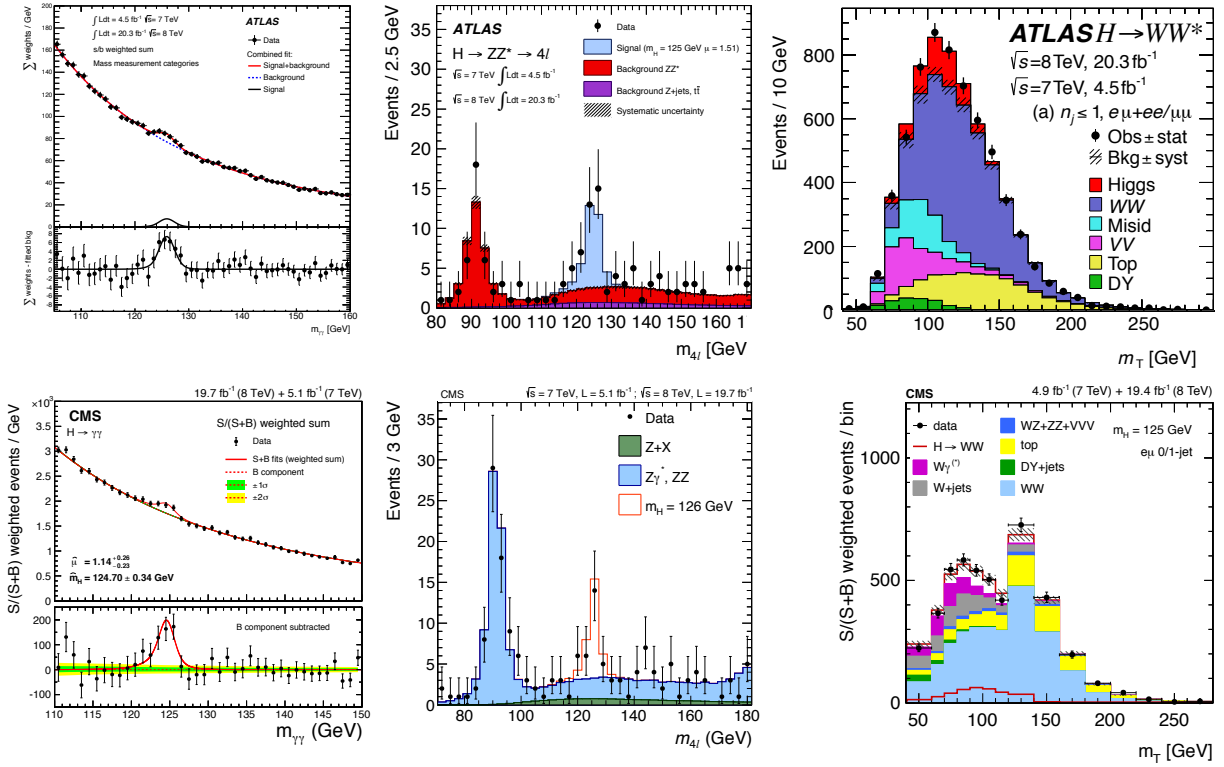


Fig. 13: Reconstructed inclusive Higgs candidate masses in the bosonic decay channels $H \rightarrow \gamma\gamma$ (left), $H \rightarrow 4\ell$ (middle), and $H \rightarrow 2\ell 2\nu$ (right, shown is the transverse mass) for the ATLAS (top row) and CMS (bottom row) Run-1 analyses [38–43].

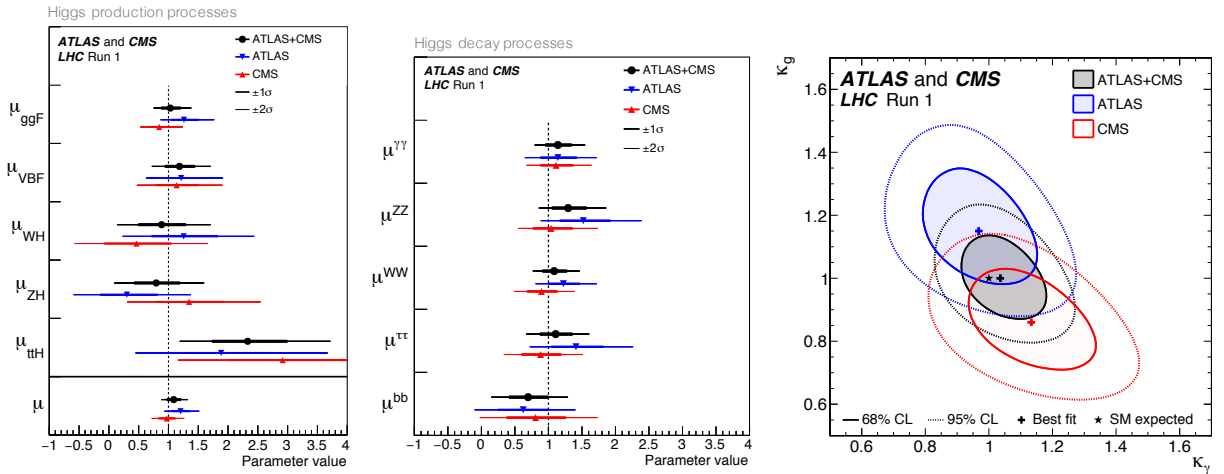


Fig. 14: Left: Higgs production signal strengths for ATLAS and CMS and their combination. Also shown is the measurement of the global signal strength. Middle: Higgs decay signal strengths for ATLAS, CMS and their combination. Right: 68% and 95% confidence level contours in the Higgs-to-gluon versus Higgs-to-photon coupling modifiers for ATLAS, CMS and their combination. The SM prediction is $\kappa_g = \kappa_\gamma = 1$. See text for the assumptions underlying these plots. The figures are taken from [45].

the combined Higgs boson data, where for a given production process or decay mode, denoted j , the coupling modifier κ_j is defined such that $\kappa_j^2 = \sigma_j/\sigma_j^{\text{SM}}$. Shown in the figure are the coupling modifiers κ_g versus κ_γ of the Higgs-to-gluon and Higgs-to-photon couplings, respectively. The fit was performed by constraining all the other coupling modifiers to their SM values and assuming no non-SM decays of the Higgs boson. The resulting agreement with the SM is remarkable as these couplings proceed through loops involving heavy fermions and also, in the photon case, bosons (W). It is a powerful probe for new heavy degrees of freedom. For example, the result allows to reject a theory with heavy fermions with SM-like Yukawa couplings.¹² The ATLAS and CMS Higgs coupling combination exhibits agreement among the two experiments. It yields sufficient significance for the observation of the Higgs decay to fermions, $H \rightarrow \tau\tau$ [47, 48], and of VBF production. The ttH process [49, 50] comes out a bit large with a relative signal strength of $\mu = 2.3$ and a combined observed significance of 4.4σ (for 2.0σ expected). With respect to the signal strengths shown in Fig. 14 we note that the least model-dependent observables at the LHC are coupling ratios rather than absolute coupling measurements [45].

The Higgs boson has been suggested to possibly act as a “portal” to new physics responsible for dark matter. In such models, a massive dark matter particle couples only weakly (or not at all) with the SM particles, except for the Higgs boson.¹³ If the dark matter particle is not too heavy, the Higgs decays invisibly to it and is searched for via, eg., a VBF topology where the forward jets are used to trigger and select the events [51, 52]. Limits of about 25% are currently set for an invisible Higgs boson decay. In general, owing to its low mass and consequently narrow width of 4.1 MeV compared to the widths of the W , Z or top quark of 2.1 GeV, 2.5 GeV and 1.3 GeV, respectively, the Higgs boson has good sensitivity to new physics as even small couplings to new states (if light enough) can measurably impact its branching fractions (see [53] for an analysis of constraints on new physics from the measurements of the Higgs couplings and invisible decays). It is therefore important to continue to measure the Higgs couplings, including the invisible one, with highest possible precision.

5.3 Heavy flavour physics

There have been beautiful flavour and low- p_T physics measurements at the LHC. The LHCb experiment has produced a flurry of important results among which the observation, together with CMS [54], of the very rare decay $B_s \rightarrow \mu\mu$ at a branching fraction of $2.8_{-0.6}^{+0.7} \cdot 10^{-9}$ in agreement with the SM prediction of $3.7 \pm 0.2 \cdot 10^{-9}$ [55]. The left panel of Fig. 15 shows representative SM and BSM Feynman graphs, and the right panel shows the combined CMS and LHCb data and the result of a simultaneous signal and background fit. The $B_s \rightarrow \mu\mu$ decay proceeds through a loop as there is no tree-level FCNC in the SM. It is in addition CKM and helicity suppressed, thus the low branching fraction. The decay is sensitive to additional scalar bosons as, eg., predicted in supersymmetry. ATLAS recently published the Run-1 result giving a branching fraction value in agreement with CMS and LHCb and approximately 2σ below the SM prediction [56].

Another high-priority flavour result from the LHC is the measurement of the mixing-induced CP violation parameter ϕ_s in a flavour-tagged, time-dependent $B_s \rightarrow J/\psi\phi$ analysis. That measurement represents one of the most sensitive CP-violation tests of the SM as ϕ_s is small and predicted with negligible theoretical uncertainty within the CKM paradigm. ATLAS [57], CMS [58] and LHCb [59] have measured simultaneously ϕ_s and $\Delta\Gamma_s$, the width difference of the two B_s mass eigenstates, with LHCb exhibiting the best precision. It found the combined result $\phi_s = -0.010 \pm 0.039$ rad in agreement with the SM. Fig-

¹²Naively an additional heavy fermion generation would increase the gluon fusion Higgs cross section by a factor of nine with respect to the SM prediction due to the quadratic fermion form-factor dependence of the cross section.

¹³For example in a Dirac neutrino case the massive right-handed neutrinos would transform as singlets under the SM gauge interactions, but would couple to the Higgs boson.

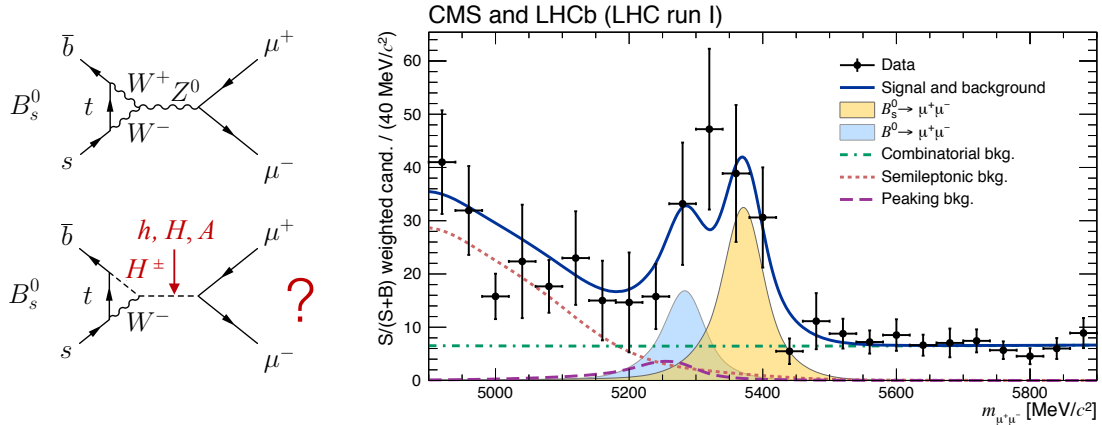


Fig. 15: Left: Feynman graphs for the decay $B_s \rightarrow \mu\mu$ in the SM (top) and beyond the SM (bottom). Right: weighted distribution of the dimuon invariant mass for all CMS and LHCb measurement categories. The yellow region indicates the fit result for $B_s \rightarrow \mu\mu$, while the blue region shows that for the doubly CKM suppressed decay $B_d \rightarrow \mu\mu$. The dashed and dotted lines indicate the various background contributions as obtained from the fit (the abundance of the peaking background is predicted) and the solid line their sum [54].

ure 16 shows the various measurements as well as their combination as 68% confidence level contours in the $\Delta\Gamma_s$ versus ϕ_s plane. The SM prediction is indicated by the black vertical bar.

LHCb also contributed significantly to the long-term effort to overconstrain the CKM matrix in what is known as the unitarity triangle, a triangle given in the $\bar{\rho}-\bar{\eta}$ CKM parameter plane, where $\bar{\eta} \neq 0$ stands for CP violation in the SM. LHCb has engaged in a vigorous programme to determine the unitarity triangle angle $\gamma \sim \arg(-V_{ub}^*)$. It can be measured through interference of $b \rightarrow u$ with $b \rightarrow c$ tree transitions where hadronic amplitude parameters are determined simultaneously with γ from the data. A combined fit [60], dominated by the measurements from charged B^+ to charm decays, gives $\gamma = 70.9_{-8.5}^{+7.1}$ deg, which is in agreement with the prediction from the CKM fit (not including the direct γ measurements) of 68 ± 2 deg [61]. LHCb also measured the ratio $|V_{ub}/V_{cb}|$ from $\Lambda_b \rightarrow p\mu\nu$ (a baryon decay!) with 5% precision [62]. The result is closer to the exclusive B -factory numbers for $|V_{ub}|$, which exhibit a tension with the larger inclusive numbers. Furthermore LHCb obtained the world's best single Δm_d measurement [63] $0.5050 \pm 0.0021 \pm 0.0010$ ps⁻¹ (the B -factories have a combined uncertainty of 0.005 ps⁻¹), a $\sin(2\beta)$ measurement [64] of $0.731 \pm 0.035 \pm 0.020$ that approaches the precision of the B -factories, the world's best constraints on CP violation in $B_{(s)}^0$ mixing ($\alpha_{sl}^s, \alpha_{sl}^d$) in agreement with the SM (D0 sees a 3.6σ deviation), and a search for CPT violation [67] (difference in mass or width) in the $B_{(s)}^0$ systems together with the measurement of sidereal phase dependence of the CPT violating parameter.

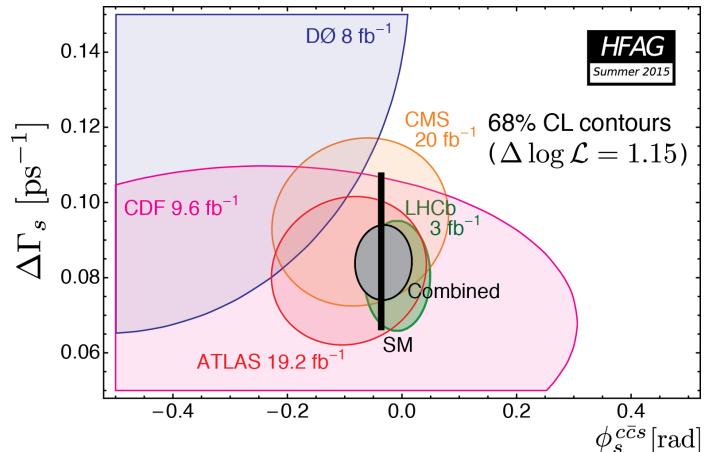


Fig. 16: Contours of 68% confidence level for $\Delta\Gamma_s$ versus the mixing induced CP-violation parameter ϕ_s [57–59]. The SM prediction is indicated by the black vertical bar.

It is interesting to speculate about the “relevance” of the CKM phase. So far, all CP violating effects

measured in particle physics can be reduced to just that phase. On the other hand, there seems to be consensus of opinion among theorists that the CKM induced CP violation in the quark sector is too small by many orders of magnitude to generate the observed baryon asymmetry in the universe (non-zero CKM CP violation requires non-zero and non-degenerate quark masses, so the baryogenesis could only be generated during the electroweak phase transition at critical temperature of $T_c \sim 100$ GeV). So is the CKM phase only an “accident of Nature”? Because there are three quark generations, there is a phase in the quark mixing matrix,¹⁴ and so that phase has “some” value? What would happen to the universe had we a dial to change that value [68]?

Several measurements in the flavour sector exhibit non-significant but interesting anomalies with respect to theory predictions. A prominent example is given by angular coefficients describing the transition $b \rightarrow s\mu^+\mu^-$, the prediction of which, however, are plagued by hadronic uncertainties. Theoretically robust are universality tests. Such tests were performed at the per-mil level at LEP and other e^+e^- colliders not showing any significant discrepancy from the expectation of universal lepton coupling. The B -factory experiments and LHCb have measured ratios of semileptonic B decays among which [69–72] $R_{D^{(*)}} = \mathcal{B}(B^0 \rightarrow D^{(*)}\tau\nu)/\mathcal{B}(B^0 \rightarrow D^{(*)}\ell\nu)$ and $R_K = \mathcal{B}(B^+ \rightarrow K^+\mu^+\mu^-)/\mathcal{B}(B^+ \rightarrow K^+e^+e^-)$. The Heavy Flavour Averaging Group (HFAG) has combined the experimental results giving [73] $R_{D^*} = 0.316 \pm 0.016 \pm 0.010$, which is 3.3σ away from the SM prediction 0.252 ± 0.003 [74]. The two-dimensional combination with R_D increases the deviation to 4.0σ . For R_K LHCb measures at low q^2 (given by the invariant mass of the dimuon or dielectron system) the value $0.745^{+0.090}_{-0.074}(\text{stat}) \pm 0.036(\text{syst})$, which differs by 2.6σ from the expected unity [75].

An intriguing observation in hadron spectroscopy was announced by LHCb in summer 2015 in a paper [76] that collected over 250 citations since. It is the observations of exotic structures in the $J/\psi p$ channel, consistent

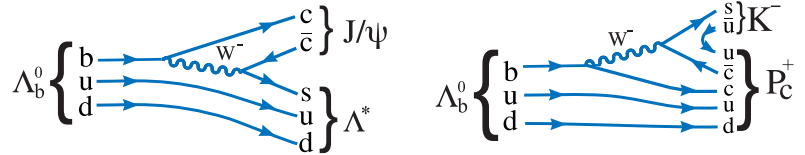


Fig. 17: Feynman graphs for $\Lambda_b^0 \rightarrow J/\psi \Lambda^*$ (left) and $\Lambda_b^0 \rightarrow P_c^+ K^-$ (right).

with pentaquark-charmonium states occurring in $\Lambda_b^0 \rightarrow J/\psi K p$ decays (see Fig. 17 for representative Λ_b^0 decay diagrams). Analysing the full Run-1 data sample and performing an intricate three-body amplitude analysis, the observed structures could only be described by adding two resonances, one with mass and width of $4380 \pm 8 \pm 29$ MeV and $205 \pm 18 \pm 86$ MeV, respectively, and the other (narrower) with mass and width of $4449.8 \pm 1.7 \pm 2.5$ MeV and $39 \pm 5 \pm 19$ MeV. LHCb dubs these two states $P_c(4380)^+$ and $P_c(4450)^+$. The binding mechanism for pentaquarks is not clear at present. They may consist of five quarks tightly bound together, but it is also possible that they are more loosely bound and consist of a three-quark baryon and a two-quark meson interacting relatively weakly in a meson-baryon molecule.

6 Digression on electroweak precision measurements

The global electroweak fit relating observables of the electroweak SM to each other by incorporating precise theoretical predictions of radiative corrections was a masterpiece of the LEP/SLC era. It led to the prediction of the top-quark mass prior to its discovery, provided a strong (logarithmic) constraint on the mass of the Higgs boson, predicting it to be light, and allowed to exclude or constrain models beyond the SM.¹⁵ The discovery of the Higgs boson overconstrains the fit and dramatically improves its

¹⁴ There would be zero (three) phases in a two (four) generations SM, as $n_{\text{phases}} = (n_{\text{gen}} - 1)(n_{\text{gen}} - 2)/2$.

¹⁵For example, it allowed to exclude the simplest technicolour models [77–79]. Technicolour invokes the existence of strong interactions at a scale of the order of a TeV and induces strong breaking of the electroweak symmetry. In the original form of

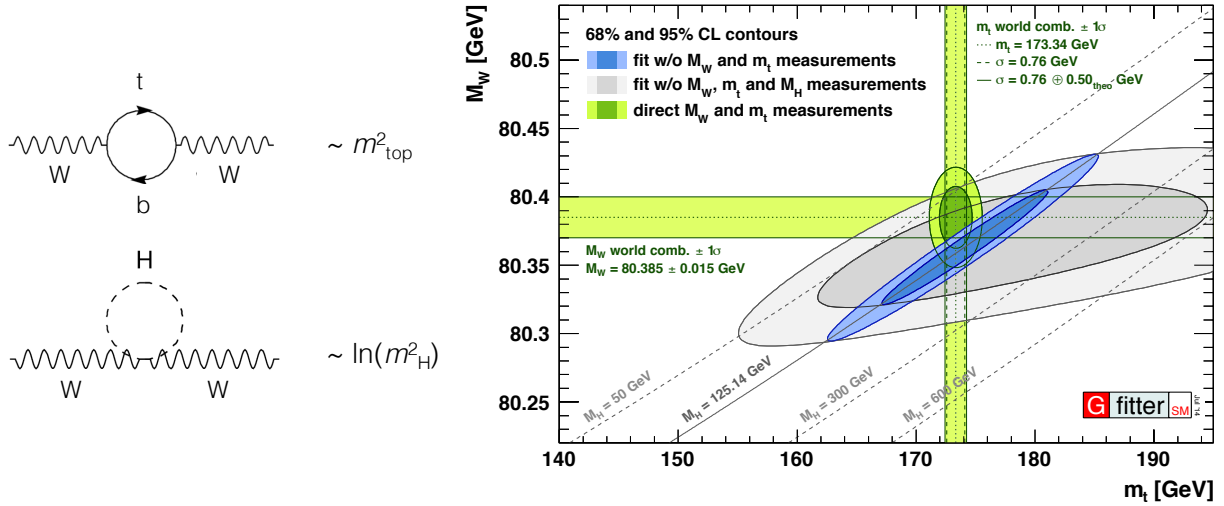


Fig. 18: Left: Feynman graphs of radiative corrections contributing to the W boson mass. The upper (lower) graph introduces a quadratic (logarithmic) top-quark (Higgs-boson) mass dependence. The right panel shows 68% and 95% confidence level contours obtained from scans of fits with fixed variable pairs m_W versus m_t . The narrower blue and larger grey allowed regions are the results of the fit including and excluding the m_H measurement, respectively [80]. The horizontal bands indicate the 1σ regions of the m_W and m_t measurements (world averages).

predictability. The fit has thus turned into a powerful test of the SM.

Figure 18 shows the Feynman graphs of radiative corrections contributing to the W boson mass. They introduce a quadratic top-quark and logarithmic Higgs-boson mass dependence of the correction parameter Δr occurring in the relation

$$m_W^2 = \frac{m_Z^2}{2} \left(1 + \sqrt{1 - \frac{\sqrt{8}\pi\alpha(1 + \Delta r)}{G_F m_Z^2}} \right), \quad (5)$$

owing to electroweak unification. Similarly, the effective weak mixing angle, $\sin^2\theta_{\text{eff}}^\ell$, for lepton flavour ℓ depends on m_W and m_Z and, via radiative corrections and by replacing m_W , on the top-quark and Higgs-boson masses. The current predictions of the observables that most benefit from the known Higgs mass, split into the various uncertainty terms, are [80]

$$\begin{aligned} M_W &= 80.3584 \pm 0.0046 m_t \pm 0.0030 \delta_{\text{theo} m_t} \pm 0.0026 M_Z \pm 0.0018 \Delta\alpha_{\text{had}} \\ &\quad \pm 0.0020 \alpha_S \pm 0.0001 M_H \pm 0.0040 \delta_{\text{theo} M_W} \text{ GeV}, \\ &= 80.358 \pm 0.008_{\text{tot}} \text{ GeV}, \end{aligned} \quad (6)$$

and

$$\begin{aligned} \sin^2\theta_{\text{eff}}^\ell &= 0.231488 \pm 0.000024 m_t \pm 0.000016 \delta_{\text{theo} m_t} \pm 0.000015 M_Z \pm 0.000035 \Delta\alpha_{\text{had}} \\ &\quad \pm 0.000010 \alpha_S \pm 0.000001 M_H \pm 0.000047 \delta_{\text{theo} \sin^2\theta_{\text{eff}}^f}, \\ &= 0.23149 \pm 0.00007_{\text{tot}}. \end{aligned} \quad (7)$$

Their total uncertainties of 8 MeV and $7 \cdot 10^{-5}$, respectively, undercut the world average experimental errors of 15 MeV and $16 \cdot 10^{-5}$ [4, 81].

technicolor, the strong interactions themselves trigger electroweak symmetry breaking without the need of a Higgs boson.

The LHC experiments, as do CDF and D0 since long and continuing, are investing efforts into precision measurements of the electroweak observables m_W , m_t , and $\sin^2\theta_{\text{eff}}^\ell$. All are extremely challenging.

6.1 Top-quark mass

There has been significant progress on the top-quark mass measurements at the LHC achieving similar precision as those performed by the Tevatron experiments. The currently most accurate LHC number is the CMS Run-1 combination of measurements, based on the kinematic top mass reconstruction and comparison with MC templates [82], giving $m_t = 172.44 \pm 0.13 \pm 0.47$ GeV, where the first uncertainty is statistical and the second systematic. The ATLAS Run-1 combination, not yet including the lepton + jets, reads $m_t = 172.84 \pm 0.34 \pm 0.61$ GeV [83]. The most recent Tevatron combination is $m_t = 174.34 \pm 0.37 \pm 0.52$ GeV [84] that shows a tension of 2.4σ or more with the CMS result.

While these kinematic mass measurements provide the best current precision on m_t and must be continued, it is also apparent that they approach a difficult systematic uncertainty regime from, mostly, the b -quark fragmentation. A way to improve could be to choose more robust observables with respect to the leading systematic effects at the possible price of loosing statistical power. The dilepton kinematic endpoint is an experimentally clean observable, which has however large theoretical uncertainties [85]. More robust could be the selection of charmonium states [86] or charmed hadrons originating from a b -hadron produced in one of the b -jets. These provide a clean but rare signature.

ATLAS and CMS also indirectly determine the top mass from inclusive and differential cross-section measurements. These are promising approaches benefiting from theoretically well defined observables, which are however not yet competitive with the kinematic methods. They also stronger depend on the assumption that no new physics contributes to the measured cross sections. The currently best top pole mass determination from CMS [87] using a precise Run-1 $e\mu$ -based cross-section measurement is $173.8_{-1.8}^{+1.7}$ GeV in agreement with the direct (kinematic) measurements.

6.2 Weak mixing angle

The CDF, D0 [91] and LHC experiments [88–90] have extracted the weak mixing angle from Z/γ^* polarisation measurements. The total uncertainty on $\sin^2\theta_{\text{eff}}^\ell$ at the Tevatron is dominated by statistical effects, that of LHCb has similar statistical and systematic contributions, while for ATLAS and CMS parton density function (PDF) uncertainties are dominant. A data-driven “PDF replica rejection” method applied by CDF allows to reduce the sensitivity to PDF and update the measurement when improved PDF sets are available. Overall, these are complex measurements (in particular with respect to the physics modelling) that are important to pursue also in view of a better understanding of Z/γ^* production at hadron colliders. The precision obtained is however not yet competitive with that of LEP/SLC.

6.3 W-boson mass

The W boson was discovered at CERN’s SPS in 1983. A first measurement of its mass by the UA1 experiment in 1983 at centre-of-mass energy of 546 GeV gave $m_W = 81 \pm 5$ GeV [65]. In 1992, at $\sqrt{s} = 630$ GeV UA2 achieved 80.35 ± 0.37 GeV using m_Z from LEP as reference calibration [66]. A factor of ten improvement in precision was obtained at LEP with the most recent combination giving 80.376 ± 0.033 GeV. That precision has been undercut by the Tevatron experiments whose latest average, using proton–antiproton collision data taken at $\sqrt{s} = 1.96$ TeV, is 80.387 ± 0.016 GeV. The combination of the Tevatron and LEP results leads to the present world average $m_W = 80.385 \pm 0.015$ GeV [4, 81].

While the LEP analyses are final, the Tevatron experiments are continuing to improve their precision and updated results can be expected in the future.

It likely came as a surprise to many in the particle physics community that such a precision measurement is now dominated by a hadron collider, which was not built with that goal in mind. The W boson mass is arguably the hardest measurement in high-energy physics, needing about seven years to be accomplished. Also the LHC was not built to measure the W boson mass, but to discover new particles. There is an unfavourable environment at the LHC compared to e^+e^- or proton–antiproton colliders. At the Tevatron, W boson production is dominated by the valence quarks of the proton. At the LHC on the contrary, sea and thus heavy quarks are much more important. This difference affects all aspects of the measurement: detector calibration, transfer from the Z to the W boson, PDF uncertainties, W polarisation, modelling of the W transverse momentum. It is thus a very challenging undertaking, but also a very interesting one: a lot can be learned on the way!

The measurement of the W -boson mass at the LHC using the leptonic W boson decay relies on an excellent understanding of the final state. The observables that probe m_W are the transverse momentum of the lepton ($p_{T,\ell}$), the transverse momentum of the neutrino ($p_{T,\nu}$), measured from the transverse recoil of the event, and the transverse mass of the lepton-neutrino system (m_T). The measurement requires a high-precision momentum and energy scale calibration (including the hadronic recoil) obtained from Z , J/ψ and Υ data, and excellent control of the signal efficiency and background modelling. The biggest challenge is posed by the physics modelling. The production is governed by PDF and initial state interactions (perturbative and nonperturbative), that can be constrained by W^+ , W^- , Z , and $W + c$ data, and the use of NNLO QCD calculations including soft gluon resummation. The experimental m_W probes are very sensitive to the W polarisation (and hence to PDF, including its strange density). Electroweak corrections are sufficiently well known.

The experiments are thriving to address the above issues. Many precision measurements (differential Z , $W + X$ cross sections, polarisation analysis, calibration performance, etc.) are produced on the way with benefits for the entire physics programme. Theoretical developments are also mandatory. Altogether this is a long-term and iterative effort.

CMS presented for the first time a m_Z measurement using a W -like $Z \rightarrow \mu^+\mu^-$ analysis where one muon is replaced by a neutrino that contributes to the missing transverse momentum in the event [92]. It represents a proof-of-principle, although differences with the full m_W analysis remain in the event selection, the background treatment and most of the physics modelling uncertainties. CMS used the 7 TeV dataset to take benefit from the lower number of pileup interactions. The momentum scale and resolution calibration for that measurement relies on J/ψ and Υ data. Track-based missing transverse momentum is used and the W transverse recoil is calibrated using $Z + \text{jets}$ events. The results for the different probes and the positive and negative W -like cases are found to agree with the LEP measurement. The uncertainties, depending on the probe used, are: statistical: 35–46 MeV, total systematic: 28–34 MeV, QED radiation: ~ 23 MeV (dominant), lepton calibration: 12–15 MeV.

ATLAS and CMS use precise measurements of the Z boson p_T to tune the p_T modelling of the W boson, which relies on NNLO and NNLL/resummed calculations. But: different generators predict different transfers from Z to W . In addition, PDFs play different roles in Z and W production. Figure 19 shows normalised differential cross section ratios measured by ATLAS [93] of resummed NLO predictions from ResBos¹⁶ [94] to data (left) and NNLO predictions using the DYNNLO programme¹⁷ [95] without

¹⁶ResBos features ISR at approximate NNLO, γ^* - Z interference at NLO, NNLL soft-gluon resummation, no FSR or hadronic event activity, CT14 PDF set.

¹⁷DYNNLO features QCD production at NNLO, no soft-gluon resummation, CT10 PDF set.

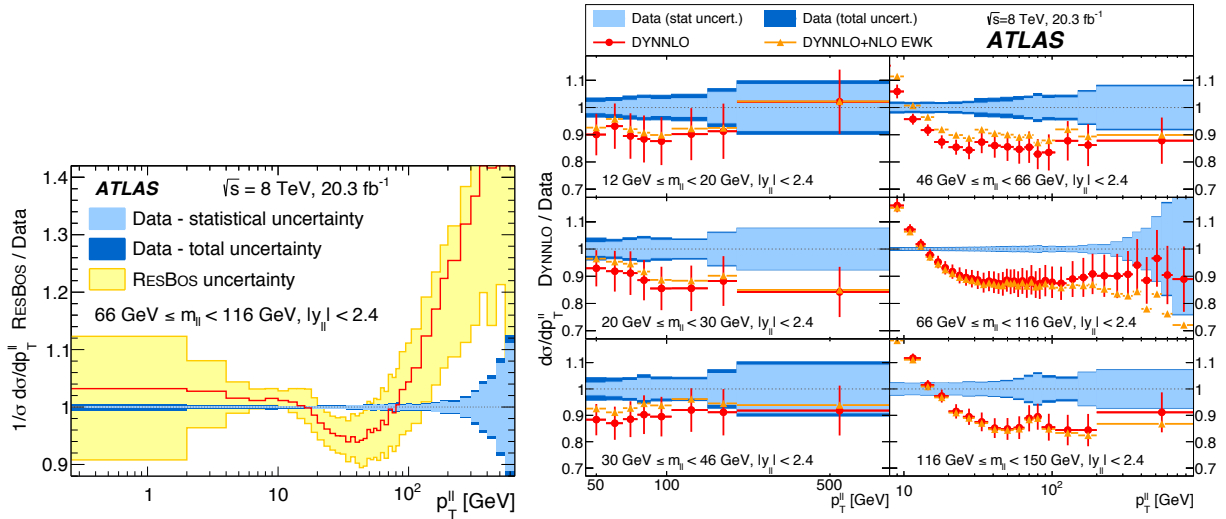


Fig. 19: Left: ratio of ResBos predictions of the normalised differential p_T^Z cross section to ATLAS Born-level data [93]. Right: the same ratio for different Z rapidity intervals and by using the DYNLO programme for the theoretical prediction.

soft gluon resummation to data (right). While resummation is needed to describe the low- p_T data, NLO calculations and better are required in the high- p_T regime.

7 The SM is complete

Since the LHC Run-1 the SM is a complete and self-consistent theory. The discovery of the Higgs boson is a triumph for the imagination and rigour of the scientific endeavour. It is also a triumph for the greatest experimental undertaking ever, at the frontier of accelerator and detector technologies, global data sharing, analysis and collaboration.

The Higgs mass of 125.1 GeV is in agreement with the prediction from the global electroweak fit [96] (cf. left panel of Fig. 20) and it lies marginally within the requirement for vacuum stability [97] (right panel of Fig. 20). The Higgs discovery does thus not come with a strict requirement for new physics below the Planck scale.

We have now two beautiful and extremely precise theories. On one hand the SM describing electroweak and strong interactions (though not their unification), predicting, eg., the anomalous magnetic moment of the electron to a relative precision of 10^{-10} in agreement with experiment. On the other hand there is general relativity, the theory of gravitation. It has been tested to an accuracy of order 10^{-5} (Cassini probe [98]). Unfortunately, the SM and general relativity do not work in regimes where both are important, that is at very small scales.

Indeed, many open questions not addressed by the SM remain as we have already alluded to in the introduction to these proceedings. We shall repeat some of them here.

- **Scalar sector.** Is there a single Higgs doublet or are there additional scalar states? Is the Higgs boson elementary or composite? What is the exact form of the scalar potential? What is the origin of the Yukawa couplings?
- **Quarks and leptons.** What is the origin of the fermion generations, mass, mixing, CP violation?

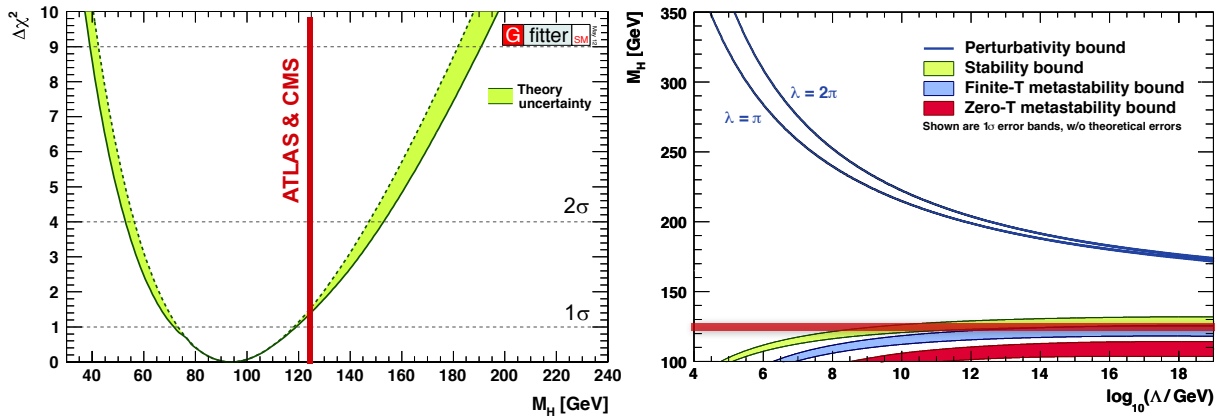


Fig. 20: Left: χ^2 curve obtained from the global electroweak fit in 2012 at the moment of the Higgs boson discovery [96]. Right: comparison of the observed Higgs mass with the lower limits from the vacuum stability constraint and the upper perturbativity limit [97].

How was the matter–antimatter asymmetry in the universe generated? What is the origin of baryon and lepton number conservation and what is the proton lifetime?

- **Neutrinos.** What is the nature of the neutrinos: Majorana or Dirac? Are there sterile neutrinos? What is the origin of neutrino mass and what are their values (and hierarchy)? Is there CP violation in the neutrino mixing?
- **Strong CP problem.** Why is there no noticeable CP violation in strong interactions albeit predicted by the SM?
- **Dark matter.** What is its composition: WIMPs, axions, sterile neutrinos, hidden sector particles, gravitational effect only? Is there a single or are there multiple sources?
- **Expansion of Universe.** Primordial expansion via inflation: which fields, and what is the role of the Higgs boson and of quantum gravity? Accelerated expansion today: cosmological constant problem.
- **High-scale physics.** Is there a solution to the hierarchy problem¹⁸ and is there new physics at the TeV scale? Will there be grand unification of the forces? How does unification with gravity proceed? How is quantum gravity realised? Is everything just made of tiny strings?

Because the SM cannot be all there is, the LHC experiments have performed a large number of searches for new physics during Run-1, covering a vast space of possible signatures as witnessed in the exclusion plots of Fig. 21. Heavy resonances are excluded up to 3.5 TeV mass in some scenarios. Gluinos up to 1.3 TeV are excluded for light neutralinos (supersymmetry limits are usually lower than those of many other new physics scenarios because R -parity conservation requires pair production of supersymmetric particles).

¹⁸The term hierarchy problem stands for the apparent dependence of phenomena at the electroweak scale on a much higher (possibly the Planck) scale, as exemplified by the extreme ultra-violet sensitivity of the Higgs potential.

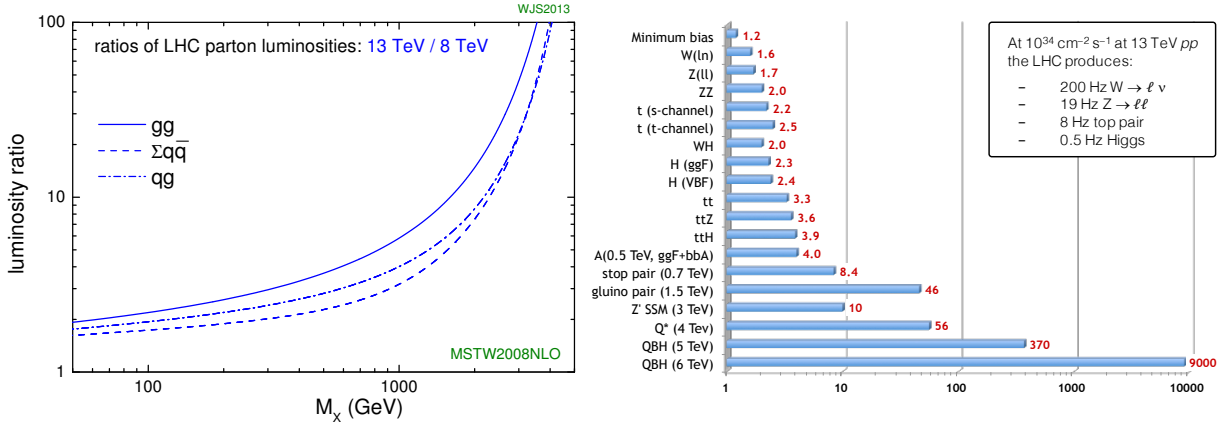


Fig. 22: Left: parton luminosity ratio of 13 TeV to 8 TeV proton–proton collisions [11]. Right: cross section ratios for selected processes (the heavy flavour cross section scales roughly linearly with centre-of-mass energy).

8 The LHC Run-2

A huge milestone was achieved in 2015 when the new record proton–proton collision energy of 13 TeV was reached. After a rocky start, the LHC delivered 4.2 fb^{-1} integrated luminosity to ATLAS and CMS. That amount of data already surpassed the Run-1 new physics sensitivity of many searches. During 2016 a peak luminosity of $1.4 \cdot 10^{34} \text{ cm}^{-2}\text{s}^{-1}$ was reached and a total of 39 fb^{-1} integrated luminosity delivered, which exceeded expectations.

The new centre-of-mass energy increases the cross-section of all LHC processes. Figure 22 gives the 13 TeV to 8 TeV parton luminosity ratios for gluon–gluon, quark–gluon and quark–quark scattering (left panel) and the resulting proton–proton cross-section ratios (right). The parton luminosity as a function of the hard scattering $Q^2 = M_X^2$ (cf. Fig. 3) is defined by the convolution integral

$$\frac{\partial \mathcal{L}_{ab}}{\partial M_X^2} = \frac{1}{s} \int_{\tau}^1 \frac{dx}{x} f_a(x, M_X^2) f_b(\tau/x, M_X^2), \quad (8)$$

where $\tau = M_X^2/s$. There is a larger parton luminosity increase with energy for gluon initiated processes than for quark ones. Owing to the important cross section rise at large M_X the early Run-2 analyses put their emphasis on searches.

Most of the results from ATLAS and CMS presented at the 2016 summer conferences contained data up to approximately 15 fb^{-1} . CMS used different software releases and thus did not merge the 2015 and 2016 datasets, but in selected cases provided a statistical combination. ATLAS performed a reprocessing of the 2015 data and MC allowing it to treat both years as a single coherent dataset. LHCb performed luminosity levelling leading to an approximately ten times smaller dataset in terms of integrated luminosity. The uncertainty on the luminosity values from ATLAS, CMS and LHCb, for the summer 2016 results were 2.9%, 6.2% and 3.8%, respectively. The amount of pileup interactions with an average μ (cf. Eq. 3) of 23 interactions was similar to that in 2012. LHCb observed 1.7 pileup interactions in average.

8.1 Standard Model and top-quark physics

Along increasing scattering momentum transfer, SM processes the LHC can be split the as follows.

- **Soft QCD:** study of particle spectra. The transverse momenta are typically smaller than a few GeV. More than 99.999% of the proton–proton collisions belong to that type. Measurements of

soft QCD processes serve to probe LO matrix elements, parton shower models, generator tunings, and for pileup modelling.

- **Hard QCD:** study of jets. Typical jet p_T greater than tens of GeV up to the TeV scale; approximately 10^{-5} of the collisions belong to that category. The measurements probe NLO QCD, the running α_s , PDFs, parton showers, etc.
- **Hard QCD and electroweak processes:** W , Z , H , top decaying to stable identified particles. Typical p_T scale of greater than tens of GeV ; a fraction of 10^{-6} and less of the collisions belong to this category. Measurements probe NLO, NN(N)LO QCD, soft gluon resummation, PDFs, electroweak physics, etc.

Standard Model and Higgs precision measurements are key to the LHC programme up to the High-Luminosity LHC (HL-LHC). Michelangelo Mangano at the SEARCH 2016 workshop [99] summarised the importance of these measurements as follows.

- **Scientific perspective.** No matter what BSM the LHC will unveil in the next years, improving the knowledge of Higgs properties is a must, which by itself requires and justifies the largest possible LHC statistics so that stopping after 300 fb^{-1} would not be satisfying.
- **Pragmatic perspective.** Higgs and SM physics are the only guaranteed deliverables of the LHC programme. Need to exploit this part of the programme to its maximum extent!
- **Utilitarian perspective.** Elements of the SM, besides the Higgs, require further consolidation, control and improved precision, both in the EW and QCD sectors. They hold a fundamental value (eg. the precise determination of parameters of nature and to better understand detailed scattering dynamics), or are critical to fully exploit the BSM search potential (eg. the knowledge of backgrounds, production rates and production dynamics).
- **Spinoffs.** The study of SM processes at colliders is typically more complex than the search for BSM signatures and throughout the years it has been the main driver of fundamental theoretical innovation.

8.1.1 Inelastic proton–proton cross section

A key initial measurement is the inclusive inelastic cross-section at 13 TeV. While the most precise total cross section measurement is obtained via elastic scattering and the optical theorem ($\sigma_{\text{tot}}(pp \rightarrow X) \propto \text{Im}f_{\text{elastic}}(t \rightarrow 0)$, where $f_{\text{elastic}}(t \rightarrow 0)$ is the elastic scattering amplitude extrapolated to the forward direction, and t is the Mandelstam momentum transfer variable) using dedicated forward devices (such measurements have achieved better than 1% precision in Run-1, dominated by the luminosity uncertainty [100, 101]); it is also possible to determine $\sigma_{\text{tot}}(pp \rightarrow X)$ from a measurement of inelastic scattering cross section if the extrapolation between fiducial to total acceptance is not too large. This can be achieved using forward detectors such as scintillators installed in ATLAS within $2.07 < |\eta| < 3.86$.

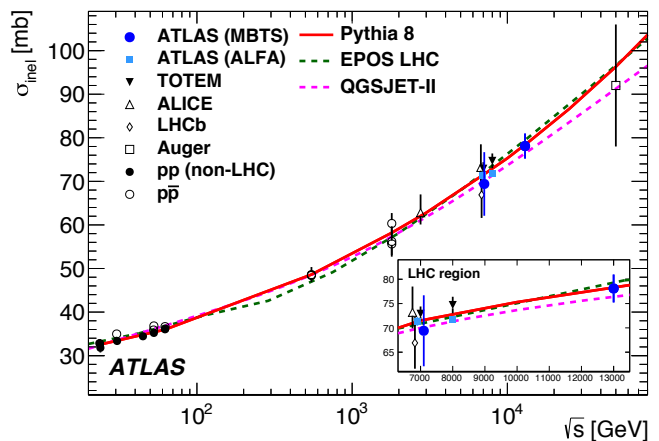


Fig. 23: Inelastic proton–proton cross section versus centre-of-mass energy [102].

The ATLAS measurement [102] was performed in the fiducial region $\xi = M_X^2/s > 10^{-6}$, where M_X is the larger invariant mass of the two hadronic (proton-dissociation) systems separated by the largest rapidity gap in the event. In this ξ range the scintillators have high efficiency. When extrapolated to the full phase space, a cross-section of $\sigma_{\text{tot}}(pp \rightarrow X) = 78.1 \pm 0.6 \pm 1.3 \pm 2.6$ mb is obtained, where the first uncertainty is experimental, the second due to the luminosity, and the third and dominant one from the extrapolation to full phase space. The result is consistent with the expectation from phenomenological models (cf. Fig. 23, where also measurements from other hadron collider experiments and from the Pierre Auger experiment are shown, see references in [102]).

8.1.2 Jet production

Moving up in transverse momentum, ATLAS and CMS measured jet production. Figure 24 shows the double differential inclusive jet cross section as measured by CMS. The unfolded data points are compared to predictions from NLOJet++ based on the CT14 PDF set and corrected for the nonperturbative and electroweak effects (line in figure). It is interesting to compare Fig. 24 at 13 TeV to the 8 TeV result shown in Fig. 7 on page 15. For a given rapidity interval, the relative drop in cross section between high and low p_T is less pronounced at 13 TeV, as expected from the parton luminosities. Indeed, taking the ratio between the 13 TeV and 8 TeV cross sections approximately reproduces the left panel of Fig. 22 for gluon–gluon scattering.

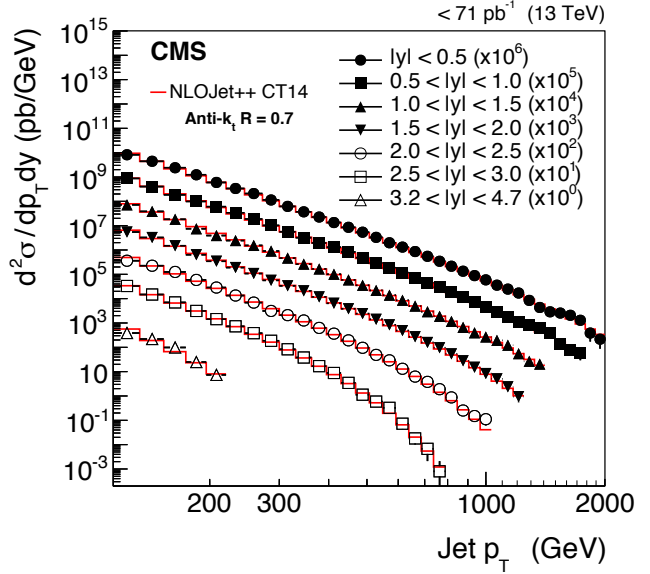


Fig. 24: Double-differential inclusive jet cross section versus jet p_T as measured by CMS at 13 TeV [103] and compared to a theoretical prediction.

8.1.3 Weak boson production

The inclusive W and Z boson production cross sections are expected to rise at 13 TeV over 8 TeV centre-of-mass energy by factors of 1.7 and 1.6, respectively, to 19.7 nb and 1.9 nb for the decays to muons. Leptonic W and Z decays are very pure channels as can be seen from Fig. 25, which shows the transverse and invariant dilepton mass distributions for 13 TeV $W \rightarrow \mu\nu$ (left panel) and $Z \rightarrow ee$ candidates (right). The transverse mass-squared is defined by $m_T^2 = 2p_{T,\ell}E_T^{\text{miss}}(1 - \cos\Delta\phi_{\ell,\nu})$, where $\Delta\phi_{\ell,\nu}$ is the azimuthal angle difference between lepton and missing transverse momentum. The dilepton invariant mass-squared is given by $m_{\ell_1\ell_2}^2 = 2p_{T,\ell_1}p_{T,\ell_2}(\cosh\Delta\eta_{12} - \cos\Delta\phi_{12})$.

Apart from the intrinsic interest in precise cross section measurements, leptonic W and Z decays also serve the experiments as standard candles to calibrate the electron and muon reconstruction performance via mass constraints and so-called tag-and-probe efficiency measurements. Tag-and-probe methods [104] are used to select, from known resonances, unbiased samples of electrons or muons (probes) by using strict selection requirements on the second object produced from the particle's decay (tags). The efficiency of a requirement can then be determined by applying it directly to the probe sample after accounting for residual background contamination.

Both ATLAS and CMS measured fiducial and inclusive cross sections for W and Z boson production as well as their ratios using partial 2015 datasets [105, 106]. The fiducial cross sections are dominated by

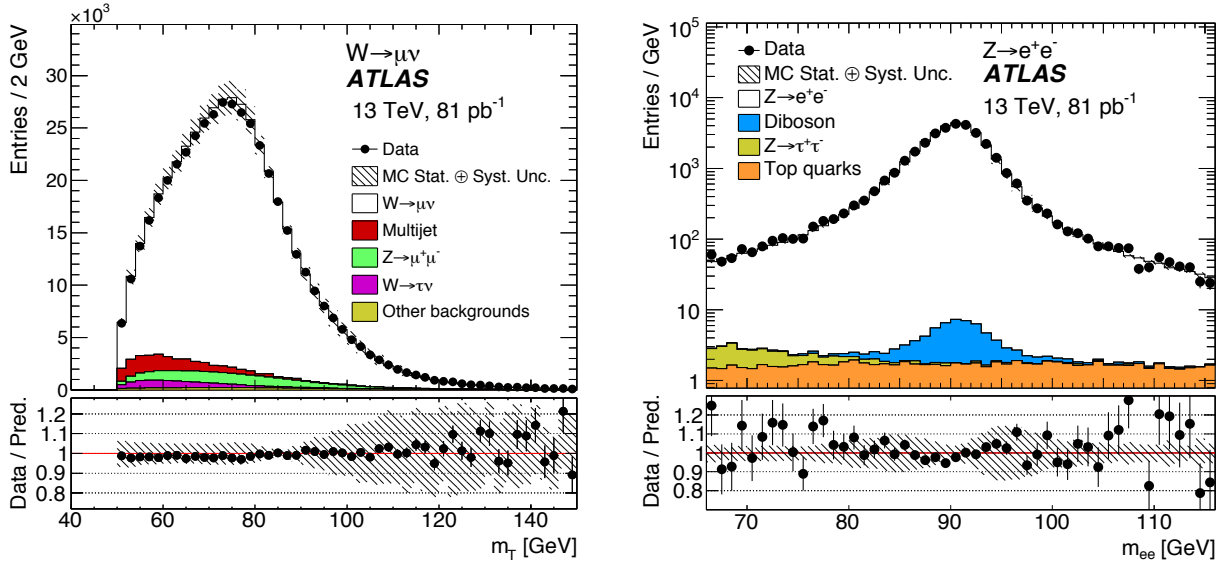


Fig. 25: Transverse mass (left) and invariant dilepton mass (right) for $W \rightarrow \mu\nu$ and $Z \rightarrow ee$ candidates, respectively [105, 106]. The predicted signal distributions are normalised to the measured cross sections.

the luminosity uncertainty of 2.1% (ATLAS). Comparisons of the measured cross-sections with NNLO QCD and NLO EW Drell-Yan predictions show good agreement within uncertainties. Figure 26 shows the energy dependence of the measured inclusive W and Z boson cross sections compared to theoretical predictions. LHCb has measured the 13 TeV Z boson cross section in the fiducial acceptance $2.0 < \eta < 4.5$ and found agreement with the SM prediction [107].

Ratios of cross sections already achieve precision of better than 1–2% owing to a cancellation of systematic uncertainties. They represent powerful tools to constrain PDFs: the W^+/W ratio is sensitive to the low- x u and d valence quarks, and the W^\pm/Z ratio constrains the strange quark PDF, in particular when also using the rapidity distributions. Figure 27 shows the measured and predicted ratios. Fair agreement between the data and most PDF sets is seen. An increased strange quark contribution [108] (towards SU(3) flavour symmetry of sea squarks in the proton) would likely improve the agreement. The right panel in Fig. 27 shows tests of the universality of the first and second generation leptonic couplings to the weak bosons. Lepton universality in the charged current was measured to the 0.14% level at LEP in τ lepton decays, however at low energy (off-shell), so with less sensitivity to new physics in loops.

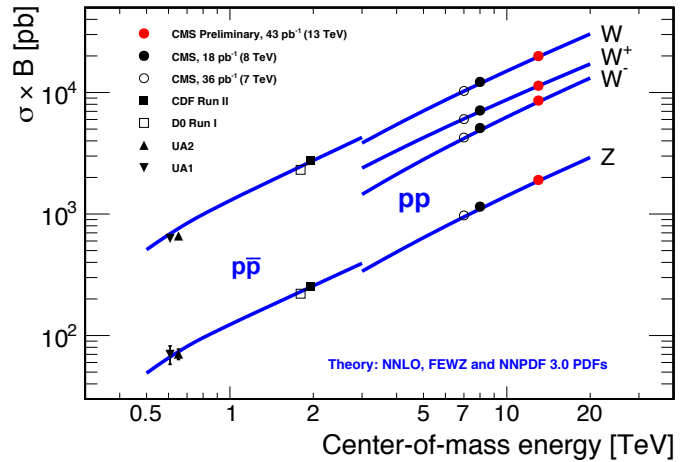


Fig. 26: Cross sections of proton–(anti-)proton production of inclusive W and Z bosons versus centre-of-mass energy.

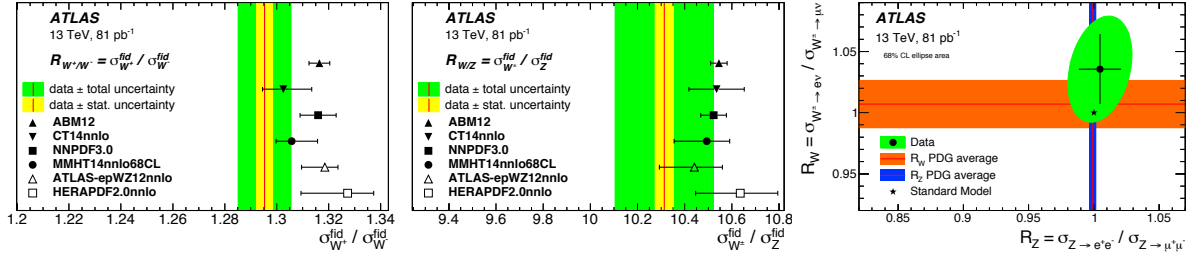


Fig. 27: Ratios of fiducial cross sections compared to various PDF predictions (left and middle panels), and W and Z lepton universality tests (right panel) [111].

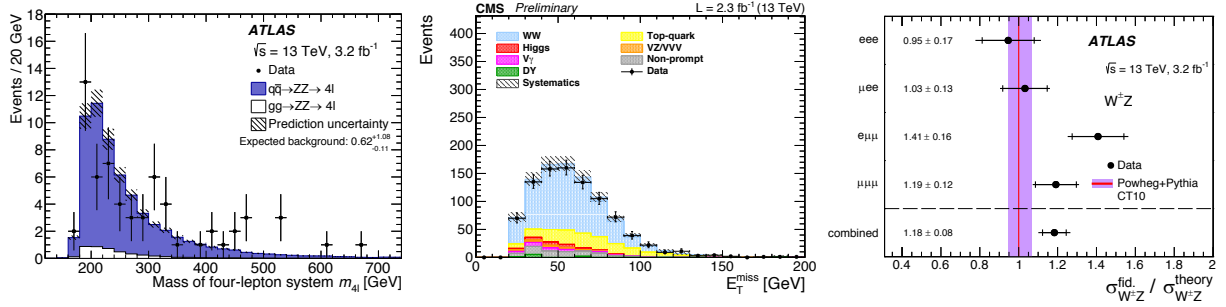


Fig. 28: Distributions from 13 TeV diboson selections. Left: four-lepton invariant mass in the $ZZ \rightarrow 4\ell$ analysis [109]; middle: missing transverse momentum in $WW \rightarrow 2\ell 2\nu$ [110]; right: ratio of measured over predicted (NLO QCD) fiducial cross sections measured in $WZ \rightarrow 3\ell\nu$ [111].

8.1.4 Diboson production

The production of boson pairs is a highly important sector of LHC physics that is intimately related to electroweak symmetry breaking. In the s -channel (Drell-Yan), via photon, Z or W exchange, diboson production is sensitive to anomalous triple gauge boson couplings (aTGC). Triple and also quartic gauge boson couplings, the latter vertices involving the scattering among four gauge bosons, are predicted by the SM as the electroweak gauge bosons carry weak charge (non-Abelian structure of EW theory).

The production of WW and ZZ events was studied at LEP versus the e^+e^- centre-of-mass energy resulting in a famous plot that showed the moderation of the WW cross section versus energy by TGC processes as predicted by the SM (see Fig. 29) [112]. The Tevatron experiments studied a multitude of diboson production processes. ATLAS and CMS performed inclusive, fiducial and differential cross-section analyses at 8 TeV. First fiducial and total cross section measurements at 13 TeV are also available (see Fig. 28 for a selection of representative plots). Inclusive diboson WW , WZ and ZZ events are reconstructed through the leptonic decays of the weak bosons, leading to two-lepton, three-lepton and four-lepton final states, where the former two channels are accompanied by E_T^{miss} . Hadronic weak boson decays are not competitive for inclusive cross section measurements, but are interesting for aTGC searches at high diboson mass where possible new physics effects are expected to show up first

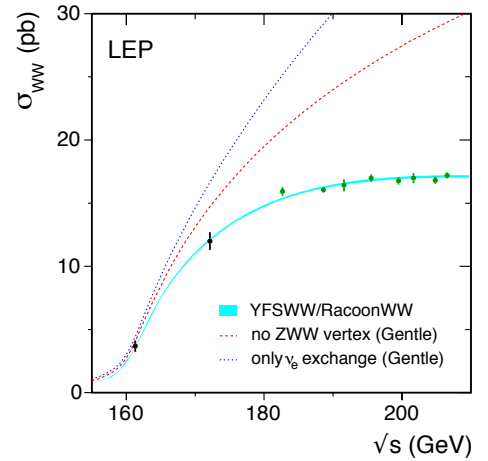


Fig. 29: W pair production cross section measured at LEP compared to the SM predictions [112].

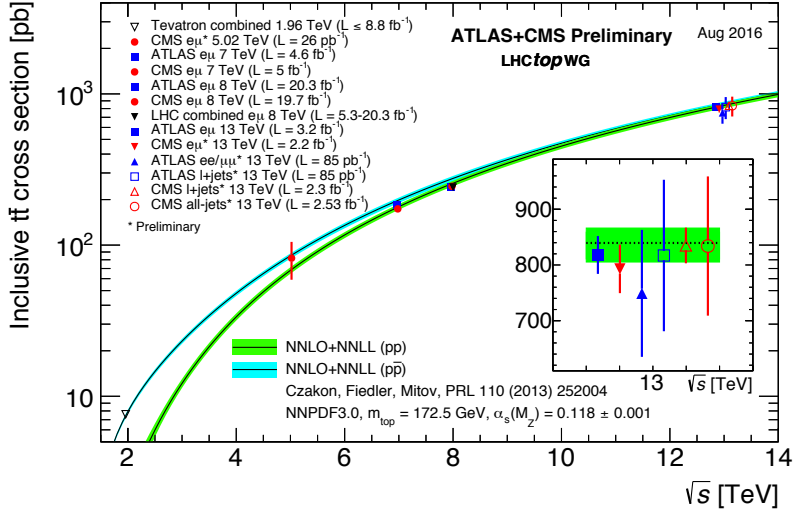


Fig. 30: Summary of LHC and Tevatron measurements of the inclusive top-pair production cross section versus centre-of-mass energy. The bands correspond to predictions with uncertainties from NNLO QCD calculations including NNLL soft gluon resummation. Measurements and theory calculations assume $m_t = 172.5$ GeV.

(see [113] for a recent review). These results show that NNLO QCD is needed to match the data, and, in case of $WW \rightarrow 2\ell 2\nu$ measured in an exclusive zero-jet channel, higher-logarithmic-order (NNLL) soft gluon resummation.

8.1.5 Top production

Top-antitop production at the LHC is dominated by gluon-gluon scattering in the initial state. A factor of 3.3 cross-section increase at 13 TeV centre-of-mass energy compared to 8 TeV is expected. The inclusive $pp \rightarrow t\bar{t} + X$ cross section can be robustly measured using dilepton events selecting different lepton flavours to suppress Drell-Yan background. A method applied successfully during Run-1 allows to simultaneously determine the $t\bar{t}$ cross section and b -tagging efficiency from data [114]. We shall briefly discuss it here for the corresponding 13 TeV measurement as it is an instructive example for a straightforward experimental approach relying where possible on data.

The method employs an exclusive selection of $e\mu$ events with one and two b -tags. The observed number of events is given by $N_1 = L \cdot \sigma_{t\bar{t}} \cdot \epsilon_{e\mu} \cdot 2\epsilon_b \cdot (1 - C_b \cdot \epsilon_b) + N_1^{\text{bkg}}$ and $N_2 = L \cdot \sigma_{t\bar{t}} \cdot \epsilon_{e\mu} \cdot C_b \cdot \epsilon_b^2 + N_2^{\text{bkg}}$, where $N_{1(2)}$ is the number of observed events with one (two) b -tags, L the integrated luminosity of the analysed data sample, $\epsilon_{e\mu}$ the combined $t\bar{t} \rightarrow e\mu + X$ selection acceptance and efficiency determined from MC, ϵ_b the probability to b -tag q from $t \rightarrow Wq$ determined from data (ϵ_b includes the selection acceptance and efficiency), and $C_b = \epsilon_{bb}/\epsilon_b^2$ is a small non-factorisation correction (1.002 ± 0.006) determined from MC. The selection of $t\bar{t} \rightarrow e\mu + X$ events is very pure with, for the ATLAS 2015 dataset (3.2 fb^{-1}), $N_1 = 11958$, $N_2 = 7069$, and $N_1^{\text{bkg}} = 1370 \pm 120$, $N_2^{\text{bkg}} = 340 \pm 88$ event counts [115]. The background is dominated by the Wt single-top process. Solving the equations simultaneously for $\sigma_{t\bar{t}}$ and ϵ_b gives: $\sigma_{t\bar{t}} = 828 \pm 8 \pm 27 \pm 19 \pm 12 \text{ pb}$, where the first error is statistical, the second systematic, and the third (fourth) due to the luminosity (beam-energy) uncertainty.¹⁹ The total relative uncertainty of 4.4% is already

¹⁹The LHC beam energy during the 2012 proton-proton run was calibrated to be $0.30 \pm 0.66 \%$ below the nominal value of 4 TeV per beam. That estimate, dominated by systematic uncertainties, was made by measuring the revolution frequency, that is, the speed difference of protons and lead ions during proton-lead runs in early 2013 [116], taking advantage of the simultaneous presence of both particle types with the same orbits in the LHC. The measurement result agrees with the beam energy derived from the magnetic calibration curves of the dipole magnets that are used to generate the current settings of the

comparable with the 4.3% obtained at 8 TeV. The measurement is in agreement with the theoretical prediction of 832^{+40}_{-46} pb, based on NNLO QCD including NNLL soft gluon resummation and of similar precision as the measurement. The systematic uncertainty affecting the measurement (total 3.3%) is dominated by theoretical sources in particular the modelling of nonperturbative effects related to parton showering and hadronisation. It is interesting (though not mandatory for the method to work) to observe that the resulting value for $\epsilon_b = 0.559 \pm 0.004 \pm 0.003$ is in agreement with the value of 0.549 found in MC simulation. Figure 30 shows a summary of various LHC and Tevatron $t\bar{t}$ cross section measurements versus centre-of-mass energy, and compared to theoretical predictions. The $e\mu$ method provides the most precise inclusive results at all LHC centre-of-mass energies.

The experiments also performed first differential cross section measurements at 13 TeV which show reasonable modelling although deviations at large jet multiplicity and top p_T persist, similar to those seen in Run-1.

Electroweak single-top production (cf. Feynman graphs in Fig. 11) amounts, in case for the dominant t-channel, to about one third of the $t\bar{t}$ production cross section and is expected to increase by a factor of 2.5 at 13 TeV compared to 8 TeV. A summary of the inclusive cross section measurements for all available centre-of-mass energies is displayed in Fig. 31 (see [117–119] for the 13 TeV results). Agreement with theoretical predictions based on pure NLO QCD, NLO QCD complemented with NNLL resummation, and NNLO QCD (t-channel only) is observed. In the t-channel, also the charge asymmetries are measured at 13 TeV and found in agreement with the SM prediction (the ratio of tq to $\bar{t}q$ production is measured to be 1.72 ± 0.20). The s-channel is challenging at the LHC and requires more data.

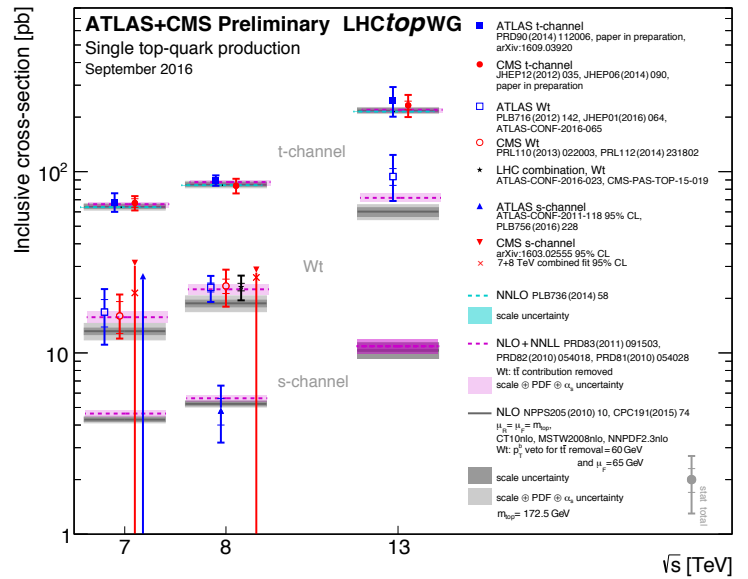


Fig. 31: Summary of ATLAS and CMS measurements of single-top production cross sections versus centre-of-mass energy. The measurements are compared to theoretical calculations (see text for details).

The opening of the phase space at 13 TeV allows to produce heavier final states, such as the associated production of $t\bar{t}$ with a W or Z boson (cf. Feynman graphs in Fig. 10 on page 16). Because of different production mechanisms (dominantly gluon s-channel scattering in case of ttZ and t-channel quark–antiquark annihilation for ttW) the 13 TeV to 8 TeV cross-section ratios are different for the two channels: 3.6 for ttZ compared to only 2.4 for ttW . Both experiments have produced first inclusive 13 TeV cross section results [120, 121] finding for ttW : 1.5 ± 0.8 pb (ATLAS) and $0.98^{+0.32}_{-0.28}$ pb (CMS), and for ttZ : 0.9 ± 0.3 pb (ATLAS) and $0.70^{+0.21}_{-0.19}$ pb (CMS). The corresponding SM predictions are 0.60 ± 0.08 pb (ttW) and 0.84 ± 0.09 pb (ttZ). Both, ATLAS and CMS are slightly on the high side for ttW reproducing a similar pattern already observed in the Run-1 data. Improving these results is important in its own rights, but also because the ttW/Z channels are important backgrounds to ttH in final states with multiple leptons, where in particular ttW is difficult to separate.

power converters which feed the magnets during beam operation. The magnetic calibration is expected to be accurate within an uncertainty of about 0.07%, which is significantly better than the measurement uncertainty based on proton–lead data.

8.2 Reobservation of the Higgs boson at 13 TeV

The expected 13 TeV to 8 TeV cross section ratios amount to 2~2.4 for VH , ggH , VBF, and 3.9 for ttH production. The combination of the 2015 and 2016 data available by the 2016 summer conferences should therefore already achieve similar or better significance and precision on Higgs boson production than in Run-1.

Figure 32 shows a rare and beautiful VBF $H \rightarrow 4\ell$ candidate event. Such an event has large signal to background probability. Preliminary results for the cleanest bosonic channels $H \rightarrow 4\ell$ and $H \rightarrow \gamma\gamma$ were released by ATLAS and CMS for the 2016 summer conferences [122–125]. The Higgs boson was reobserved with high significance at the expected mass in both channels by either experiment (cf. Fig. 33 for the corresponding diphoton and four-lepton mass spectra). The extracted inclusive cross sections have still large uncertainties and are found in agreement with the SM expectations. In the four-lepton channel, ATLAS found a cross section of 81^{+18}_{-16} pb compared to 55 ± 4 pb expected. CMS measured a signal strength of $\mu_{H \rightarrow 4\ell} = 0.99^{+0.33}_{-0.26}$ pb. CMS also measured the mass to be $m_H = 124.50^{+0.48}_{-0.44}$ GeV in agreement with the Run-1 ATLAS and CMS combined value of 125.09 ± 0.24 GeV. In the diphoton channel signal strengths of $\mu_{H \rightarrow \gamma\gamma} = 0.85^{+0.22}_{-0.20}$ and 0.91 ± 0.21 are measured by ATLAS and CMS, respectively. The measured cross sections versus centre-of-mass energy are shown in Fig. 34 for the inclusive cases (ATLAS, left) and fiducial measurements (CMS, right). ATLAS has combined the 4ℓ and $\gamma\gamma$ results to perform a coupling analysis [126]. The combined inclusive cross section is also shown on the left panel of Fig. 34. The experiments also measured differential cross sections that are compared to NNLO plus parton shower predictions. No deviation from the SM prediction is found within yet large uncertainties.

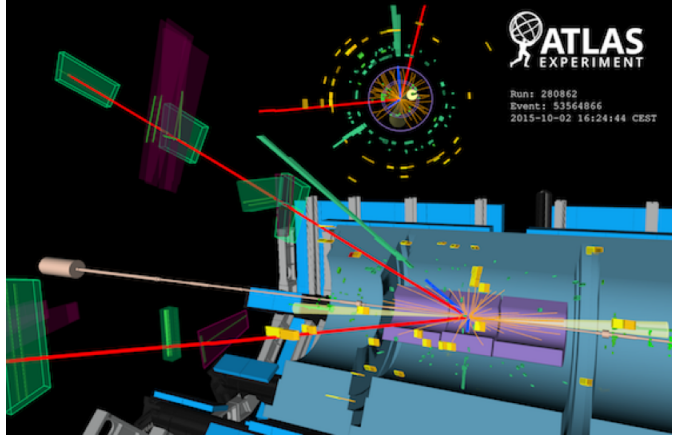


Fig. 32: Display of $H \rightarrow ee\mu\mu$ candidate from 13 TeV pp collisions measured by ATLAS. The event is accompanied by two forward jets with pseudorapidity difference of 6.4 and invariant dijet mass of 2 TeV. This event is consistent with VBF production of a Higgs boson decaying to four leptons.

ATLAS also released first preliminary studies of associated VH production with the decay $H \rightarrow bb$ [127]. The channel is very challenging due to large backgrounds that need to be controlled with high precision in order to extract the signal. Run-1 had provided a signal strength slightly below the SM expectation [45, 128, 129]. The Run-2 yield was again low with $\mu_{VH(\rightarrow bb)} = 0.21^{+0.51}_{-0.50}$ after combining the zero, one, and two charged lepton final states covering the ZH and WH modes.

ATLAS also looked into inclusive production of $H \rightarrow \mu\mu$ [130] that has an expected branching fraction of 0.02%, but might be enhanced due to new physics effects. The sensitivity to that decay depends primarily on the dimuon mass resolution. The sensitivity can be improved, similarly to that of $H \rightarrow \gamma\gamma$, by splitting the event sample into categories with different mass resolution and/or signal-to-background ratios, such as low versus high p_T , central versus forward muons, ggF versus VBF, etc. The observed 95% confidence level limit for $H \rightarrow \mu\mu$ is found at 4.4 times the SM prediction, reducing to 3.5 when combined with Run-1. About 300 fb^{-1} are needed to reach SM sensitivity. These results allow to exclude a universal Higgs coupling to fermions, as $H \rightarrow \mu\mu$ would have been observed had it the same branching fraction as $H \rightarrow \tau\tau$.

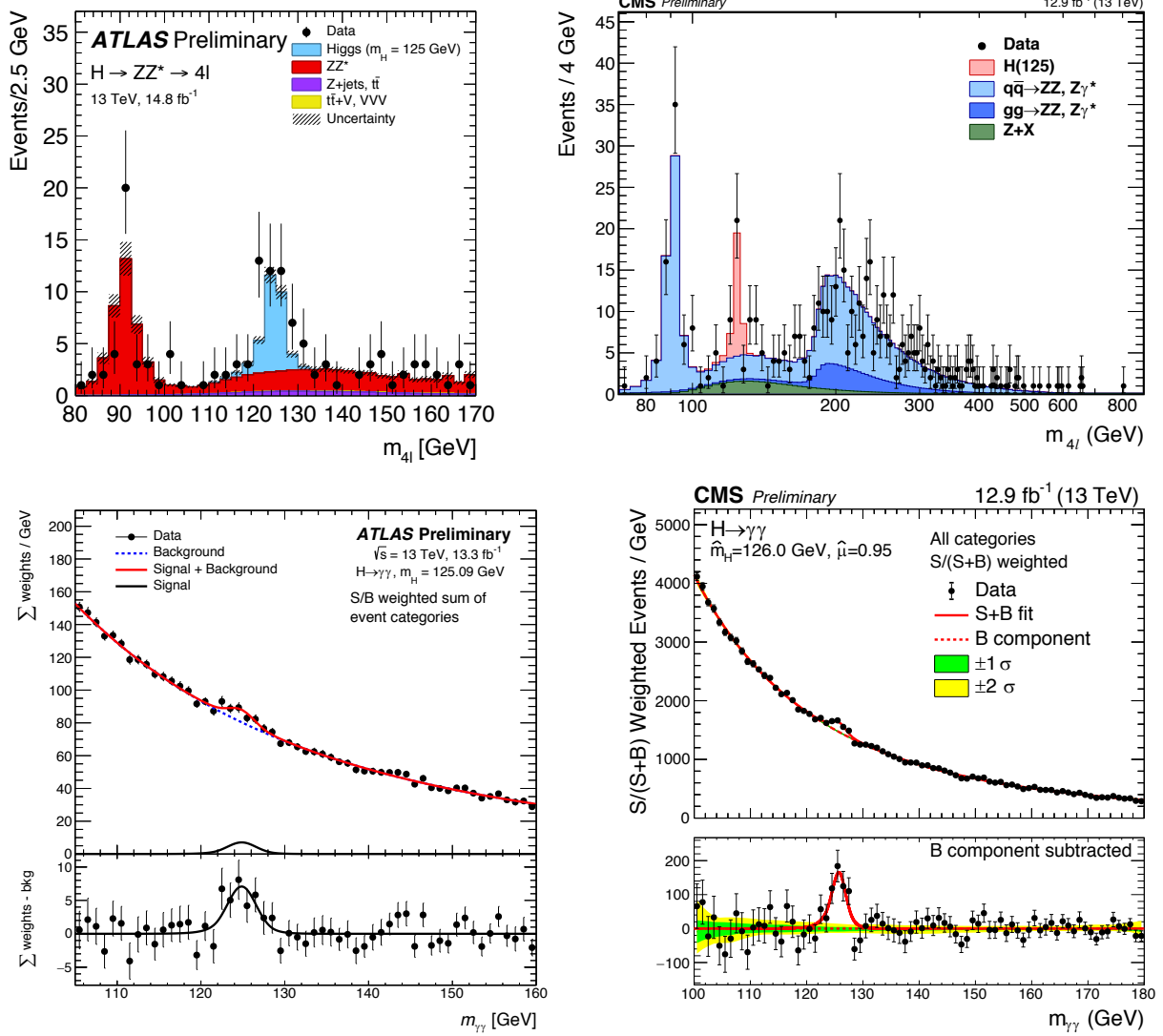


Fig. 33: Four-lepton (top row) and diphoton (bottom row) invariant mass distributions for ATLAS (left column) and CMS (right column) for the combined 2015 and 2016 datasets (ATLAS) and 2016 dataset (CMS) taken at 13 TeV proton–proton centre-of-mass energy [122–125]. The bottom plots show each event weighted by the signal-to-background ratio of the event category it belongs to.

The Higgs production mode that most benefits from the increased centre-of-mass energy is ttH that was found a bit enhanced compared to the SM prediction in the Run-1 Higgs couplings combination (cf. Fig. 14, page 19). The motivation was thus large to look for that mode in Run-2.

The associated production of ttH is the only currently accessible channel that directly measures the top–Higgs coupling (cf. Feynman graph in Fig. 12 on page 18). All major Higgs decay channels, $\gamma\gamma$, multileptons, and bb , are analysed, where in particular the latter two channels represent highly complex analyses. The multilepton mode targets Higgs decays to $\tau\tau$, $WW \rightarrow 2\ell 2\nu$, and $ZZ \rightarrow 2\ell 2\nu$, 4ℓ together with at least one top quark decaying leptonically. It requires at least two leptons with the same charge, which greatly reduces SM backgrounds. The dominant remaining backgrounds are misidentified prompt leptons and ttV production in particular the difficult to separate ttW (cf. the right panel in Fig. 35 for the distribution of a boosted decision tree trained to distinguish ttW background from ttH signal). The $H \rightarrow bb$ mode is analysed in the one and two lepton channels. Here the biggest challenge represents

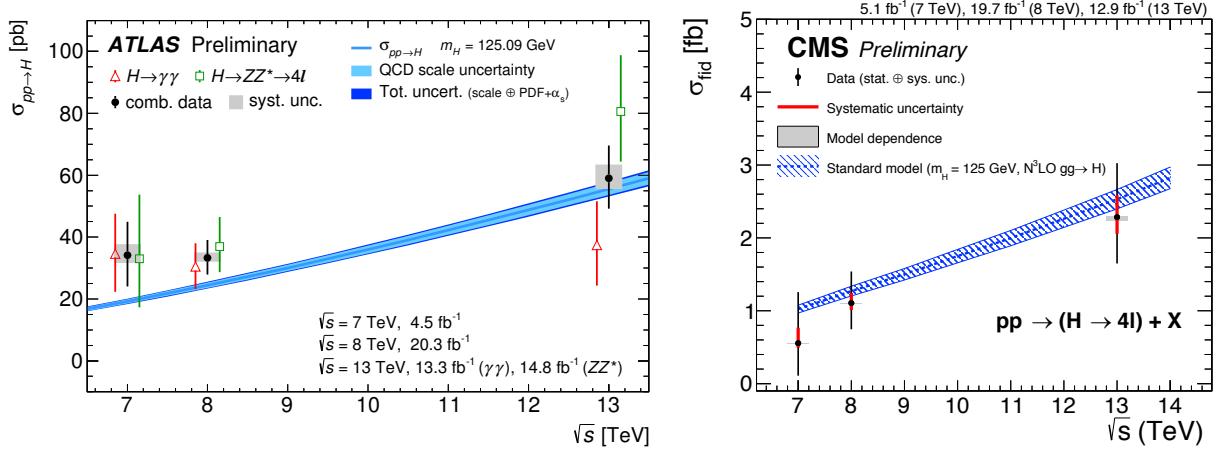


Fig. 34: Total (ATLAS, left) and fiducial (CMS, right) $pp \rightarrow H + X$ cross sections measured at different centre-of-mass energies and compared to SM predictions at up to 3NLO in QCD. The left plot shows the individual results of the 4ℓ and $\gamma\gamma$ channels and their combination [126]. The right plot shows the 4ℓ fiducial measurements. Agreement with the SM predictions is observed within yet large uncertainties.

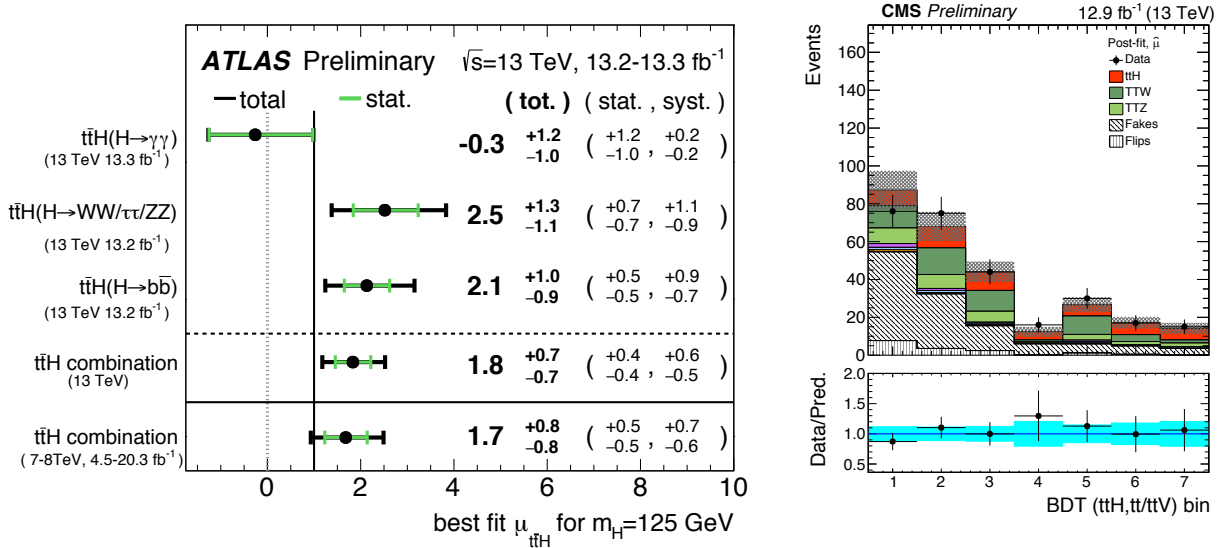


Fig. 35: Left: ATLAS summary of the $\mu_{t\bar{t}H}$ signal strength measurements from the individual analyses and their combination, assuming $m_H = 125$ GeV [135]. Right: boosted decision tree output from CMS in the same-charge channel trained to separate ttW background from ttH signal [131].

background due to $t\bar{t}$ production associated with heavy flavour quarks (c or b) originating mostly from gluon splitting, which is poorly known and needs to be constrained from data simultaneously with the signal. CMS released preliminary 13 TeV results for ttH in all three Higgs decay categories finding for the relative signal strengths [131–133]: $\mu_{t\bar{t}H(\rightarrow\gamma\gamma)} = 3.8^{+4.5}_{-3.6}$, $\mu_{t\bar{t}H(\rightarrow\text{leptons})} = 2.0^{+0.8}_{-0.7}$, and $\mu_{t\bar{t}H(\rightarrow b\bar{b})} = -2.0 \pm 1.8$, with no significant excess observed. ATLAS also measured all three channels [134] and their statistical combination [135] that is shown in the left panel of Fig. 35. The combined preliminary signal strength is $\mu_{t\bar{t}H} = 1.7 \pm 0.8$.

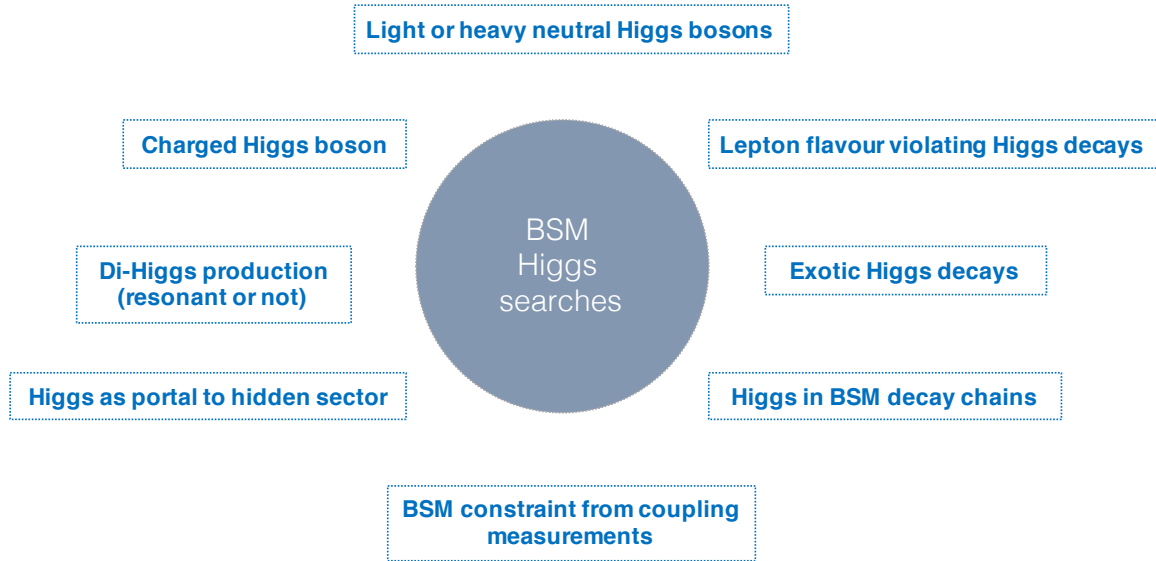


Fig. 37: Illustration of beyond the SM Higgs boson search areas.

8.3 Searches — a fresh start

Many of the high mass and higher cross section searches for new physics already benefited from the 2015 13 TeV data sample to extend their sensitivity, and all searches surpass their Run-1 limits with the 2016 datasets (see Fig. 36). Run-2 represents thus a fresh start in the quest for new physics after the negative searches from Run-1. The legacy of Run-1 also contained a small number of anomalies that needed to be verified in the Run-2 data. Only 13 TeV searches are discussed in the following.



Fig. 36: The bulldozer (aka, LHC at 13 TeV) moving out of the way the Run-1 limits on beyond the SM searches.

8.3.1 Additional Higgs bosons

The 125 GeV Higgs boson completes the four degrees of freedom of the SM BEH doublet. Nature may have, however, chosen a more complex scalar sector of, eg., two BEH doublets, which extends the sector by four additional Higgs bosons, of which two are neutral (one CP -even and one CP -odd) and the other two are charged. Searching for ancillary scalar bosons is thus one way to detect BSM physics in the scalar sector. Other ways are to look for non-SM decays of the Higgs boson such as decays to invisible particles where the Higgs boson acts as a portal to new physics responsible for dark matter. The Higgs boson could also be produced as a particle in the decay chain of new physics processes such as supersymmetry. New heavy resonances might decay to a pair of Higgs boson. A summary of BSM options around the Higgs boson is sketched in Fig. 37.

ATLAS and CMS have searched for additional Higgs bosons in Run-1 and Run-2. For $H^\pm \rightarrow \tau\nu$ [136, 137] ($H/A \rightarrow \tau\tau$ [138, 139]), the sensitivity of the new data exceeds that of Run-1 for masses larger than 250 GeV (700 GeV). The search for $A \rightarrow Z(\rightarrow \ell\ell, \nu\nu)h_{125}(\rightarrow bb)$ features improved sensitivity beyond about 800 GeV [140]. Searches for $H \rightarrow ZZ(\rightarrow \ell\ell qq, \nu\nu qq, 4\ell)$ and $WW(\rightarrow \ell\nu qq)$

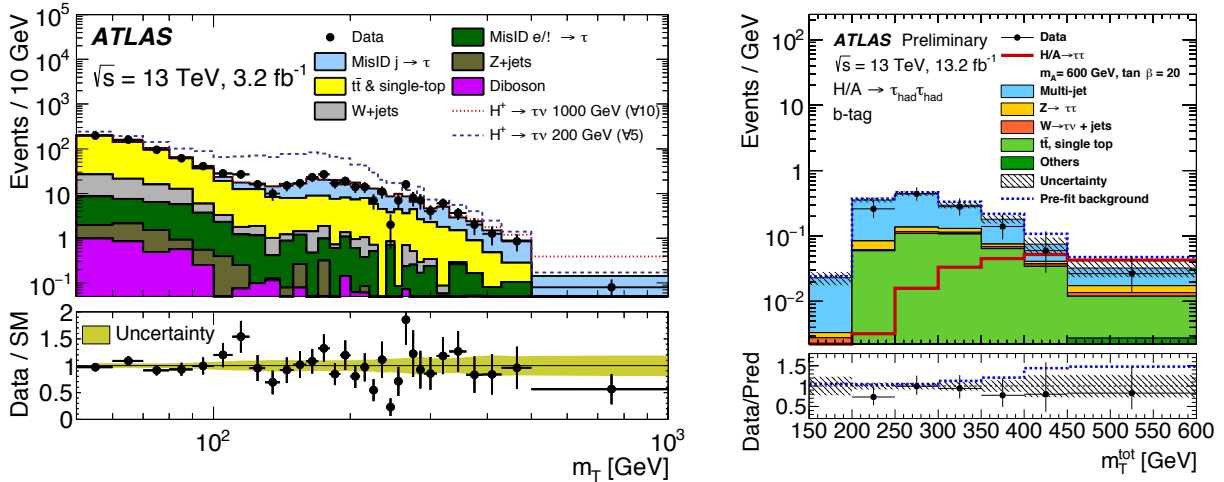


Fig. 38: Left: transverse mass in a search for a charged Higgs boson decaying to $\tau\nu$ [136,137]. Right: distribution of the reconstructed transverse mass in a search for a heavy neutral Higgs boson decaying to a tau τ pair, where both τ leptons are reconstructed via their hadronic decay modes [138].

target the > 1 TeV mass range where the bosons are boosted and their hadronic decays are reconstructed with jet substructure techniques. The search for a resonance decaying to $hh_{125}(\rightarrow bb\gamma\gamma)$ had a small excess in Run-1 at about 300 GeV [141], which has been excluded at 13 TeV [142, 143]. Also performed were searches for resonant and non-resonant $H_{125}H_{125} \rightarrow bb\tau\tau, bbVV_{V=Z/W}, bbbb$ production [144–147]. None of these many searches exhibits an anomaly so far in the 13 TeV data.

A slight Run-1 excess of 2.4σ seen by CMS in the search for the lepton-flavour violating decay $H \rightarrow \tau\mu$ [148] was not seen by ATLAS in Run-1 [149], and also not confirmed by CMS in an early Run-2 analysis [150].

8.3.2 New physics searches in events with jets

Among the first searches performed at any increase of collision energy are those for heavy strongly interacting new phenomena such as excited quarks due to quark substructure, or strong gravity effects. The signatures investigated are a dijet resonance and angular distributions, a resonance decaying to heavy-flavour quarks $X \rightarrow b\bar{b}$ or $t\bar{t}$ [156, 157], high- p_T multijet events, high- p_T lepton plus jets events, and a lepton-jet resonance as could occur in presence of heavy leptoquarks. None of these searches exhibited an anomaly.

Figure 39 shows dijet invariant mass spectra as measured by ATLAS [151, 152] (see [153] for the corresponding CMS analysis). The left panel shows the high-mass tail as obtained with standard unrescaled jet triggers. The right panel shows lower mass events obtained with the use of a hard ISR jet trigger (see Feynman graph in right panel). The measured spectra are compared to phenomenological fits using smoothly falling functions as expected from the QCD continuum. No significant deviation from these fits is seen in the data. In addition to the ISR “trick”, it is possible to reach the low mass dijet regime with high statistics by using high-rate trigger-level objects of events that are prescaled for offline analysis (this technique is denoted Data Scouting in CMS) [154, 155]. Figure 40 shows the combined exclusion plot obtained by ATLAS in the coupling-vs-mass plane for a hypothetical leptophobic Z' resonance. The low-mass region is covered by ISR-based searches both for ISR jets and photons. For intermediate masses the trigger-level analysis (TLA) provides the strongest bounds, and for high Z' masses the standard dijets search takes over, smoothly extending the TLA bound.

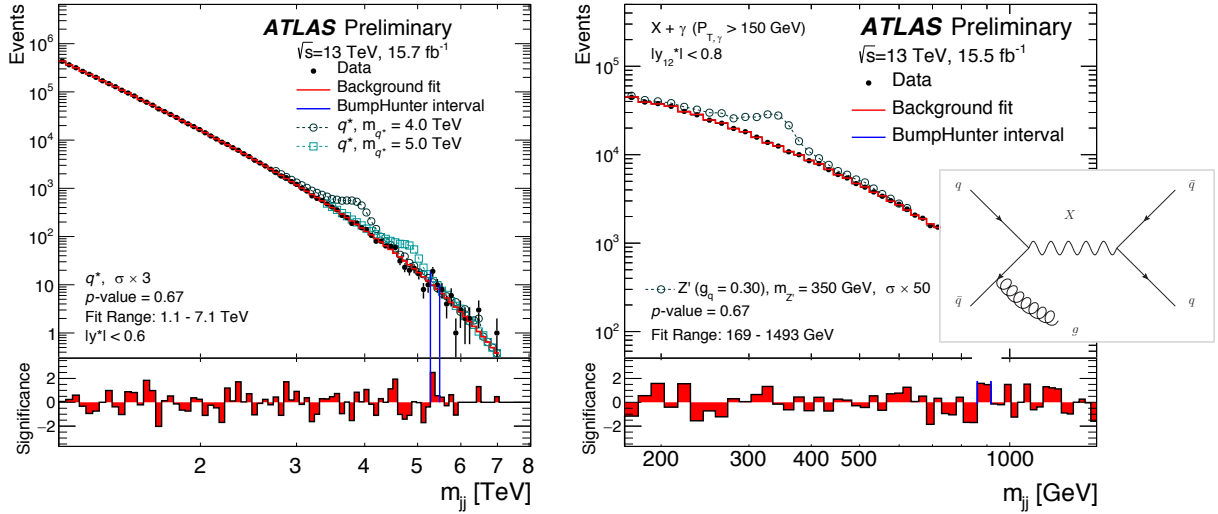


Fig. 39: Dijet invariant mass distributions measured by ATLAS for the high-mass resonance search [151] (left panel) and the low-mass search (right) using events with significant initial-state radiation (cf. Feynman graph in panel) [152].

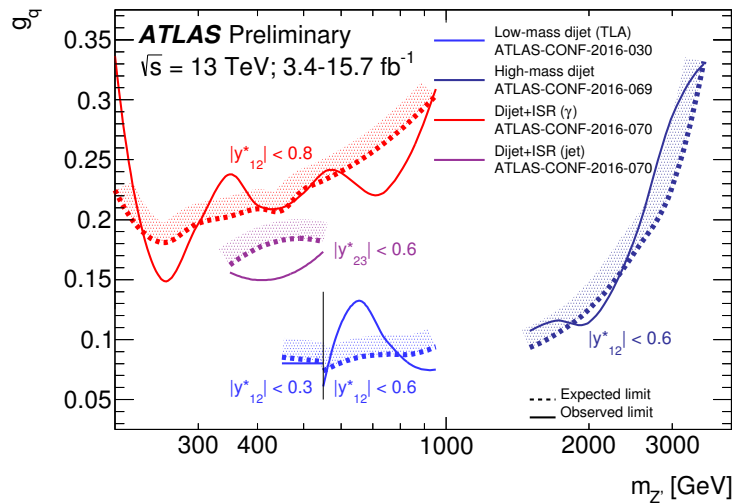


Fig. 40: ATLAS bounds in the coupling-vs-mass plane on a leptophobic Z' model obtained from dijet searches.

8.3.3 Searches in leptonic final states

Canonical searches for new physics are performed in high-mass Drell-Yan production ($Z' \rightarrow \ell\ell$, $W' \rightarrow \ell\nu$) [158–161]. These searches require faithful SM Drell-Yan modelling that is tested using SM differential cross section measurements. High transverse momentum muons represent a challenge for the detector alignment, requiring, eg., down to $30 \mu\text{m}$ relative alignment precision in the ATLAS muon spectrometer. The electron and muon channels have complementary strength: the electron energy resolution measured in the calorimeters being more precise than the muon track momentum resolution, the electron channel has better discovery sensitivity. On the other hand, there is almost no charge information from the electron tracks, so the muon channel is needed to measure the charge of a resonance if detected (cf. the panels in Fig 41). No anomaly was found in the measured spectra. Sequential SM Z' / W' benchmark limits are set at 4.1 / 4.7 TeV (compared to 2.9 / 3.3 TeV at 8 TeV). Figure 42 shows the highest-mass dielectron event measured by CMS in the early 2015 data. It has an invariant mass of 2.9 TeV. For comparison, the highest-mass Run-1 events have 1.8 TeV (ee) and 1.9 TeV ($\mu\mu$).

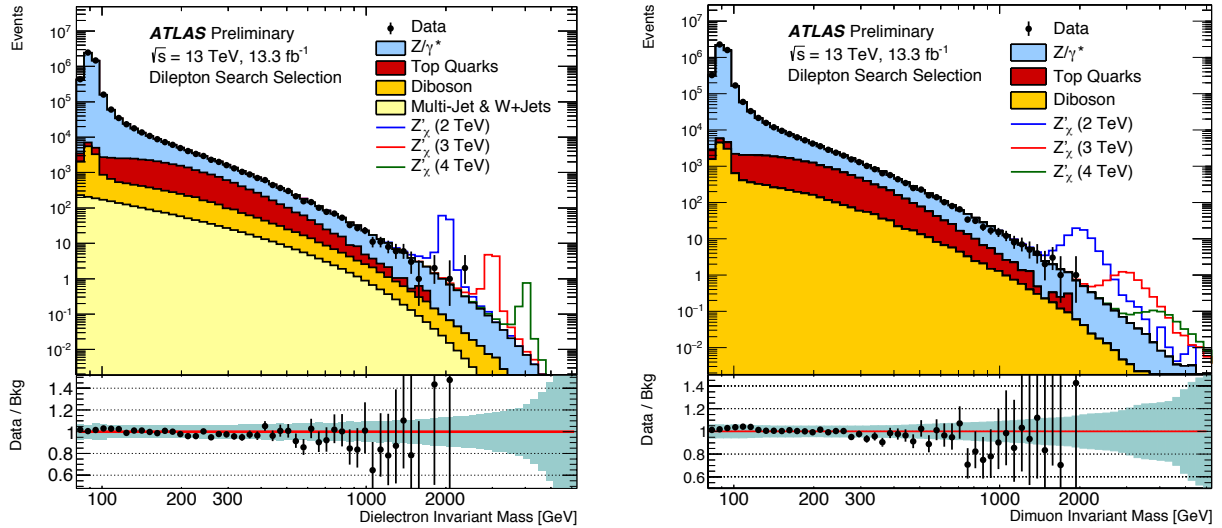


Fig. 41: Dielectron (left panel) and dimuon (right panel) reconstructed invariant mass distributions for data and the SM background estimates as well as their ratios. Benchmark Z' signals with masses of 2, 3 and 4 TeV are overlaid [158].

ATLAS and CMS also looked into high-mass $e\mu$ production not accompanied by neutrinos that would violate lepton flavour conservation. The main background here are top–antitop events that are estimated from MC simulation.

The following table [163] gives a historical evolution of the 95% confidence level lower limits for selected leptonically and hadronically decaying benchmark resonances from Tevatron, via LHC up to the HL-LHC expectation (see [162] for the latter studies). The corollary from these numbers is that future improvement in reach will take more time.

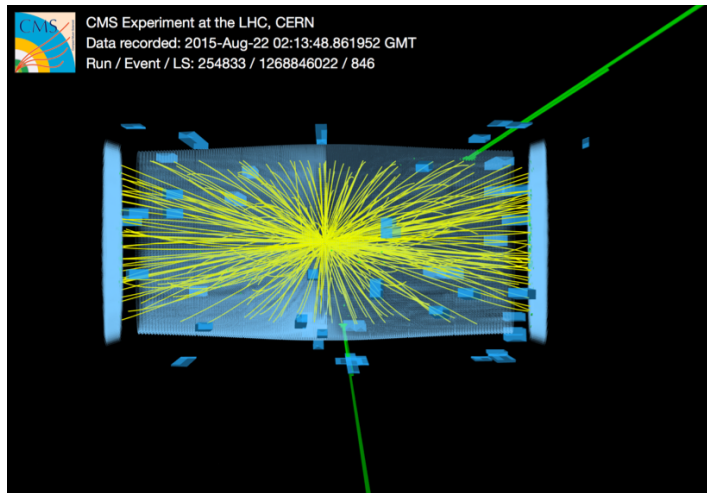


Fig. 42: Display of a rare, colossal e^+e^- event with mass of 2.9 TeV measured by CMS. The electrons are azimuthally back-to-back.

| Model | CDF | 95% confidence level lower limits (TeV) | | | | |
|-------------------------------------|-----|---|-------------|-----------|-----------------------------------|------------------------------------|
| | | Run-1 '12 | Moriond '16 | ICHEP '16 | 300 fb ⁻¹ 14 TeV pp | 3000 fb ⁻¹ 14 TeV pp |
| $Z' \rightarrow \ell\ell$ | 1.1 | 2.9 | 3.4 | 4.1 | 6.5 | 7.8 |
| $q^* \rightarrow qg$ | 0.9 | 4.1 | 5.2 | 5.6 | 7.4 | 8 |
| $Z' \rightarrow tt$ (1.2% width) | 0.9 | 1.8 | 2.0 | – | 3.3 | 5.5 |

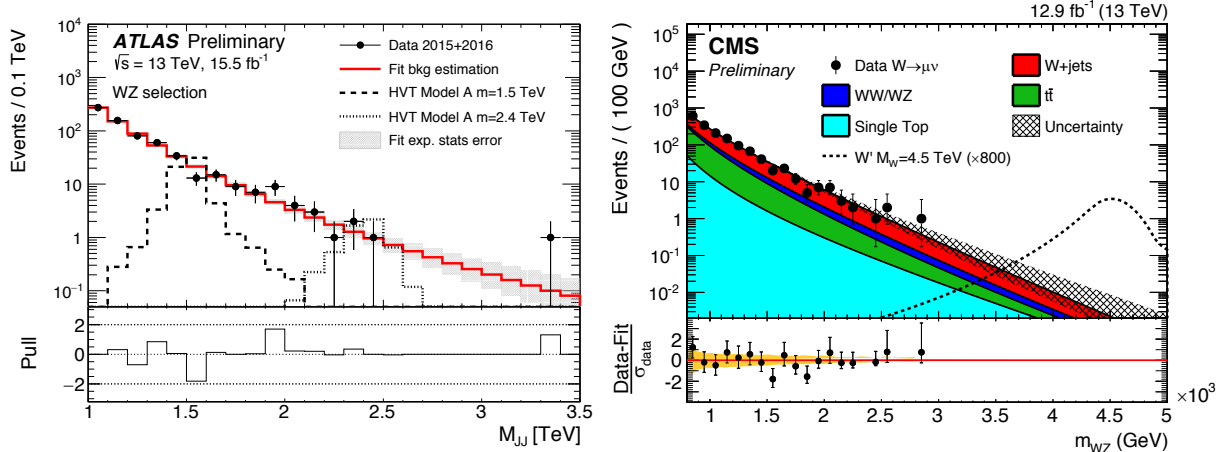


Fig. 43: Diboson mass in the fully hadronic channel (ATLAS [166], left panel) and semileptonic channel (CMS [167], right) for data and background expectations.

8.3.4 Searches for diboson resonances (VV , Vh , hh)

Diboson resonances occur in many new physics scenarios and also in extended scalar sector models. If the resonances are heavy, the high transverse momentum of the decaying bosons boosts the hadronic decay products into merged jets. Jet substructure analysis is used to reconstruct hadronically decaying bosons and to suppress strong interaction continuum backgrounds. Some excess of events with a (global) significance of 2.5σ was seen by ATLAS in Run-1 around a mass of 2 TeV in fully hadronically decaying VV events (mostly WZ) [164,165], which was however not observed in the other weak gauge boson decay channels of similar sensitivity. The excess is not confirmed in Run-2 [166,167] (cf. Fig. 43).

Searches for a new resonance in the diphoton mass spectrum were performed by ATLAS [168,169] and CMS [170] in Run-1 looking for a low to medium mass scalar resonance, or a medium to high mass spin-two resonance motivated by strong gravity models. Diphoton spectra were also analysed in view of high-mass tail anomalies due to new nonresonant phenomena. Searches involving at least three photons were used during Run-1 to look for new physics in Higgs or putative Z' decays [171].

Preliminary analyses of the 13 TeV diphoton data presented at the 2015 end-of-year seminars showed an excess of events at around 750 GeV invariant diphoton mass in ATLAS and, albeit weaker, also in CMS. In spring 2016, reanalyses of the 2015 data were published by ATLAS [172] and CMS [173] confirming the preliminary results. CMS also included 0.6 fb^{-1} of data taken without magnetic field requiring a dedicated reconstruction. The photons are tightly identified and isolated and have a typical purity of 94%. The background modelling uses empirical functions fit to the full invariant mass spectra (ATLAS uses a theoretical model to describe the background shape in the spin-2 case). ATLAS observed the lowest background-only p-value for a resonance at around 750 GeV with a natural width of about 45 GeV (6% with respect to the mass). The local and global significance was found to be 3.9σ and 2.1σ , respectively. The global significance was derived by running background-only pseudo-experiments, modelled according to the fit to data, and by evaluating for each experiment the mass and width that leads to the largest excess, that is, the lowest p-value. One then counts the fraction of experiments with a p-value lower than that in data. This procedure corrects the local p-value for the trials factor (also called “look-elsewhere effect”). Indeed, the local p-value corresponds to a non-normalised probability that does not have a well-defined interpretation. Only the global p-value defines a proper probability and is thus the correct reference value. CMS also found its lowest p-value at around 750 GeV at, however, a narrow width. Combining 8 TeV and 13 TeV data a global (local) significance of 1.6σ (3.4σ) was seen. These

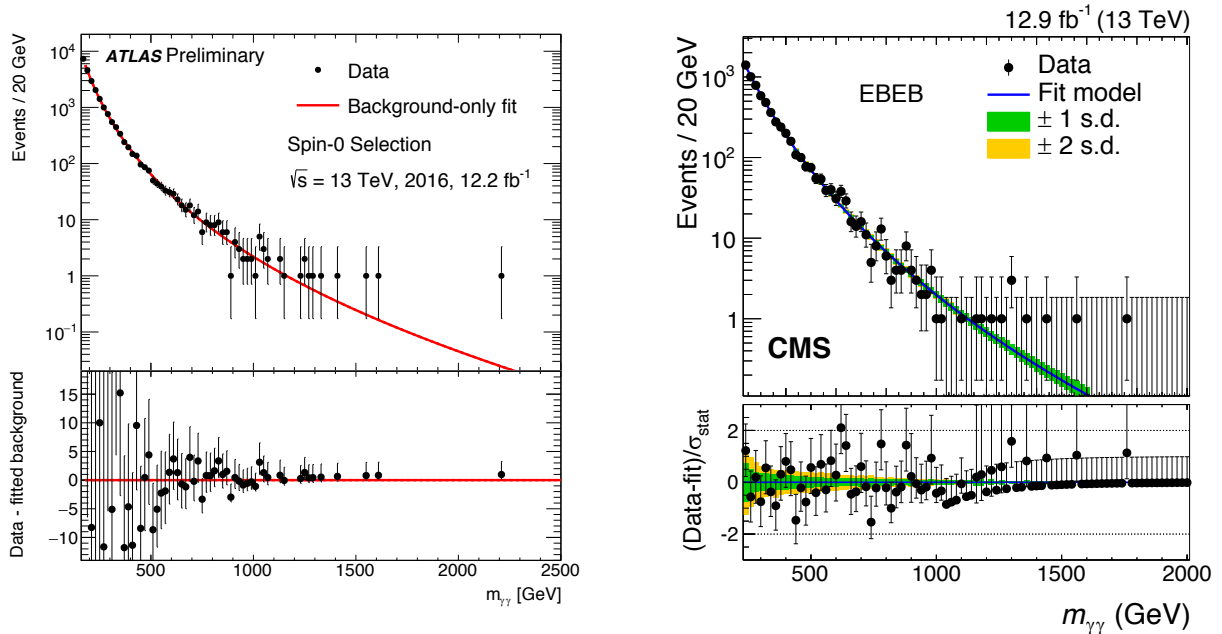


Fig. 44: Diphoton mass spectrum in the summer 2016 dataset from ATLAS (left panel) and CMS (right). There is no noticeable excess at around 750 GeV.

results have prompted intense theoretical activity.

As is well known the first 12–13 fb⁻¹ data taken in 2016 did not reproduce the excess in neither experiment [174, 175] (cf. Fig. 44). The excesses in the 2015 data were thus the result of a statistical fluctuation which, given the global significance, is not that unlikely to occur. One should also take into consideration that the actual trials factor is larger than the global factor quoted for these analyses as there are many signatures probed by the experiments. This truly global significance of a local excess is hard or impossible to estimate in a thorough manner, but the additional trials factor should be kept in mind. In that respect, having a second experiment with a similar non-significant excess does not remove the trials factor if the results from both experiments are retained. Removing the 2015 data and looking solely at 750 GeV in the 2016 data does, however, properly remove any trials factor.

8.3.5 Supersymmetry

Supersymmetry (SUSY) is still among the most popular SM extensions owing to the elegance of the theoretical ansatz, and its phenomenological appeal by offering potential solutions to the hierarchy problem,²⁰ grand unification of the gauge couplings, and dark matter. However, if the SM is included in a supersymmetric theory with SUSY particles (sparticles) that differ by half-a-unit of spin from their SM partners, how is it possible that more than half the particles in the superworld have escaped our observations?

Due to SUSY breaking, allowing the sparticles to acquire large masses,²¹ SUSY comes with very diverse signatures. Highest cross-section events produce gluino or squark pairs with decays to jets and missing

²⁰As the SM, SUSY is a weakly coupled approach to electroweak symmetry breaking in which the Higgs boson remains elementary.

²¹In unbroken SUSY, fermionic $|f\rangle$ and bosonic $|b\rangle$ partner states, transformed into each other via the SUSY generator Q , have the same mass, as $P^2 Q|b\rangle = P^2|f\rangle = m_f^2|f\rangle$, $P^2 Q|b\rangle = Q P^2|b\rangle = Q m_b^2|b\rangle = m_b^2|f\rangle$, and hence $m_f^2 = m_b^2$. P^2 is the square of the energy-momentum operator which commutes with Q .

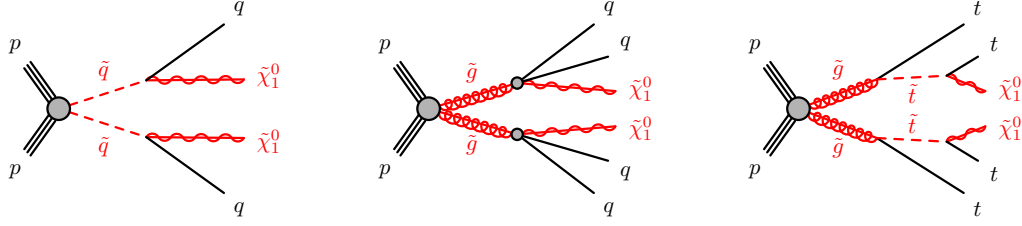


Fig. 45: Graphs for simplified models describing the pair production and decay of supersymmetric particles. Left: squark pair production and decay to two quark-jets and two neutralinos; middle: gluino pair production and decay to four quark-jets and two neutralinos; right: gluino pair production and decay to four top quarks and two neutralinos. The top quarks will each further decay to a W boson and b quark.

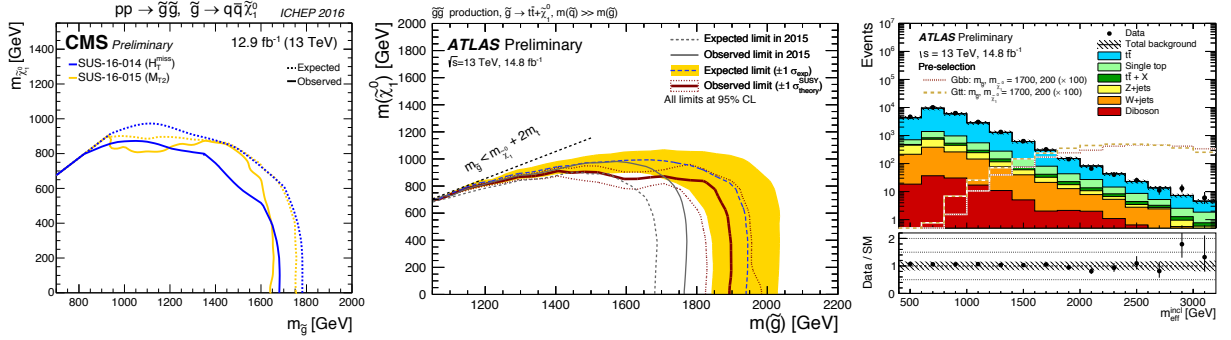


Fig. 46: Left: exclusion limits for strong gluino pair production and decay to four jets and two lightest neutralinos as obtained by CMS [178, 179]. Observed limits are shown with solid lines and expected with dashed lines. Middle: exclusion limits obtained for strong gluino pair production and decay via stop squarks into a four top quark final state and two neutralinos. Right: effective mass distribution obtained in the search for gluino mediated stop production [180] (cf. Footnote 8, page 11 for the definition of the effective mass).

transverse momentum if R -parity is conserved.²² Naturalness suggests not too heavy SUSY top, weak and Higgs boson partners to effectively cancel the radiative corrections to the Higgs mass at high scale and hence provide a solution to the hierarchy problem.²³ It might thus occur that stop pair production, or gluino pair production and decay via stop and top to a four-top final state are the dominant SUSY processes at the LHC. If all strongly interacting SUSY particles are too heavy to be directly produced at the LHC, it could still be that the electroweak partners of the photon, weak bosons and five physical Higgs states are light enough so that SUSY would manifest itself through “electroweak-ino” production featuring final states with leptons (and/or photons) and E_T^{miss} . Finally, SUSY could also give rise to the existence of long-lived heavy particles, and, if R -parity is nonconserved, the lightest SUSY particle could decay to jets or leptons depending on the R -parity violating couplings.

To approach the search for SUSY in a systematic manner, a bottom-up approach through so-called simplified models is used by the experiments. These models correspond to simple signatures as those depicted in Fig. 45. While a simplified model cannot encompass the full SUSY phenomenology, an ensemble of simplified models and the corresponding searches have been shown to cover signatures of complete

²² R -parity, defined by $R = (-1)^{3(B-L)+2S}$, where B , L , S are the baryon, lepton numbers and spin, respectively, is assumed to be conserved in most SUSY models to avoid baryon and/or lepton number violation (and thus proton decay if both occur together). R -parity conservation is arbitrarily imposed and not enforced by any known symmetry. Its consequence is that SUSY particles must be produced in pairs and the lightest SUSY particle is stable.

²³The top quark gives the largest contribution to the radiative corrections of the Higgs mass, δm_H^2 , in presence of a high new physics scale Λ . If the stop is heavier than the top residual logarithmic contributions $\delta m_H^2 \propto \ln(\Lambda^2/m_t^2)$ remain.

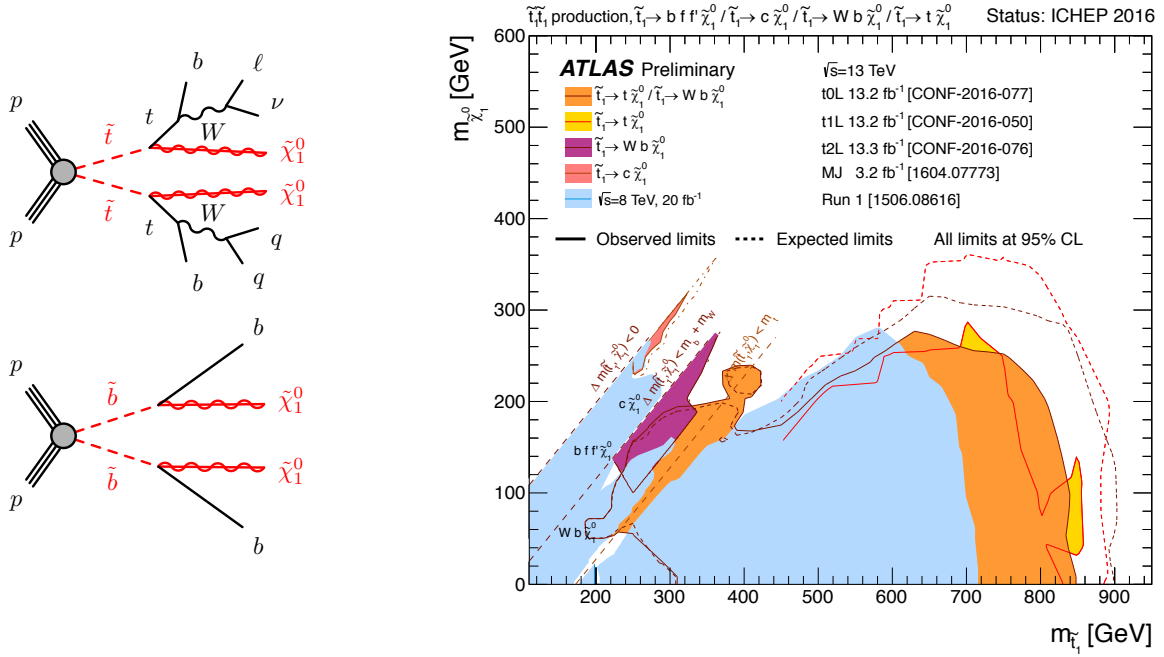


Fig. 47: Graphs for simplified models of stop and sbottom pair production and decay. The right panel shows exclusion limits in the neutralino versus stop mass plane as obtained by ATLAS with several dedicated analyses (see references in figure).

models such as the phenomenological minimal supersymmetric standard model (pMSSM) [176, 177].

Searches for strong SUSY production study events with jets and E_T^{miss} with or without leptons, photons, and b -jets. Up to ten jets are exclusively selected, which requires a data-driven background determination as MC cannot be trusted to reliably predict such large jet multiplicity. None of the searches have revealed a significant anomaly. Figure 46 shows on the left and middle plots exclusion limits in the lightest neutralino mass versus gluino mass planes. The analyses have the sensitivity to exclude gluinos of up to 1.8 TeV for low-mass neutralinos depending on the scenarios. In case of heavy neutralinos, the final states exhibit softer jets and less E_T^{miss} , which leads to reduced trigger efficiency and a more difficult background discrimination thus reducing the sensitivity. The right panel in Fig. 46 shows the effective mass distribution obtained in the search for gluino mediated stop production (four top quark final state). The distribution reaches beyond 3 TeV with the dominant background from top-quark production. No excess of events is seen in data compared to the background estimation.

If gluinos are too heavy to be produced in significant quantities, squark mixing could make third generation squarks lighter than the first and second generation squarks. Direct searches for stop and sbottom squark production have been the topic of intense efforts in both ATLAS and CMS since Run-1. The analyses are distinguished according to the number of identified leptons (0, 1, 2) and differently optimised signal regions target different stop/sbottom and neutralino mass regimes. In the stop case, the signatures also depend on whether the stop decays in a two-body signature to an on-shell top quark and the lightest neutralino, or off-shell via three or four body decays to the top decay products. The right panel in Fig. 47 shows the exclusion limits for simplified models of stop and sbottom pair production and decay obtained by ATLAS with several dedicated analyses. The analyses have sensitivity to exclude stop masses up to 900 GeV. As in the gluino and first-generation squark cases, the limits for heavy neutralinos are significantly worse.

Alternative models for new heavy quark partners introduce, for example, vector-like quarks, which are

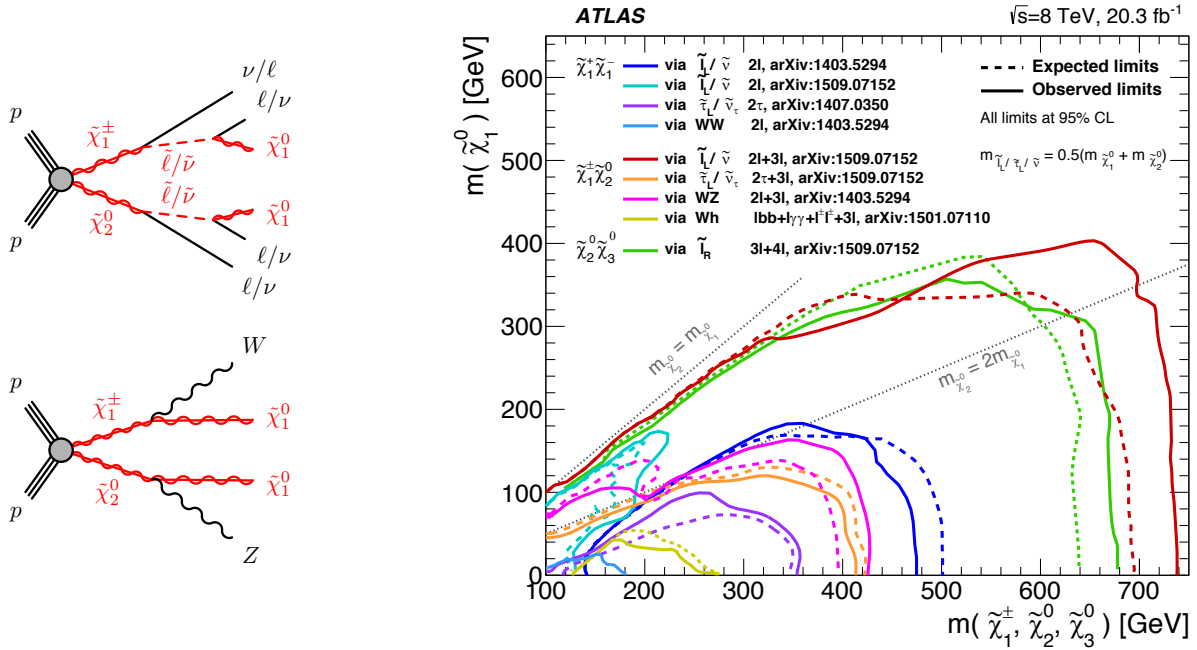


Fig. 48: Graphs for simplified models of associated lightest chargino and next-to-lightest neutralino production and decay through sleptons (top graph) or, if sleptons are too heavy, through W and Z bosons. The right plot shows the exclusion bounds obtained by ATLAS for various electroweakino production scenarios (see references in figure).

hypothetical fermions that transform as triplets under colour and who have left-handed and right-handed components with same colour and electroweak quantum numbers. Vector-like quarks can be singly or pair produced and decay to bW , tZ or tH . Also exotic $X_{5/3} \rightarrow tW$ processes may exist.

It could also be that all squarks and gluinos are beyond reach of the current LHC sensitivity and electroweakinos are the lightest fermions. They have low cross-sections, so that the present Run-2 luminosity just suffices to surpass the Run-1 sensitivity. Figure 48 shows graphs for simplified models of associated lightest chargino and next-to-lightest neutralino production and decay through sleptons (top graph) or, if sleptons are too heavy, through W and Z bosons. The right plot shows the exclusion bounds obtained by ATLAS for various electroweakino production scenarios. Electroweakino decays via sleptons are a favourable case due to the larger leptonic rate than in weak boson decays. In the models considered, chargino pair production has lower cross section than $\tilde{\chi}_1^+ \tilde{\chi}_2^0$ production. The cross section depend on the mixing properties of the states: neutralinos can be bino, wino or higgsino like; charginos wino or higgsino like, depending on the dominant contribution.²⁴

8.3.6 Search for massive long-lived massive particles

Massive long-lived heavy particles are predicted in many new physics models. They can occur due to large virtuality (such as predicted in split supersymmetry), low couplings (such as predicted in some gauge mediated SUSY breaking scenarios where the gravitino is the lightest SUSY particle), and mass

²⁴There are a total of eight spin-half partners of the electroweak gauge and Higgs bosons: the neutral bino (superpartner of the $U(1)$ gauge field), the winos, which are a charged pair and a neutral particle (superpartners of the W bosons of the $SU(2)_L$ gauge fields), and the higgsinos, which are two neutral particles and a charged pair (superpartners of the Higgs field's degrees of freedom). The bino, winos and higgsinos mix to form four charged states called charginos ($\tilde{\chi}_i^\pm$) and four neutral states denoted neutralinos ($\tilde{\chi}_i^0$). Their indices i are ordered according to the increasing mass of the $\tilde{\chi}_i$ state.

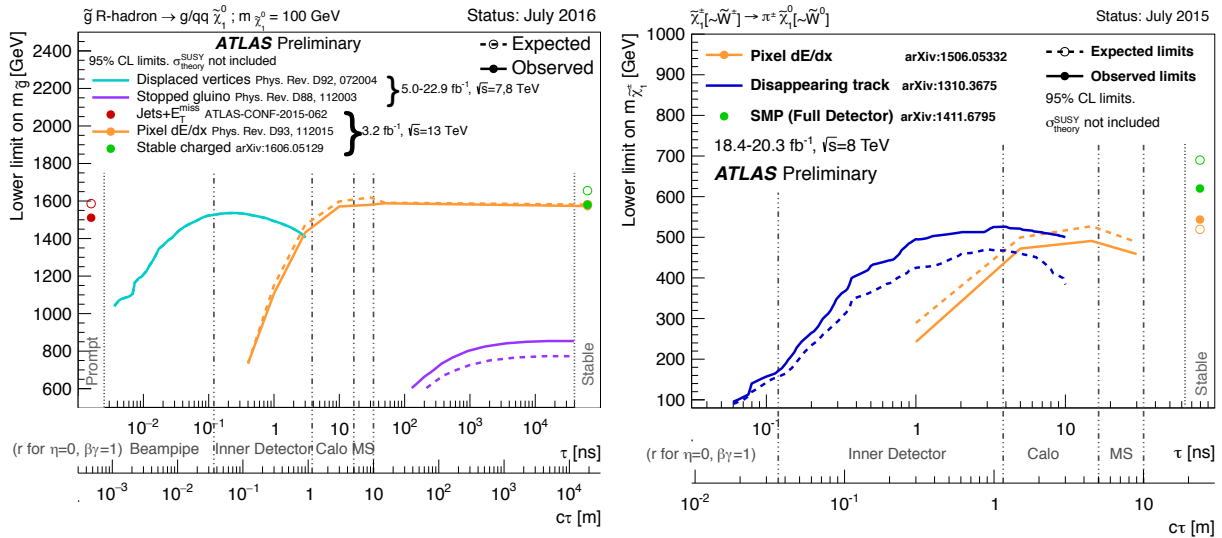


Fig. 49: Exclusion limits on the gluino mass versus lifetime (left panel) and chargino mass versus lifetime (right) as obtained by ATLAS (see references in figure). The dots on the left (right) of the plots indicate the limits obtained on promptly decaying (stable) gluinos/charginos. Varying searches cover the full lifetime spectrum.

degeneracy in a cascade decay, eg., via a scale-suppressed colour triplet scalar from unnaturalness [181] or anomaly-mediated SUSY breaking scenarios with a wino-like lightest chargino [182]. The search for massive long-lived particles is a key part of the LHC search programme.

The LHC experiments search for massive long-lived particles using measurements of specific ionisation loss in the tracking detectors, the time-of-flight in the calorimeters and muon systems, and by reconstructing displaced vertices, kinked or disappearing tracks. Looking for calorimeter deposits outside of the colliding proton bunches makes it possible to look for very long-lived strongly interacting massive particles that were stopped in the calorimeter layers [183,184]. Some signatures need dedicated triggers, most require novel analysis strategies to determine backgrounds from data. Figure 49 shows exclusion limits on the gluino mass versus lifetime (left panel) and chargino mass versus lifetime (right) as obtained by ATLAS. The dots on the left (right) of the plots indicate the limits obtained on promptly decaying (stable) gluinos/charginos. Varying searches cover the full lifetime spectrum. It is interesting to observe that the standard SUSY searches are not blind to scenarios with long-lived sparticles if their lifetime is short enough to still decay before the calorimeter.

8.3.7 Searches for dark matter production

If dark matter particles (assumed to be weakly interacting and massive, WIMPs) interact with quarks and/or gluons they can be directly pair produced in the proton collisions at the LHC [185]. Since the WIMPs remain undetected, to trigger the events a large boost via initial state jet or photon radiation (or other recoiling particles) is needed leading to large missing transverse momentum from the recoiling WIMP pair. The final state signature depends on the unknown details of the proton–WIMP coupling. A set of “ $X + E_T^{\text{miss}}$ ” searches is therefore needed for full experimental coverage. The most prominent and among the most sensitive of these is the so-called “mono-jet” search, which extends to a couple of high- p_T jets recoiling against the E_T^{miss} (cf. Fig. 50). Large irreducible SM backgrounds in this channel stem from $Z(\rightarrow \nu\nu) + \text{jets}$ and $W(\rightarrow \ell\nu) + \text{jets}$ events, where in the latter case the charged lepton is either undetected or a hadronically decaying tau lepton. These backgrounds are determined in data control regions requiring accurate input from theory to transfer the measured normalisation scale factors to the

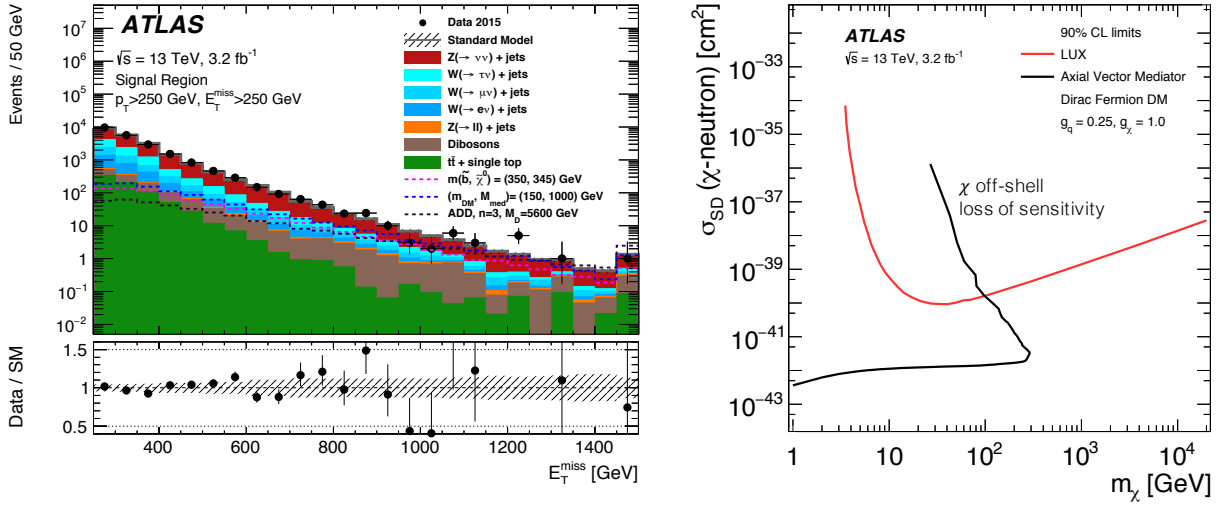


Fig. 51: Left: distribution of missing transverse momentum measured by ATLAS at 13 TeV in a “mono-jet” search [186]. The dominant backgrounds stem from leptonic Z and W plus jets events. Also shown are distributions for new physics benchmark models. Right: exclusion limit on the spin-dependent WIMP–neutron scattering cross section versus the WIMP mass in the context of a Z' -like simplified model with axial-vector couplings. The result is compared with limits from the LUX experiment [195]. All limits are shown at 90% confidence level, which is the standard benchmark in direct dark matter detection experiments. The comparison to LUX is valid solely in the context of this model, assuming minimal mediator width and the coupling values $g_q = 1/4$ and $g_\chi = 1$ [186].

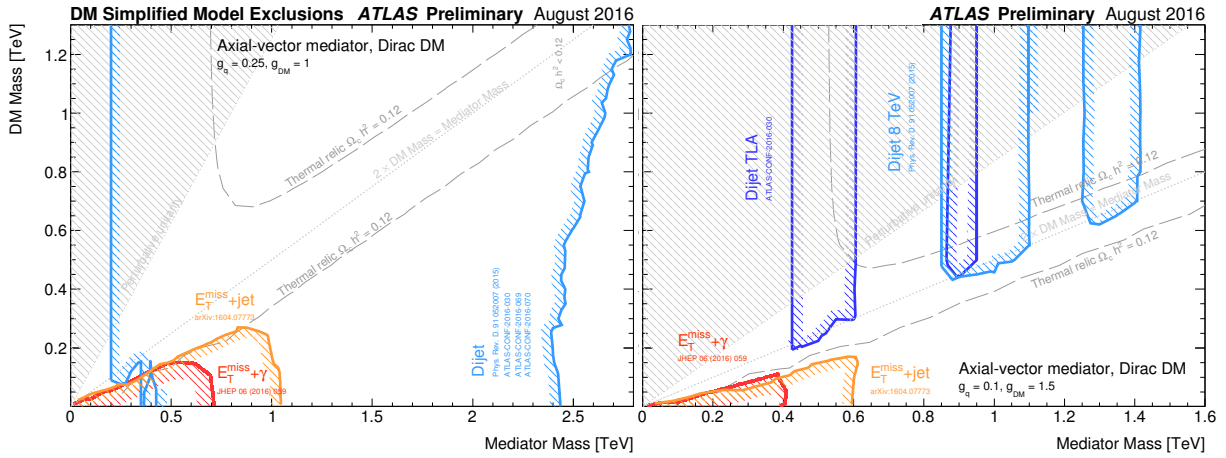


Fig. 52: Regions in a dark matter (DM) versus mediator mass planes excluded at 95% CL by a selection of ATLAS DM searches, for a possible interaction between the SM and DM, the lepto-phobic axial-vector mediator described in [185]. The left panel shows exclusion bounds for quark coupling $g_q = 1/4$, universal to all flavors, and dark matter coupling $g_{DM} = 1$. On the right panel $g_q = 1/10$ and $g_{DM} = 3/2$ are assumed. Shown are the results from the monojet, monophoton and dijet resonance searches. Dashed curves labelled “thermal relic” indicate combinations of DM and mediator mass that are consistent with the cosmological DM density and a standard thermal history. Between the two curves, annihilation processes described by the simplified model deplete the relic density. A dotted curve indicates the kinematic threshold where the mediator can decay on-shell into DM. Points in the plane where the model is in tension with perturbative unitarity considerations are indicated by the shaded triangle at the upper left. The exclusion regions, relic density contours, and unitarity curve are not applicable to other choices of coupling values or model. See [196] for more information.

signal regions.

Numerous 13 TeV results have been released by ATLAS and CMS, including jets + E_T^{miss} [186, 187], photon + E_T^{miss} [188, 189], Z/W + E_T^{miss} [190, 191], and bb/tt + E_T^{miss} [192–194] signatures. None of these has so far shown an anomaly. Figure 51 shows the missing transverse momentum distributions measured by ATLAS in the monojet jets + E_T^{miss} search.

Since the mediator is produced via quark annihilation (g_q) it can also decay to quarks and hence the dijet resonance search is sensitive to it. Figure 52 shows for a specific benchmark model and two different coupling sets (see figure caption) ATLAS exclusion regions in the DM versus the model’s mediator mass plane as obtained from the jets + E_T^{miss} and photon + E_T^{miss} analyses as well as from the dijet resonance search. These searches have complementary sensitivity.

Finally, we note that even in the case of a signal in one of the LHC WIMP searches the LHC may not be able to prove that a signal is indeed dark matter because of insufficient constraints on the lifetime of the detected WIMPs.

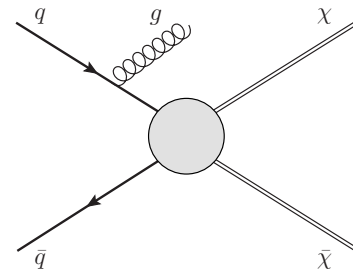


Fig. 50: Graph for WIMP pair production with initial-state radiation jet.

9 The road to the future

The LHC experimental programme follows a well-defined suit of data taking periods followed by longer technical stops used to repair and upgrade the accelerator and experiments. With the approval of the HL-LHC project by the CERN Council in 2016 a roadmap for twenty more exciting years of physics with the LHC has been established. That roadmap is sketched in Fig. 53. The current Run-2 will continue until end of 2018 with a delivered integrated luminosity at 13 TeV (or higher) that may reach 120 fb^{-1} . The following two year long shutdown (LS2) will be used to upgrade the injector for an increased beam brightness (batch compression in the PS, new optics in the SPS, collimator upgrades). Also the experiments upgrade their detectors to prepare for the increased Run-3 luminosity. The following data taking period between 2021 and 2023 should allow the LHC to deliver a total of 300 fb^{-1} at 13–14 TeV proton–proton centre-of-mass energy. This is followed by the major HL-LHC

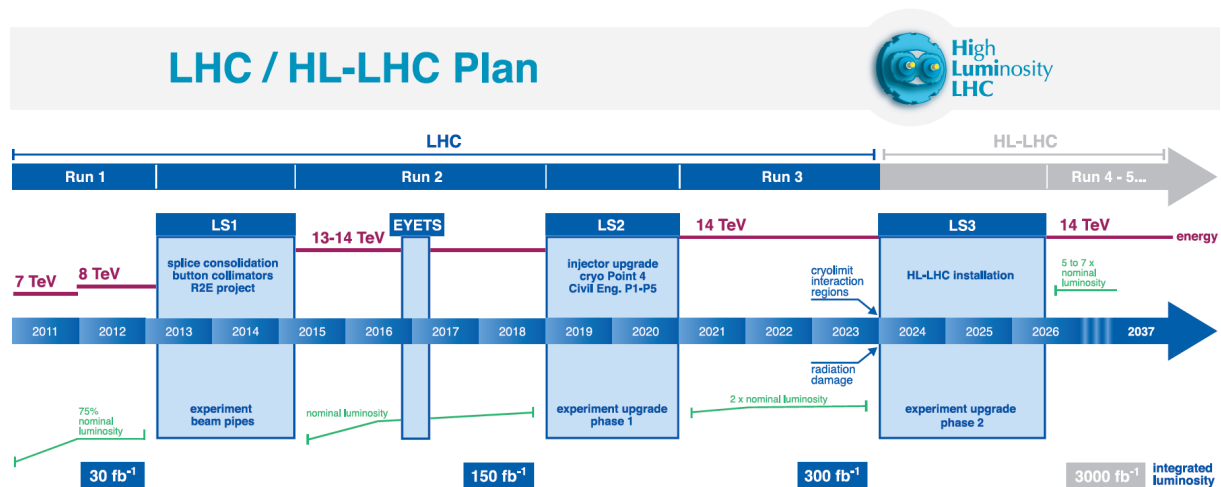


Fig. 53: Timeline of the LHC programme up to the high-luminosity LHC (HL-LHC).

upgrade during 2024 until 2026, featuring a new LHC triplet design (low- β^* quadrupoles, crab cavities), and injector upgrades for luminosity levelling [197]. Here, also the experiments will undergo major upgrades to prepare for the high-luminosity phase [198, 199]. Collisions are expected to resume in 2026 allowing to deliver to each experiment (ATLAS and CMS) 300 fb^{-1} per year. The following table summarises some of the LHC beam parameters during Run-1, Run-2, and as expected for Run-3 and the HL-LHC.²⁵

| Parameter | LHC Run-1 | LHC Run-2 & 3 | HL-LHC |
|---|---------------------|---------------------------------|------------------------------|
| Beam energy [TeV] | 0.45–4 | 6.5–7 | 7 |
| Peak inst. luminosity [$\text{cm}^{-2} \text{ s}^{-1}$] | $0.8 \cdot 10^{34}$ | $(0.7\text{--}2) \cdot 10^{34}$ | $5 \cdot 10^{34}$ (levelled) |
| Bunch distance [ns] | 50 | 25 | 25 |
| Max. number of bunches | 1380 | 2028~2748 | 2748 |
| β^* [cm] | 60 | 40 | 15 |
| ϵ_n [μm] | 2.3 | 2.5–3.5 (2.3 with BCMS) | 2.5 |
| Max. num. protons per bunch | $1.7 \cdot 10^{11}$ | $1.2 \cdot 10^{11}$ | $2.2 \cdot 10^{11}$ |
| Average pileup $\langle\mu\rangle$ | 21 | 21~50 | 140 |

If one wants to succinctly highlight the main physics results of the LHC proton–proton programme during Run-1, one should emphasise the discovery of the Higgs boson, searches for additional new physics (all negative), multiple SM measurements, the observation of rare processes such as $B_s \rightarrow \mu\mu$, precision measurements of SM processes and parameters, and the study of CP asymmetries in the B_s sector. For Run-2 and Run-3, the focus lies on searches for new physics at the energy frontier, improved measurements of Higgs couplings in the main Higgs boson channels, consolidation and observation of the remaining Higgs decay and production modes, measurements of rare SM processes and more precision, improved measurements of rare B decays and CP asymmetries. Finally, the HL-LHC will serve for precision measurements of Higgs couplings, the search for and observation of very rare Higgs modes (among these di-Higgs production), the ultimate new physics search reach (on mass and forbidden decays such as FCNC), and ultimate SM and heavy flavour physics precision for rare processes (VBS, aT/QGC, etc.). Although any new physics found along the way would likely be a game changer in this planning process, these physics goals are “must do” topics for the HL-LHC.

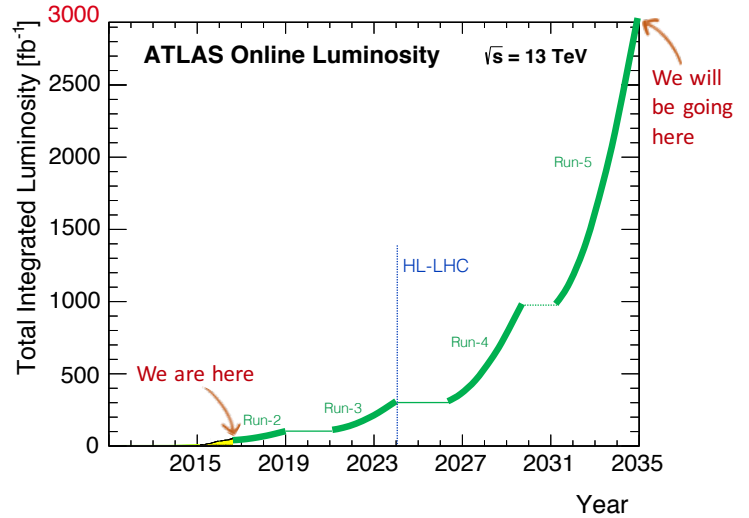


Fig. 54: Sketch illustrating the integrated luminosity evolution during the various LHC phases [200]. LHC physics will hardly look the same again.

The substantial increase in luminosity will pose major technical challenges for the experiments. The average pileup will rise to $\langle\mu\rangle = 140$ inelastic collisions per bunch crossing at (levelled) $5 \cdot 10^{34} \text{ cm}^{-2} \text{ s}^{-1}$,

²⁵Recall that $L \propto (\sigma_x \sigma_y)^{-1} = (\epsilon_n \beta^* / \gamma)^{-1}$

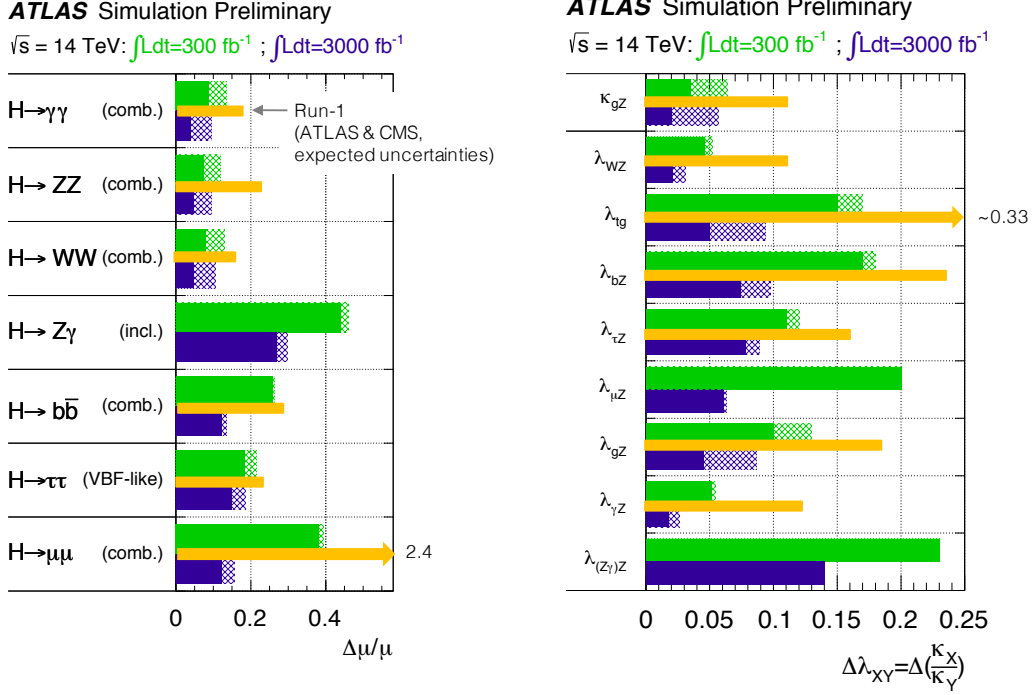


Fig. 55: Current (orange) and prospects for future precision (green for Run-3, blue for HL-LHC) on the measurements of the Higgs signal strengths (left panel) and the coupling modifier ratios (right). Hatched areas indicate the impact of theoretical uncertainties on expected cross-sections [201]. (The original figures have been modified.)

which will increase the background levels, the average event size and the time it takes to reconstruct the events (dominated by the track reconstruction). Faster detectors and readout electronics, as well as more sophisticated trigger systems will be required to efficiently identify physics signatures while keeping the transverse momentum thresholds at the current level. Finally, the detectors will need to withstand substantial radiation dose. Ambitious and costly upgrade programmes of the experiments address these challenges by improving the trigger and data acquisition systems, the front-end electronics, entirely replacing the inner tracking system (thereby increasing the tracker acceptance), and, in case of CMS, the endcap calorimeter, and more.

Among the large amount of prospective studies for the physics potential of the HL-LHC (and compared to the Run-3 integrated luminosity of 300 fb^{-1}) I would like to mention here the prospects for Higgs coupling measurements, the constraint on the Higgs width from Higgs off-shell coupling measurements, and a precision measurement of $B_s \rightarrow \mu\mu$.

From a rather conservative extrapolation of the Run-1 Higgs coupling measurements ATLAS has derived the prospects shown in Fig. 55 assuming SM central values for the couplings. As a reminder, the coupling modifiers are defined by $\kappa_i^2 = \sigma_i/\sigma_i^{\text{SM}}$ and $\lambda_{ij} = \kappa_i/\kappa_j$. The best precision of a few percent on the relative Higgs signal strengths is obtained for the diphoton, four-lepton and $2\ell 2\nu$ decay channels. The decays to $\tau\tau$ and bb are challenging and will be limited by systematic uncertainties. The rare decays to $Z\gamma$ and $\mu\mu$ will have been observed and be statistically limited. The coupling modifier ratios (cf. right panel of Fig. 55) show a similar pattern. The important Higgs–top to Higgs–gluon coupling ratios are expected to be measured with a precision reaching 5% at the HL-LHC. Theory uncertainties are limiting the achievable precision in several cases. Some of the uncertainties cancel in the coupling modifier ratios.

Both CMS and ATLAS have constrained the Higgs off-shell coupling in Run-1 analyses and through

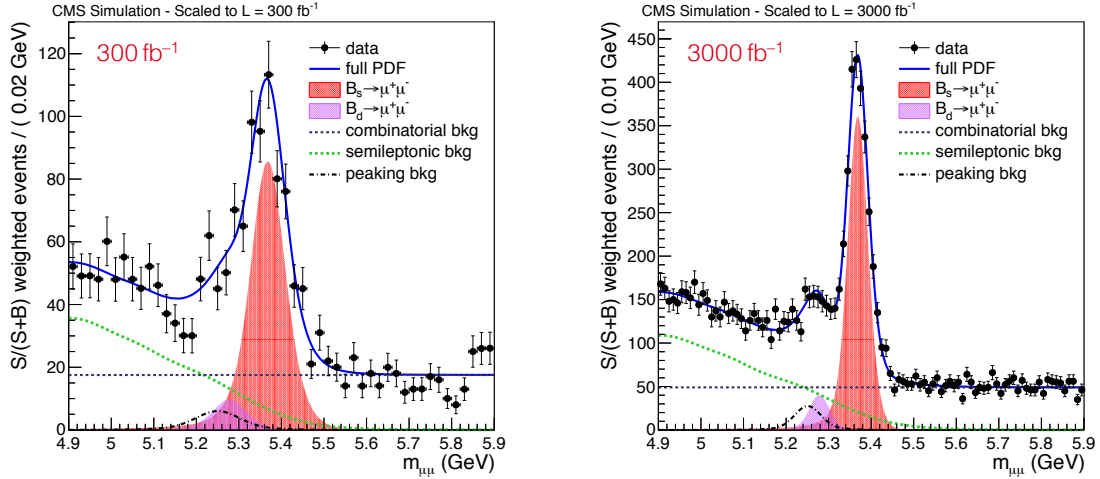


Fig. 56: Expected invariant mass distribution in the measurement of $B_{(s)} \rightarrow \mu\mu$ for 300 fb^{-1} and 3000 fb^{-1} from a prospective study by CMS [206].

this obtained upper limits on the Higgs total width Γ_H [202, 203]. The method uses the independence of the off-shell cross section on Γ_H and relies on the assumption of identical on-shell and off-shell Higgs couplings.²⁶ One can then determine Γ_H ($=4.1 \text{ MeV}$ in SM [204]) from the measurements of the off-shell and on-shell signal strengths $\mu_{\text{off-shell}}$ and $\mu_{\text{on-shell}}$ as follows:

$$\mu_{\text{off-shell}}(\hat{s}) = \frac{\sigma_{\text{off-shell}}^{gg \rightarrow H^* \rightarrow VV}(\hat{s})}{\sigma_{\text{off-shell,SM}}^{gg \rightarrow H^* \rightarrow VV}(\hat{s})} = \kappa_{g,\text{off-shell}}^2(\hat{s}) \cdot \kappa_{V,\text{off-shell}}^2(\hat{s}),$$

$$\mu_{\text{on-shell}} = \frac{\sigma_{\text{on-shell}}^{gg \rightarrow H \rightarrow VV^*}}{\sigma_{\text{on-shell,SM}}^{gg \rightarrow H \rightarrow VV^*}} = \frac{\kappa_{g,\text{off-shell}}^2(\hat{s}) \cdot \kappa_{V,\text{off-shell}}^2(\hat{s})}{\Gamma_H / \Gamma_{H,\text{SM}}}.$$

With the Run-1 datasets, limits of the order of 5 times $\Gamma_{H,\text{SM}}$ were obtained by ATLAS and CMS. An ATLAS HL-LHC study [205] derived prospects for integrated luminosities of 300 fb^{-1} and 3000 fb^{-1} giving $\mu_{\text{off-shell}} = 1^{+0.80}_{-0.97}$ and $1^{+0.43}_{-0.50}$, respectively. The latter precision allows to constrain Γ_H to remarkable $4.1^{+1.5}_{-2.1} \text{ MeV}$.

In the area of new physics searches, the emphasis will gradually move towards rare and difficult channels, such as low cross-section electroweak production and compressed scenarios in SUSY. Searches for WIMPs will require improvements in the data-driven determination of the backgrounds to take full benefit from the increased data sample.

Among the many other interesting prospects, one should also note the continuous gain in precision and reach for rare or suppressed processes in the flavour sector. The rise in luminosity during Run-2 will be slower for LHCb due to the luminosity levelling. The upgrade to 40 MHz trigger readout during the long shutdown 2 in 2019 will help increase the annual muonic B rate by a factor of ten. High-profile rare decay measurements performed by LHCb, ATLAS and CMS are $B_{(s)} \rightarrow \mu\mu$ (and similar) as well as $b \rightarrow s$ transitions such as $B \rightarrow K^* \mu\mu$ and similar modes. Figure 56 shows the invariant mass distribution for $B_{(s)} \rightarrow \mu\mu$ as expected from a prospective study by CMS [206]. The observation beyond 5σ significance of the loop and CKM suppressed decay $B \rightarrow \mu\mu$ is expected for the full HL-LHC integrated luminosity. CP-violation measurements of the phase ϕ_s will be performed by LHCb (dominant) and also by ATLAS

²⁶The denominator of a relativistic Breit-Wigner resonance lineshape has the form $(s - m^2)^2 + s^2 \Gamma^2 / m^2$. For $s \sim m^2$ (on-shell) the first term in the denominator vanishes so that the coupling depends reciprocally on the width Γ . In the off-shell regime $s \gg m^2$ the first term dominates and the Γ dependence becomes negligible.

and CMS, the unitarity triangle angle γ and other CKM parameters will be measured by LHCb. These important measurements will benefit from any increase in integrated luminosity. LHCb will also improve CP asymmetry measurements in the charm sector. Of high importance given the current results is to pursue measurements testing lepton universality in B decays (LHCb and Belle). Finally, further surprises and a better understanding of recently discovered heavy flavour spectroscopy states are expected by LHC, ATLAS and CMS.

10 Conclusions

The LHC Run-2 is a key period for particle physics. The first 100 fb^{-1} at 13 TeV centre-of-mass energy are critical for new physics searches in all signatures. Further consolidation of the Higgs sector with the observation and measurement of $H \rightarrow \tau\tau$, $H \rightarrow bb$, and associated ttH production, as well as more precise coupling, fiducial and differential cross section measurements will be followed up with high priority by ATLAS and CMS. The luminosity of Run-2 will hugely increase the amount of interesting Standard Model and flavour physics measurements that can be performed.

Throughout Run-2 it is important to stay alert. New physics does not necessarily appear at high mass so that one needs to continue to search everywhere. High precision measurements are key for a better knowledge of the Standard Model. It is thereby extremely important to measure the detector performance in data as precisely as possible, and this may have priority over further improving the performance. Many results are dominated by theoretical uncertainties. The experiments need to produce measurements that allow to test theory, to improve PDFs, and that motivate theorists to improve calculations and event generators. We may cite William Thomson Kelvin, from a speech held to the British Association for the Advancement of Science in 2 Aug 1871: “Accurate and minute measurement seems to the non-scientific imagination, a less lofty and dignified work than looking for something new. But [many of] the grandest discoveries of science have been but the rewards of accurate measurement and patient long-continued labour in the minute sifting of numerical results.”

I thank the organisers of the 2016 European School of High-Energy Physics for giving me the opportunity to lecture at this excellent school at a very pleasant location in Norway.

Contents

| | | |
|-------|--|----|
| 1 | Introduction | 1 |
| 2 | Particle physics at the dawn of the LHC | 3 |
| 3 | Experimental setup | 4 |
| 4 | Experimental methods | 6 |
| 4.1 | Luminosity | 6 |
| 4.2 | Proton–proton collisions | 8 |
| 4.3 | The experimental data path in a nutshell | 9 |
| 4.4 | Monte Carlo event simulation | 10 |
| 4.5 | Cross section measurement and data unfolding | 10 |
| 4.6 | Background determination | 11 |
| 4.7 | Basic physics objects | 12 |
| 4.8 | Boosted objects | 13 |
| 4.9 | Systematic uncertainties | 14 |
| 5 | Physics highlights from the LHC Run-1 | 14 |
| 5.1 | Standard Model and top-quark physics | 14 |
| 5.2 | Higgs boson physics | 17 |
| 5.3 | Heavy flavour physics | 20 |
| 6 | Digression on electroweak precision measurements | 22 |
| 6.1 | Top-quark mass | 24 |
| 6.2 | Weak mixing angle | 24 |
| 6.3 | W-boson mass | 24 |
| 7 | The SM is complete | 26 |
| 8 | The LHC Run-2 | 29 |
| 8.1 | Standard Model and top-quark physics | 29 |
| 8.1.1 | Inelastic proton–proton cross section | 30 |
| 8.1.2 | Jet production | 31 |
| 8.1.3 | Weak boson production | 31 |
| 8.1.4 | Diboson production | 33 |
| 8.1.5 | Top production | 34 |
| 8.2 | Reobservation of the Higgs boson at 13 TeV | 36 |
| 8.3 | Searches — a fresh start | 39 |
| 8.3.1 | Additional Higgs bosons | 39 |
| 8.3.2 | New physics searches in events with jets | 40 |
| 8.3.3 | Searches in leptonic final states | 41 |
| 8.3.4 | Searches for diboson resonances (VV , Vh , hh) | 43 |
| 8.3.5 | Supersymmetry | 44 |
| 8.3.6 | Search for massive long-lived massive particles | 47 |
| 8.3.7 | Searches for dark matter production | 48 |
| 9 | The road to the future | 50 |
| 10 | Conclusions | 54 |

References

- [1] F. Englert and R. Brout, Phys. Rev. Lett. 13, 321 (1964); P.W. Higgs, Phys. Lett. 12, 132 (1964); P. W. Higgs, Phys. Rev. Lett. 13, 508 (1964); G.S. Guralnik, C.R. Hagen, and T.W.B. Kibble, Phys. Rev. Lett. 13, 585 (1964); P.W. Higgs, Phys. Rev. 145, 1156 (1966); T.W.B. Kibble, Phys. Rev. 155, 1554 (1967).
- [2] W. Bernreuther, Lect. Notes Phys. 591, 237 (2002) [[hep-ph/0205279](#)].
- [3] H1 and ZEUS Collaborations Eur. Phys. J. C 75, 580 (2015) [[1506.06042](#)].
- [4] ALEPH, DELPHI, L3, OPAL, SLD Collaborations, LEP Electroweak Working Group, SLD Electroweak and Heavy Flavour Groups, Phys. Rept. 427, 257 (2006) [[hep-ex/0509008](#)]; ALEPH, DELPHI, L3, OPAL Collaborations, LEP Electroweak Working Group, Phys. Rept. 532, 119 (2013) [[1302.3415](#)].
- [5] L. Evans and P. Bryant, JINST 3 (2008) S08001, ed. by L. Evans.
- [6] LHC luminosity calibration tool: <https://lpc.web.cern.ch/lumi2.html>.
- [7] ATLAS Collaboration, [1608.03953](#) (2016).
- [8] CMS Collaboration, CMS-PAS-LUM-13-001 (2013), CMS-PAS-LUM-15-001 (2016).
- [9] LHCb Collaboration, JINST 9 no. 12, 12005 (2014) [[1410.0149](#)].
- [10] S. van der Meer, [CERN-ISR-PO-68-31](#), [ISR-PO-68-31](#) (1968).
- [11] J. Stirling, [Parton luminosity plots](#).
- [12] J. Collins, *Foundations of Perturbative QCD*, Cambridge Monographs on Particle Physics, Nuclear Physics and Cosmology, 2011.
- [13] V.N. Gribov and L.N. Lipatov. Sov. J. Nucl. Phys. 15, 438 (1972); Y.L. Dokshitzer. Sov. Phys. JETP 46, 641 (1977); G. Altarelli and G. Parisi. Nucl. Phys. B 126, 298 (1977).
- [14] S. Agostinelli et al., Nucl. Instrum. Meth. A 506, 250 (2003), <http://cern.ch/geant4>.
- [15] G. Salam, [Talk at LHCP 2016](#), Lund, Sweden, June 2016.
- [16] ATLAS Collaboration, [ATL-PHYS-PUB-2015-013](#) (2015).
- [17] M. Cacciari, G.P. Salam, G. Soyez, JHEP 0804, 063 (2008) [[0802.1189](#)].
- [18] ATLAS Collaboration, JHEP 1309, 076 (2013) [[1306.4945](#)].
- [19] CMS Collaboration, JHEP 12, 017 (2014) [[1410.4227](#)].
- [20] CMS Collaboration, [1609.05331](#) (2016).
- [21] ATLAS Collaboration, Phys. Rev. Lett. 113, 141803 (2014) [[1405.6241](#)]; [1611.02428](#) (2016);
- [22] CMS Collaboration, Phys. Rev. Lett. 114, 051801 (2015) [[1410.6315](#)].
- [23] ATLAS Collaboration, JHEP 11, 172 (2015) [[1509.05276](#)].
- [24] CMS Collaboration, JHEP 01, 096 (2016) [[1510.01131](#)].
- [25] ATLAS Collaboration, Phys. Rev. D. 90, 112006 (2014) [[1406.7844](#)]; ATLAS-CONF-2014-007 (2014).
- [26] CMS Collaboration, JHEP 06, 090 (2014) [[1403.7366](#)].
- [27] ATLAS Collaboration, JHEP 1601, 064 (2016) [[1510.03752](#)].
- [28] CMS Collaboration, Phys. Rev. Lett. 112, 231802 (2014) [[1401.2942](#)].
- [29] ATLAS Collaboration, Phys. Lett. B 756, 228 (2016) [[1511.05980](#)].
- [30] CDF and D0 Collaborations, Phys. Rev. Lett. 112, 231803 (2014) [[1402.5126](#)].
- [31] ATLAS Collaboration, Phys. Lett. B 716, 1 (2012) [[1207.7214](#)].
- [32] CMS Collaboration, Phys. Lett. B 716, 30 (2012) [[1207.7235](#)].
- [33] The ALEPH, DELPHI, L3 and OPAL Collaborations, and LEP Working Group for Higgs Boson Searches, Phys. Lett. B 565, 61 (2003) [[hep-ex/0306033](#)].

- [34] CDF and D0 Collaborations, Phys. Rev. D 88, 052014 (2013) [[1303.6346](#)].
- [35] ALEPH, CDF, D0, DELPHI, L3, OPAL and SLD Collaborations, LEP Electroweak Working Group, Tevatron Electroweak Working Group, SLD Electroweak and Heavy Flavour Groups [1012.2367](#); J. Erler and P. Langacker (in: Review for Particle Data Group), Phys. Rev. D 86, 010001 (2012); M. Baak et al., Eur. Phys. J. C 72, 2003 (2012) [[1107.0975](#)].
- [36] LHC Higgs Cross Section Working Group, [1610.07922](#) (2016).
- [37] M. Carena, C. Grojean, and M. Kado, Review in PDG, Chin. Phys. C38, 090001 (2014).
- [38] ATLAS Collaboration, Phys. Rev. D 90, 112015 (2014) [[1408.7084](#)].
- [39] ATLAS Collaboration, Phys. Rev. D 91, 012006 (2015) [[1408.5191](#)].
- [40] ATLAS Collaboration, Phys. Rev. D 92, 012006 (2015) [[1412.2641](#)]; JHEP 08, 137 (2015) [[1506.06641](#)].
- [41] CMS Collaboration, Eur. Phys. J. C 74, 3076 (2014) [[1407.0558](#)].
- [42] CMS Collaboration, Phys. Rev. D 89, 092007 (2014) [[1312.5353](#)].
- [43] CMS Collaboration, JHEP 01, 096 (2014) [[1312.1129](#)].
- [44] ATLAS and CMS Collaborations, Phys. Rev. Lett. 114, 191803 (2015) [[1503.07589](#)].
- [45] ATLAS and CMS Collaborations, JHEP 1608, 045 (2016) [[1606.02266](#)].
- [46] S. Heinemeyer et al., [1307.1347](#) (2013).
- [47] ATLAS Collaboration, JHEP 04, 117 (2015) [[1501.04943](#)].
- [48] CMS Collaboration, JHEP 05, 104 (2014) [[1401.5041](#)].
- [49] ATLAS Collaboration, Phys. Lett. B 740, 222 (2015) [[1409.3122](#)]; Eur. Phys. J. C 75, 349 (2015) [[1503.05066](#)]; Phys. Lett. B 749, 519 (2015) [[1506.05988](#)].
- [50] CMS Collaboration, JHEP 05, 145 (2013) [[1303.0763](#)]; JHEP 09, 087 (2014) [[1408.1682](#)].
- [51] ATLAS Collaboration, JHEP 1601, 172 (2016) [[1508.07869](#)].
- [52] CMS Collaboration, Eur. Phys. J. C 74, 2980 (2014) [[1404.1344](#)]; [1610.09218](#) (2016).
- [53] ATLAS Collaboration, JHEP 1511, 206 (2015) [[1509.00672](#)].
- [54] CMS and LHCb Collaborations, Nature 522, 68 (2015) [[1411.4413](#)].
- [55] C. Bobeth et al., Phys. Rev. Lett. 112, 101801 (2014) [[1311.0903](#)].
- [56] ATLAS Collaboration, Eur. Phys. J. C 76, 513 (2016) [[1604.04263](#)].
- [57] ATLAS Collaboration, JHEP 08, 147 (2016) [[1601.03297](#)].
- [58] CMS Collaboration, Phys. Lett. B 757, 97 (2016) [[1507.07527](#)].
- [59] LHCb Collaboration, Phys. Rev. Lett. 114, 041801 (2015) [[1411.3104](#)].
- [60] LHCb Collaboration, LHCb-CONF-2016-001 (2016).
- [61] CKMfitter Group, updates at <http://ckmfitter.in2p3.fr> (2015).
- [62] LHCb Collaboration, Nature Physics 10, 1038 (2015) [[1504.01568](#)].
- [63] LHCb Collaboration, Eur.Phys.J. C 76, 412 (2016) [[1604.03475](#)].
- [64] LHCb Collaboration, Phys. Rev. Lett. 115, 031601 (2015) [[1503.07089](#)].
- [65] UA1 Collaboration, Europhys. Lett. 1, 327 (1986).
- [66] UA2 Collaboration, Phys. Lett. B 276, 354 (1992).
- [67] LHCb Collaboration, Phys.Rev.Lett. 116, 241601 (2016) [[1603.04804](#)].
- [68] R.N. Cahn, Rev. Mod. Phys. 68, 951 (1996).
- [69] BABAR Collaboration, Phys. Rev. Lett. 109, 101802 (2012) [[1205.5442](#)].
- [70] Belle Collaboration, Phys. Rev. D 92, 072014 (2015) [[1507.03233](#)].
- [71] LHCb Collaboration, Phys. Rev. Lett. 115, 111803 (2015) [[1506.08614](#)].
- [72] Belle Collaboration, [1603.06711](#) (2016).

- [73] Heavy Flavour Averaging Group, [R_{D\(*\)} combination \(2016\)](#).
- [74] S. Fajfer, J.F. Kamenik, and I. Nisandzic, Phys. Rev. D85, 094025 (2012) [[1203.2654](#)].
- [75] LHCb Collaboration, Phys. Rev. Lett. 113, 151601 (2014) [[1406.6482](#)].
- [76] LHCb Collaboration, Phys. Rev. Lett. 115, 072001 (2015) [[1507.03414](#)].
- [77] M.E. Peskin and T. Takeuchi, Phys. Rev. D 46, 381 (1992).
- [78] J.R. Ellis, G.L. Fogli and E. Lisi, Phys. Lett. B 343, 282 (1995).
- [79] M. Baak et al., Eur. Phys. J. C 72, 2003 (2012) [[1107.0975](#)].
- [80] M. Baak *et al.*, Eur. Phys. J. C 74, 3046 (2014) [[1407.3792](#)].
- [81] CDF and D0 Collaborations, Phys. Rev. D 88, 052018 (2013) [[1307.7627](#)].
- [82] CMS Collaboration, Phys. Rev. D 93, 072004 (2016) [[1509.04044](#)].
- [83] ATLAS Collaboration, Phys. Lett. B 761, 350 (2016) [[1606.02179](#)].
- [84] CDF and D0 Collaborations, [1407.2682](#) (2014).
- [85] CMS Collaboration, Eur. Phys. J. C 73, 2494 (2013) [[1304.5783](#)].
- [86] CMS Collaboration, CMS-PAS-TOP-15-014 (2015).
- [87] CMS Collaboration, [1603.02303](#) (2016).
- [88] ATLAS Collaboration, JHEP 09, 049 (2015) [[1503.03709](#)].
- [89] CMS Collaboration, Phys. Rev. D 84, 112002 (2011) [[1110.2682](#)].
- [90] LHCb Collaboration, JHEP 1511, 190 (2015) [[1509.07645](#)].
- [91] A. Bodek, Eur. Phys. J. C, 76, 1 (2016) [[1512.08256](#)].
- [92] CMS Collaboration, CMS-PAS-SMP-14-007 (2016).
- [93] ATLAS Collaboration, Eur. Phys. J. C 76, 1 (2016) [[1512.02192](#)].
- [94] C. Balazs, J.W. Qiu and C. Yuan, Phys. Lett. B 355, 548 (1995) [[hep-ph/9505203](#)].
- [95] S. Catani et al., Phys. Rev. Lett. 103, 082001 (2009) [[0903.2120](#)].
- [96] Gfitter Group (M. Baak et al.), Eur. Phys. J. C 72, 2205 (2012) [[1209.2716](#)].
- [97] J. Ellis et al., Phys.Lett. B 679, 369 (2009) [[0906.0954](#)].
- [98] B. Bertotti, L. Iess, P. Tortora, Nature 425, 374 (2003).
- [99] M. Mangano, [Talk at SEARCH 2016](#), Oxford, UK, August 2016.
- [100] ATLAS Collaboration, Phys. Lett. B, 158 (2016) [[1607.06605](#)].
- [101] TOTEM Collaboration, Phys. Rev. Lett. 111, 012001 (2013).
- [102] ATLAS Collaboration, [1606.02625](#) (2016).
- [103] CMS Collaboration, Eur. Phys. J. C 76, 451 (2016) [[1605.04436](#)].
- [104] ATLAS Collaboration, Eur. Phys. J. C 72, 1909 (2012) [[1110.3174](#)].
- [105] ATLAS Collaboration, Phys.Lett. B 759, 601 (2016) [[1603.09222](#)].
- [106] CMS Collaboration, CMS-PAS-SMP-15-004 (2015).
- [107] LHCb Collaboration, LHCb-CONF-2016-002 (2016).
- [108] ATLAS Collaboration, Phys. Rev. Lett. 109, 012001 (2012) [[1203.4051](#)].
- [109] ATLAS Collaboration, Phys. Rev. Lett. 116, (2016) [[1512.05314](#)].
- [110] CMS Collaboration, CMS-PAS-SMP-16-006 (2016).
- [111] ATLAS Collaboration, Phys. Lett. B 762, 1 (2016) [[1606.04017](#)].
- [112] ALEPH, DELPHI, L3 and OPAL Collaborations, LEP Electroweak Working Group, Phys.Rept. 532, 119 (2013) [[1302.3415](#)].
- [113] D.R. Green, P. Meade, M.-A. Pleier, [1610.07572](#) (2016).
- [114] ATLAS Collaboration, Eur. Phys. J. C 74, 3109 (2014) [[1406.5375](#)].
- [115] ATLAS Collaboration, Phys. Lett. B 761, 136 (2016) [[1606.02699](#)].

- [116] J. Wenninger, [CERN-ATS-2013-040](#) (2013).
- [117] ATLAS Collaboration, [1609.03920](#) (2016).
- [118] CMS Collaboration, [1610.00678](#) (2016).
- [119] ATLAS Collaboration, ATLAS-CONF-2016-065 (2015).
- [120] ATLAS Collaboration, [1609.01599](#) (2016).
- [121] CMS Collaboration, CMS-PAS-TOP-16-017 (2016).
- [122] ATLAS Collaboration, ATLAS-CONF-2016-079 (2016).
- [123] CMS Collaboration, CMS-PAS-HIG-16-033 (2016).
- [124] ATLAS Collaboration, ATLAS-CONF-2016-067 (2016).
- [125] CMS Collaboration, CMS-PAS-HIG-16-020 (2016).
- [126] ATLAS Collaboration, ATLAS-CONF-2016-081 (2016).
- [127] ATLAS Collaboration, ATLAS-CONF-2016-091 (2016).
- [128] ATLAS Collaboration, JHEP 01, 069 (2015) [[1409.6212](#)].
- [129] CMS Collaboration, Phys. Rev. D 89, 012003 (2014) [[1310.3687](#)].
- [130] ATLAS Collaboration, ATLAS-CONF-2016-041 (2016).
- [131] CMS Collaboration, CMS-PAS-HIG-16-022 (2016).
- [132] CMS Collaboration, CMS-PAS HIG-15-005 (2016).
- [133] CMS Collaboration, CMS-PAS HIG-16-004 (2016).
- [134] ATLAS Collaboration, ATLAS-CONF-2016-058 (2016); ATLAS-CONF-2016-067 (2016); ATLAS-CONF-2016-080 (2016).
- [135] ATLAS Collaboration, ATLAS-CONF-2016-06 (2016).
- [136] ATLAS Collaboration, ATLAS-CONF-2016-088 (2016).
- [137] CMS Collaboration, CMS-PAS-HIG-16-031 (2016).
- [138] ATLAS Collaboration, ATLAS-CONF-2016-085 (2016).
- [139] CMS Collaboration,
- [140] ATLAS Collaboration, ATLAS-CONF-2016-015 (2016).
- [141] ATLAS Collaboration, Phys. Rev. Lett. 114, 081802 (2015) [[1406.5053](#)].
- [142] ATLAS Collaboration, ATLAS-CONF-2016-004 (2016).
- [143] CMS Collaboration, CMS-PAS-HIG-16-032 (2016).
- [144] CMS Collaboration, CMS-PAS-HIG-16-029 (2016).
- [145] CMS Collaboration, CMS-PAS-HIG-16-024 (2016).
- [146] ATLAS Collaboration, Phys. Rev. D 94, 052002 (2016) [[1606.04782](#)].
- [147] CMS Collaboration, CMS-PAS-HIG-16-026 (2016).
- [148] CMS Collaboration, Phys. Lett. B 749, 337 (2015) [[1502.07400](#)].
- [149] ATLAS Collaboration, [1604.07730](#) (2016).
- [150] CMS Collaboration, CMS-PAS-HIG-16-005 (2016).
- [151] ATLAS Collaboration, ATLAS-CONF-2016-069 (2016).
- [152] ATLAS Collaboration, ATLAS-CONF-2016-070 (2016).
- [153] CMS Collaboration, [1611.03568](#) (2016).
- [154] ATLAS Collaboration, ATLAS-CONF-2016-030 (2016).
- [155] CMS Collaboration, Phys. Rev. Lett. 117, 031802 (2016) [[1604.08907](#)].
- [156] ATLAS Collaboration, [1603.08791](#) (2016); ATLAS-CONF-2016-014 (2016); ATLAS-CONF-2016-060 (2016).
- [157] CMS Collaboration, CMS-PAS-B2G-15-002 (2016).

- [158] ATLAS Collaboration, ATLAS-CONF-2016-045 (2016).
- [159] CMS Collaboration, CMS-PAS-EXO-16-031 (2016).
- [160] ATLAS Collaboration, ATLAS-CONF-2016-061 (2016).
- [161] CMS Collaboration, CMS-PAS-EXO-15-006 (2016).
- [162] ATLAS Collaboration, ATL-PHYS-PUB-2013-003 (2013); ATL-PHYS-PUB-2015-004 (2015)
- [163] H. Bachacou, Table shown at SEARCH2016 workshop, Oxford, UK (Sep 2016).
- [164] ATLAS Collaboration, JHEP 12, 55 (2015) [[1506.00962](#)].
- [165] CMS Collaboration, JHEP 08, 173 (2014) [[1405.1994](#)].
- [166] ATLAS Collaboration, ATLAS-CONF-2016-05 (2016).
- [167] CMS Collaboration, CMS-PAS-B2G-16-020 (2016); CMS-PAS-B2G-16-007 (2016).
- [168] ATLAS Collaboration, Phys. Rev. D 92, 032004 (2015) [[1504.05511](#)].
- [169] ATLAS Collaboration, Phys. Rev. Lett. 113, 171801 (2014) [[1407.6583](#)].
- [170] CMS Collaboration, Phys. Lett. B 750, 494 (2015) [[1506.02301](#)].
- [171] ATLAS Collaboration, Eur. Phys. J. C 76, 1 (2016) [[1509.05051](#)].
- [172] ATLAS Collaboration, [1606.03833](#) (2016).
- [173] CMS Collaboration, [1606.04093](#) (2016).
- [174] ATLAS Collaboration, ATLAS-CONF-2016-059 (2016).
- [175] CMS Collaboration, [1609.02507](#) (2016).
- [176] ATLAS Collaboration, JHEP 10, 134 (2015) [[1508.06608](#)].
- [177] CMS Collaboration, JHEP 10, 129 (2016) [[1606.03577](#)].
- [178] CMS Collaboration, CMS-PAS-SUS-16-014 (2016).
- [179] CMS Collaboration, CMS-PAS-SUS-16-015 (2016).
- [180] ATLAS Collaboration, ATLAS-CONF-2016-052 (2016).
- [181] J. Barnard, P. Cox, T. Gherghetta, A. Spray, JHEP 1603, 003 (2016) [[1510.06405](#)].
- [182] ATLAS Collaboration, Phys. Rev. D 88, 112006 (2013) [[1310.3675](#)].
- [183] ATLAS Collaboration, Phys. Rev. D 88, 112003 (2013) [[1310.6584](#)].
- [184] CMS Collaboration, Eur. Phys. J. C 75, 151 (2015) [[1501.05603](#)].
- [185] LHC Dark Matter Forum, [1507.00966](#) (2015).
- [186] ATLAS Collaboration, Phys. Rev. D 94, 032005 (2016) [[1604.07773](#)].
- [187] CMS Collaboration, CMS-PAS-EXO-16-037 (2016).
- [188] ATLAS Collaboration, JHEP 06, 059 (2016) [[1604.01306](#)].
- [189] CMS Collaboration, CMS-PAS-EXO-16-039 (2016).
- [190] ATLAS Collaboration, Phys. Lett. B 763, 251 (2016) [[1608.02372](#)].
- [191] CMS Collaboration, CMS-PAS-EXO-16-038 (2016); CMS-PAS-EXO-16-037 (2016); CMS-PAS-EXO-16-010 (2016).
- [192] ATLAS Collaboration, ATLAS-CONF-2016-086 (2016).
- [193] CMS Collaboration, CMS-PAS-B2G-15-007 (2016).
- [194] CMS Collaboration, CMS-PAS-EXO-16-028 (2016); CMS-PAS-EXO-16-005 (2016).
- [195] LUX Collaboration, Phys. Rev. Lett. 116, 161302 (2016) [[1602.03489](#)].
- [196] ATLAS Collaboration, [Dark Matter searches summary plot](#).
- [197] The HI-LHC project: <http://hilumilhc.web.cern.ch>.
- [198] ATLAS Collaboration, [CERN-LHCC-2015-020](#) (2015).
- [199] CMS Collaboration, [CERN-LHCC-2015-019](#) (2015).
- [200] P. Ferreira da Silva at Moriond EW, 2016.

- [201] ATLAS Collaboration, ATL-PHYS-PUB-2014-016 (2014).
- [202] ATLAS Collaboration, Eur. Phys. J. C 75, 335 (2015) [[1503.01060](#)].
- [203] CMS Collaboration, JHEP 09, 051 (2016) [[1605.02329](#)].
- [204] LHC Higgs Cross Section Working Group, CERN-2013-004, [1307.1347](#) (2013).
- [205] ATLAS Collaboration, ATL-PHYS-PUB-2015-024 (2015).
- [206] CMS Collaboration, CMS-PAS-FTR-13-022 (2013).